ABSTRACT

Title of dissertation: SUPERCONDUCTIVITY IN TRANSITION-METAL SUBSTITUTED IRON-BASED SUPERCONDUCTORS:

Kevin Kirshenbaum, Doctor of Philosophy, 2013

Dissertation directed by: Professor Johnpierre Paglione
Department of Physics

I report on superconductivity in undoped $SrFe_2As_2$ and find that it is caused by lattice strain in the as-grown crystals that can be removed or returned with annealing or pressure, respectively. To study the magnetic/structural transition I measure the evolution of these transitions in solid solutions of the [Ca, Sr, Ba]Fe_2As_2 series and determine that the Neél temperature is independent of the size of the antiferromagnetically ordered moment. I present the first reported phase diagrams for Ni- and Pt-substitution in $SrFe_2As_2$, showing that the simple charge-counting picture of chemical substitution cannot completely describe the onset and offset of the superconducting phase. Finally, I use the transport scattering rate to explain the variation in T_c seen in transition metal substituted 122s. I will show that pair breaking can explain the variation in the optimum transition temperature, and that the rate of suppression of T_c with scattering will show that the pairing symmetry of the iron-based superconductors is a sign-changing, multiband s-wave order parameter that must include both inter- and intraband scattering.

SUPERCONDUCTIVITY IN TRANSITION METAL SUBSITUTED IRON-BASED SUPERCONDUCTORS

by

Kevin Kirshenbaum

Dissertation submitted to the Faculty of the Graduate School of the
University of Maryland, College Park in partial fulfillment
of the requirements for the degree of
Doctor of Philosophy
2013

Advisory Committee:
Professor Johnpierre Paglione
Professor Richard Greene
Professor Ichiro Takeuchi
Professor Steven Anlage
Professor Frederick Wellstood

© Copyright by
Kevin Kirshenbaum
2013

Dedication

To JP for his guidance, my parents for their encouragement, and to Amy for her unwavering support.

Acknowledgments

Low temperature condensed matter experiments have always required the efforts of many working together. The work in this thesis was performed over five years and required the help of dozens of people. I would like to take this opportunity to acknowledge those without whom I could not have completed this work:

First I would like to thank my advisor, Johnpierre Paglione, for providing me with guidance these past few years. I will always appreciate the opportunity that he gave me to join his group in its early stages, giving me the chance to see how a lab is built. The experience of setting up a lab space is something that I will always remain grateful for.

Next I would like to acknowledge the former post docs in our group, Shanta Saha and Nicholas Butch, who assisted with most of the studies in this thesis and taught me so much the first few years. I would also like to acknowledge our collaborators for their work on several of the studies cited in this thesis: Peter Zavaij in the Chemistry department, Jeffrey Lynn at NIST, and Jason Jeffries at LLNL.

I would like to thank Richard Greene and Ichiro Takeuchi and the post docs who worked alongside them, Kui Jin and Xiaohang Zhang, for providing their expertise in unconventional superconductors as well as their technical assistance keeping the PPMS running.

I have been fortunate enough to work alongside several other highly successful graduate students: Tyler Drye, Paul Syers, Steven Ziemak, and Richard Suchoski have been extremely supportive during my graduate career. We have also been for-

tunate to have several undergradute students working with us over summer sessions: Gabriel Droulers, Jeffrey Magill, Andrew Hope, and Alex Hughes are all deserving of my thanks and appreciation for their long hours keeping the dilution refrigerator cold.

It is with immense gratitude that I acknowledge the support and help of the CNAM technical staff, Doug Benson and Brian Straughn, who have personally helped me take apart and put back together almost everything in the lab with very few parts left over. It was Doug's words of wisdom that gave me the courage to take apart broken (and expensive) equipment before trying to contact the manufacturer. I say this to thank him and so that anyone reading this knows who to blame when the equipment falls apart.

Last and most, I would like to thank my parents who have helped to lift me through my education and show me what is most important in life. They, more than any other factor, are why I am writing this today. I would like to thank my twin brother, Kyle, for speeding up my education; gloating over receiving his Master's before me was reason enough to graduate as quickly as possible. Finally, I am grateful for my fiancée Amy who has listened to me patiently as I finish my degree. Her support during this time has been unbelievable, and I am forever grateful to her.

Foreword

Much of the work presented in this thesis has been published, and thus portions of this thesis have been summarized or paraphrased from the following published works:

S.R. Saha, N.P. Butch, K. Kirshenbaum, Johnpierre Paglione, **Superconducting and ferromagnetic phases induced by lattice distortions in $SrFe_2As_2$.** Physical Review Letters **103**, 037005 (2009) (Ref. [1]).

K. C. Kirshenbaum, S. R. Saha, N. P. Butch, J. D. Magill, J. Paglione, **Superconductivity in the Iron-Pnictide Parent Compound $SrFe_2As_2$.** Science and Technology for Humanity (TIC-STH), 2009 IEEE Toronto International Conference. p.861 (2009) (Ref. [2]).

K. Kirshenbaum, N. P. Butch, S. R. Saha, P. Y. Zavalij, B. G. Ueland, J. W. Lynn, J. Paglione, **Tuning magnetism in FeAs-based materials via tetrahedral structure.** Physical Review B **86**, 060504(R) (2012) (Ref. [3]).

Shanta R. Saha, Kevin Kirshenbaum, Nicholas P. Butch, Peter Y. Zavalij, Johnpierre Paglione, **Uniform chemical pressure effect in solid solutions $Ba_{1-x}Sr_xFe_2As_2$ and $Sr_{1-x}Ca_xFe_2As_2$.** Journal of Physics: Conference Series **273**, 012104 (2011) (Ref. [4]).

S.R. Saha, N.P. Butch, K. Kirshenbaum, Johnpierre Paglione, **Evolution of bulk superconductivity in $SrFe_2As_2$ with Ni substitution.** Physical Review

B **79**, 224519 (2009) (Ref. [5]).

Shanta R. Saha, Nicholas P. Butch, Kevin Kirshenbaum, Johnpierre Paglione, **Annealing effects on superconductivity in $SrFe_{2-x}Ni_xAs_2$.** Physica C **470**, S379 (2009) (Ref. [6]).

N. P. Butch, S. R. Saha, X. H. Zhang, K. Kirshenbaum, R. L. Greene, J. Paglione, **Effective carrier type and field-dependence of the reduced-T_c superconducting state in $SrFe_{2-x}Ni_xAs_2$.** Physical Review B **81**, 024518 (2010) (Ref. [7]).

Kevin Kirshenbaum, Shanta R. Saha, Tyler Drye, Johnpierre Paglione, **Superconductivity and magnetism in platinum-substituted $SrFe_2As_2$ single crystals.** Physical Review B **82**, 144518 (2010) (Ref. [8]).

Kevin Kirshenbaum, Shanta R. Saha, Steven Ziemak, Tyler Drye, and Johnpierre Paglione, **Universal pair-breaking in transition metal-substituted iron-pnictide superconductors.** Physical Review B **86**, 140505 (2012) (Ref. [9]).

Table of Contents

List of Figures ix

List of Abbreviations xii

1 Iron-Based Superconductors 1
1.1 122 Iron-Based Superconductors . . . 5
1.2 Pairing Symmetry . . . 8
1.3 Open Questions . . . 16

2 Experimental Details 18
2.1 Sample Preparation . . . 18
2.1.1 Single Crystal Growth . . . 19
2.1.2 Preparing Samples for Measurement . . . 25
2.1.3 2, 4, and 6 Probe Techniques . . . 29
2.2 Characterization . . . 32
2.2.1 X-ray Diffractometry . . . 35
2.2.2 Energy- and Wavelength Dispersive X-Ray Spectroscopy . . . 36
2.3 Temperature and Magnetic Field Control . . . 37
2.3.1 Physical Properties Measurement System . . . 38
2.3.2 Magnetic Properties Meaasurement System . . . 39
2.3.3 Dipper Probe . . . 39
2.3.4 15/17 T Superconducting Magnet . . . 40
2.4 Electronic Transport . . . 41
2.4.1 AC Resistance Bridges . . . 46
2.4.2 Longitudinal Resistivity . . . 48
2.4.3 Transverse Resistivity in Magnetic Fields . . . 50
2.4.4 Scattering Rate . . . 54
2.5 Magnetic Susceptibility . . . 55
2.6 Pairing Symmetry and Scattering Rate . . . 58

3 Superconductivity in the Undoped Parent Compound $SrFe_2As_2$ 63
3.1 Experimental Details . . . 65
3.2 Observation of Superconductivity . . . 66
3.3 Annealing and Cold-Working Studies . . . 69
3.4 Lattice Distortion . . . 76
3.5 Enhanced Magnetic Susceptibility . . . 80
3.6 Conclusions . . . 84

4 Isovalent Elemental Substitution in the [Ca,Sr,Ba]Fe_2As_2 Series 86
4.1 Experimental Details . . . 88
4.2 Characterization of Transition Temperatures . . . 89
4.3 Magnetic Order Parameter . . . 95

4.4 Evolution of Structural and Magnetic Properties with Alkaline Earth Substitution . . . 97
4.5 Conclusions . . . 101

5 Comparison of Ni- and Pt- substitution in $SrFe_2As_2$ 103
5.1 $SrFe_{2-x}Ni_xAs_2$ . . . 105
5.1.1 Growth and Characterization . . . 106
5.1.2 Effect of Annealing . . . 107
5.1.3 Resistivity and Magnetization Measurements . . . 111
5.1.4 Upper Crifical Field . . . 121
5.1.5 Hall Effect and Carrier Concentration . . . 128
5.2 $SrFe_{2-x}Pt_xAs2$ and Comparison to $SrFe_{2-x}Ni_xAs2$ . . . 129
5.2.1 Resistivity and Magnetic Susceptibility . . . 133
5.2.2 Upper Critical Field . . . 139
5.3 Comparison and Conclusions . . . 142

6 Pair Breaking in Transition Metal Substituted 122s 145
6.1 Experimental Details . . . 151
6.2 Results and Discussion . . . 154
6.3 Conclusions . . . 162

7 Conclusions 164

A Lattice Constants for Select Concentrations in the [Ca, Sr, Ba]Fe_2As_2 Series 168

B Additional Figures for Pair Breaking Chapter 172

Bibliography 176

List of Figures

1.1 Different families of iron-based superconductors. 3
1.2 Single crystal of Ni-substituted $SrFe_2As_2$ grown using the self flux technique. 5
1.3 Phase diagram for $Ba(Fe_{1-x}Co_x)_2As_2$. 7
1.4 Fermi surface of $Ba_{1-x}K_xFe_2As_2$ determined by ARPES. 12
1.5 Fermi surface of $BaFe_{2-x}Co_xAs_2$ determined by ARPES. 13
1.6 Possible pairing symmetries for multiband superconductors. 15

2.1 Binary phase diagram for Fe-As. 21
2.2 Typical growth schedule for 122 single crystals. 23
2.3 Single crystal growth tube before placing into furnace. 24
2.4 Photograph of a typical as-grown single crystal of $SrFe_{2x}Ni_xAs_2$ harvested from flux growth. 26
2.5 Configurations for electrical transport measurements 33
2.6 Picture of sample $SrFe_{1.80}Pd_{0.20}As_2$ B33 6W1 showing 6-wire lead configuration. 34
2.7 Schematic drawing of dipper tail. 42
2.8 Schematic drawing of dipper tail; close-up on head. 43
2.9 Schematic drawing of dipper tail; close-up on bottom. 44
2.10 Schematic drawing of dipper tail; side view. 45
2.11 Field cooled and zero-field cooled magnetic susceptibility curves for $BeFe_{1.85}Pt_{0.15}As_2$. 57
2.12 Rate of suppression of superconducting transition temperature, T_c for different order parameters and types of scattering. 59
2.13 Plot of pairbreaking prediction by Abrokosov and Gor'kov 61

3.1 Comparison of resistivity of several as-grown specimens of $SrFe_2As_2$ normalized to 300 K 67
3.2 Resistivity vs. temperature for $SrFe_2As_2$ at fields from 0 to 14 T . . . 68
3.3 Diamagnetic screening in four $SrFe_2As_2$ single crystals as measured by magnetic susceptibility 70
3.4 Effect of annealing on resistivity of a single-crystal sample of $SrFe_2As_2$ 72
3.5 Heat treatment and applied pressure effects on resistive superconducting transition in one sample of $SrFe_2As_2$ 73
3.6 Electrical resistivity measurements of a single-crystal sample of $SrFe_2As_2$ subject to various treatments 75
3.7 Scanning electron microscopy images of a single-crystal sample of $SrFe_2As_2$ subject to severe deformation 77
3.8 Reciprocal-lattice structure of $SrFe_2As_2$ from single-crystal x-ray diffraction 79
3.9 Magnetic susceptibility of one single crystal specimen of $SrFe_2As_2$ . . 81
3.10 Ferromagnetic moment and superconducting volume fraction at 1.8 K for several samples of $SrFe_2As_2$ exhibiting a proportional relationship 83

4.1 Structural and chemical properties of (Ca,Sr,Ba)Fe_2As_2 91
4.2 Evolution of resistivity and magnetic susceptibility with substitution in the (Ca,Sr,Ba)Fe_2As_2 series. 93
4.3 Characterization of the first-order antiferromagnetic transition observed in electrical resistivity measurements of $Sr_{1-y}Ca_yFe_2As_2$ 94
4.4 Evolution of structure and magnetic order parameter in $Sr_{1-y}Ca_yFe_2As_2$ as measured by neutron diffraction 98
4.5 Evolution of structural and magnetic properties of $Ba_{1-x}Sr_xFe_2As_2$ and $Sr_{1-y}Ca_yFe_2As_2$ as a function of solution concentration 100

5.1 Crystallographic and chemical data for the series $SrFe_{2-x}Ni_xAs_2$ . . . 108
5.2 Effect of high-temperature annealing on an optimally doped x = 0.15 sample of $SrFe_{2-x}Ni_xAs_2$ 110
5.3 Volume magnetic susceptibility of $SrFe_{1.85}Ni_{0.15}As_2$ 112
5.4 Temperature dependence of in-plane electrical resistivity of specimens of $SrFe_{2-x}Ni_xAs_2$ 115
5.5 Ni substitution phase diagram of $SrFe_{2-x}Ni_xAs_2$ 116
5.6 Temperature dependence of magnetic susceptibility χ of $SrFe_{2-x}Ni_xAs_2$ 119
5.7 Evolution of normal and superconducting state parameters in $SrFe_{2-x}Ni_xAs_2$ with Ni concentration x 122
5.8 Electrical resistivity of $SrFe_{2-x}Ni_xAs_2$ vs temperature in magnetic fields 123
5.9 Upper critical field H_{c2} of $SrFe_{2-x}Ni_xAs_2$, for H // c 126
5.10 Upper critical field H_{c2} of $SrFe_{2-x}Ni_xAs_2$ for different field orientations 127
5.11 Hall coefficient of $SrFe_{2-x}Ni_xAs_2$ as a function of temperature. 130
5.12 Variation of the c-axis lattice parameters with Pt concentration in single-crystal samples of $SrFe_{2-x}Pt_xAs_2$ compared with that from powder data of $SrFe_{2-x}Ni_xAs_2$ 132
5.13 Electrical resistivity of single-crystal samples of $SrFe_{2-x}Pt_xAs_2$ 136
5.14 Magnetic susceptibility $SrFe_{2-x}Pt_xAs_2$ 138
5.15 Phase diagrams of the $SrFe_{2-x}Ni_xAs_2$ and $SrFe_{2-x}Pt_xAs_2$ systems. . . 140
5.16 Upper critical field of $SrFe_{1.84}Pt_{0.16}As_2$ 141

6.1 Comparison of the evolution of superconductivity as a function of transition metal substitution in $SrFe_{2-x}TM_xAs_2$ (TM = Co, Ni, Rh, Pd, and Pt) 148
6.2 Comparison of the evolution of superconductivity as a function of transition metal substitution in $Ba(Fe_{1-x}TM_x)_2As_2$ (TM = Co, Rh, Ni, Pd) 149
6.3 Six-wire measurements of resistivity and Hall coefficient of optimally-doped $SrFe_{2-x}Pd_xAs_2$, $SrFe_{2-x}Ni_xAs_2$, $SrFe_{2-x}Co_xAs_2$ and $BaFe_{2-x}Pt_xAs_2$ 155
6.4 Hall coefficient of optimally-doped $SrFe_{2-x}Pd_xAs_2$, $SrFe_{2-x}Ni_xAs_2$, $SrFe_{2-x}Co_xAs_2$ and $BaFe_{2-x}Pt_xAs_2$ 156
6.5 Effect of transition metal substitution on T_c values as a function of the experimental transport scattering rate 158

B.1 Superconducting transition temperature as a function of residual resistivity for several 122 systems 174
B.2 Superconducting transition temperature as a function of transport scattering rate, Γ, for several iron-based superconductors 175

List of Abbreviations

CNAM	Center for Nanophysics and Advanced Materials
FeSC	Iron-based superconductor
TM	Transition metal
T_c	Superconducting transition temperature
T_N	Neél temperature
AFM	Antiferromagnetism
122	Materials with the chemical formula $AEFe_2As_2$ (AE = Ca, Sr, or Ba)
AE	Alkaline earth element
EDS	Energy dispersive x-ray spectroscopy (also called EDX)
WDS	Wavelength dispersive x-ray spectroscopy (also called WDX)

Chapter 1

Iron-Based Superconductors

The history of superconductivity stretches back over 100 years to 1911 when Heike Kamerlingh Onnes at the University of Leiden first liquified helium and observed the disappearance of resistance in mercury below the superconducting transition temperature [29], and it was only two years later that the significance of this research was recognized by the Nobel Prize committee. Following the observation of zero resistance was the discovery of perfect diamagnetism by Meissner and Ochsenfeld [30], a property that sets superconductivity apart from just a perfect conductor. It then took over 40 years to have a theoretical understanding of superconductivity: BCS theory, proposed by Bardeen, Cooper and Schrieffer, finally offered an explanation for superconductivity. According to the theory, electrons are paired and condensed into the superconducting state, with phonons providing the necessary attractive potential [31]. Despite having a microscopic theory of superconductivity, it would be another 30 years until high temperature superconductors were discovered and a major increase in the superconducting transition temperature, T_c, was observed.

The first superconductors discovered were single elements or binary compounds such as Nb_3Sn and NbTi, all with relatively low T_c's (below 25 K), though with high enough upper critical fields to be useful as magnets. The observation of the

isotope effect verified that pairing in these superconductors was phonon mediated. It seemed that superconductivity would be a strictly low-temperature phenomenon until 1986 when the high-T_c cuprates were discovered by Bednorz and Müller [32]. It was soon determined that phonons were not providing the pairing potential in these materials, but rather something more exotic. The exact mechanism is still not agreed upon, although there are several strong candidates proposed (see Refs. [33] and [34] for overviews). Following the discovery of high-T_c superconductors, many other superconducting "families" have been discovered and there is a rich (and growing) pantheon of superconducting materials. Each family of superconductors offers another perspective from which the phonomenon of superconductivity can be studied.

In 2008 a group led by Hideo Hosono discovered a new family of high-temperature superconductors with a layered structure similar to the cuprates [35]. Interestingly, these materials contain iron, an anathema to conventional superconductivity because the magnetic moment would tend to break apart the singlet-paired electrons. Within six months of the discovery of LaFeAsO (related materials are known as "1111" compounds after the chemical formula) transition temperatures up to 55 K were observed. Also in this time, several other classes of iron-based superconductors were discovered. These include the "11" materials (which includes FeSe), "111" materials (such as LiFeAs), and recently several others with larger chemical formulae such as the "32522" materials ($Ca_3Al_2O_{5-y}Fe_2As_2$) and "42622" materials ($Ca_4Al_2O_{6-y}Fe_2As_2$) [36].

What all of these materials have in common is a square lattice of iron atoms

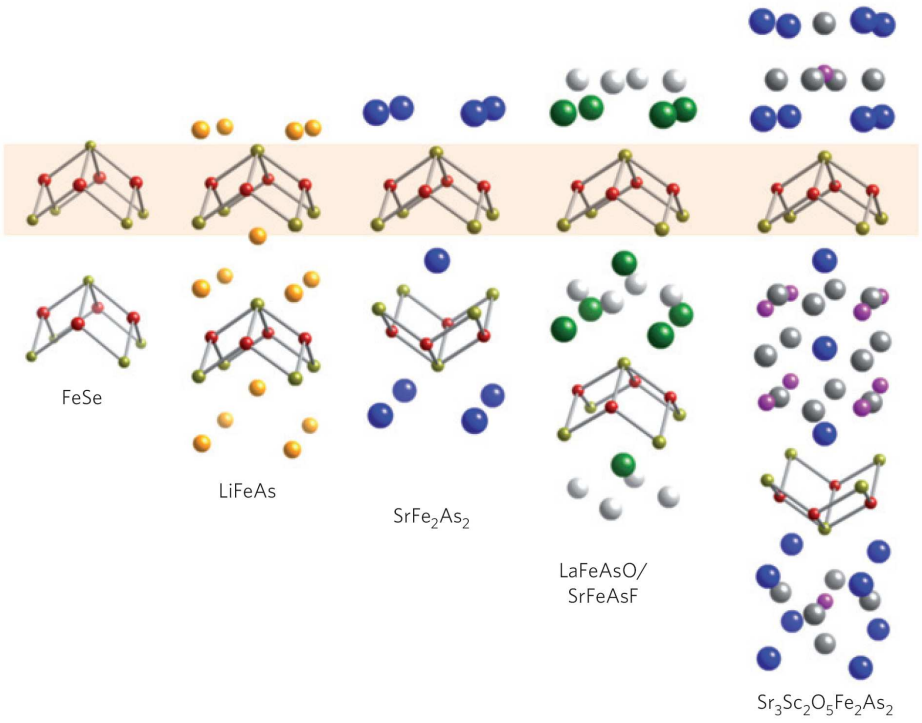

Figure 1.1: Different families of iron-based superconductors. These materials are all related by a square lattice of iron atoms in a layered structure (from Ref. [36]).

in layers with either pnictide or chalcogenide atoms arranged in tetrahedra around the iron (see Fig. 1.1). In fact, this layered structure is similar to that seen in cuprate superconductors where the pairing is expected to take place in the Cu-O layer. In the pnictides, superconductivity is expected to arise in the Fe-As plane. There are a few other notable similarities with cuprate superconductors: similar phase diagrams with antiferromagnetism in the parent compound suppressed with doping or pressure (Fig. 1.3), a tetragonal crystal structure (Fig. 1.1), and strongly correlated electrons. The similarities between these systems provides a stepping off point in the search for new high temperature superconductors.

My work focused on a specific family of iron-based superconductors known as the "122" family which has the chemical formula $AEFe_2As_2$, where AE is an alkali earth element (specifically Ca, Sr, or Ba). While T_c for these materials seems to be slightly lower than the "1111" materials (the highest transition temperatures are $\sim$ 40 K for alkali substitution on the AE site), the 122s have been studied more in-depth owing to the relative ease with which one can grow large, stable single crystals of these materials.

In this chapter I discuss the basic properties of the 122 family of iron-based superconductors that are relevant to this dissertation. For more complete reviews of the many intriguing properties of these materials, there have been several comprehensive review articles published in the last few years. [36, 37, 38, 39].

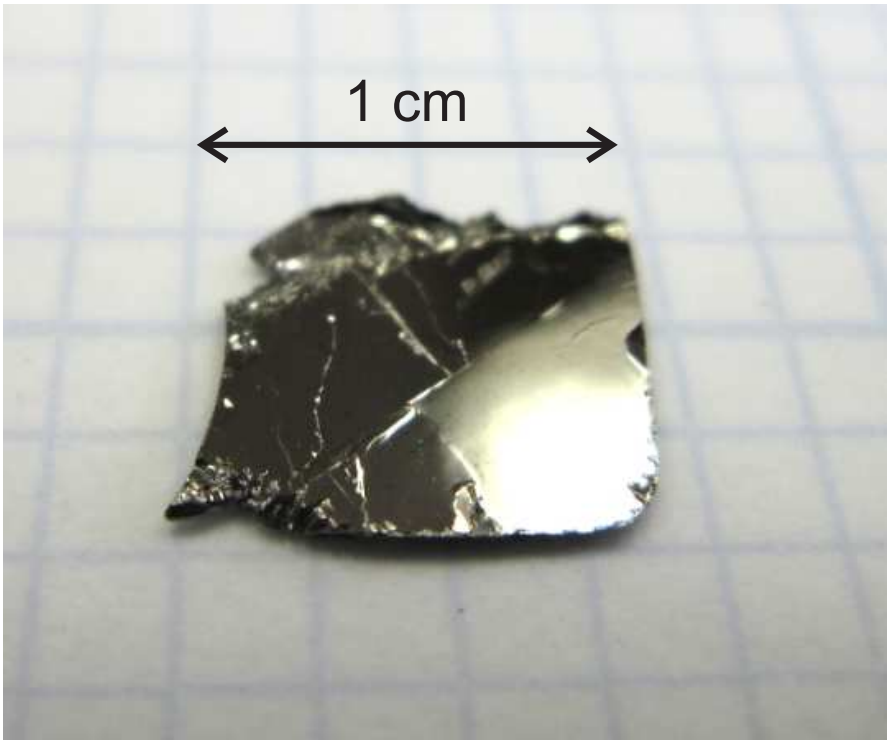

Figure 1.2: Single crystal of Ni-substituted $SrFe_2As_2$ grown using the self flux technique. The crystal size is limited by the size of the crucible (1 cm) (from Ref. [5]).

1.1 122 Iron-Based Superconductors

A majority of single-crystal studies in iron-based superconductors have been on the 122 system, primarily for technical reasons. Although the highest transition temperatures are observed in the 1111 system, it has proven difficult to grow single crystals of these oxypnictides. Instead, the 122 family offers a relatively simple route to grow crucible-limited crystals that can grow to more than 1 cm on a side (see Fig. 1.2).

Iron-based superconductors and cuprates share a common phase diagram [40];

at room temperature these materials are orthorhombic and paramagnetic, however at lower temperatures they transition into a tetragonal antiferromagnetic state at, for example, 165 K for $CaFe_2As_2$ [41], 200 K for $SrFe_2As_2$ [15] and 140 K for $BaFe_2As_2$ [42]. With pressure or chemical subsitution (which is often viewed as either chemical pressure or charge doping depending on the substituent element) the Neél temperature (T_N) decreases and at some point superconductivity begins to emerge at low temperatures. With further substitution or pressure, eventually T_N decreases to 0 K and T_c reaches a maximum; this point is known as "optimal doping". Finally, as doping increases into what is called the "overdoped" region, T_c decreases and the material obeys Fermi liquid theory. Figure 1.3 shows an example of a typical phase diagram for $Ba[Fe_{1-x}Co_x]_2As_2$. Here we see that the structural and magnetic transitions that occur at the same temperature in the parent compound are split at increased doping. Interestingly, although we typically say that these materials require pressure or doping to induce superconductivity, for both cuprates [43] and pnictides (Refs. [1, 2] and discussed at length in Chapter 3), superconductivity has been observed in the parent compound under certain conditions.

The highest transition temperatures at optimal doping in the 122 system come from substitution on the alkaline earth (AE) site. Early studies induced superconductivity by hole-doping the AE site (either Ca, Sr, or Ba) with an alkali metal (K or Rb) [45, 46, 47, 48] which produced transition temperatures as high as 38 K. Recently it has been shown that electron-doping on the AE site can produce an even higher T_c, up to 45 K in $Ca_{1-x}Ln_xFe_2As_2$ [49, 50]. The As site can also be substituted with phosphorus, which produces a remarkably clean system; this is currently

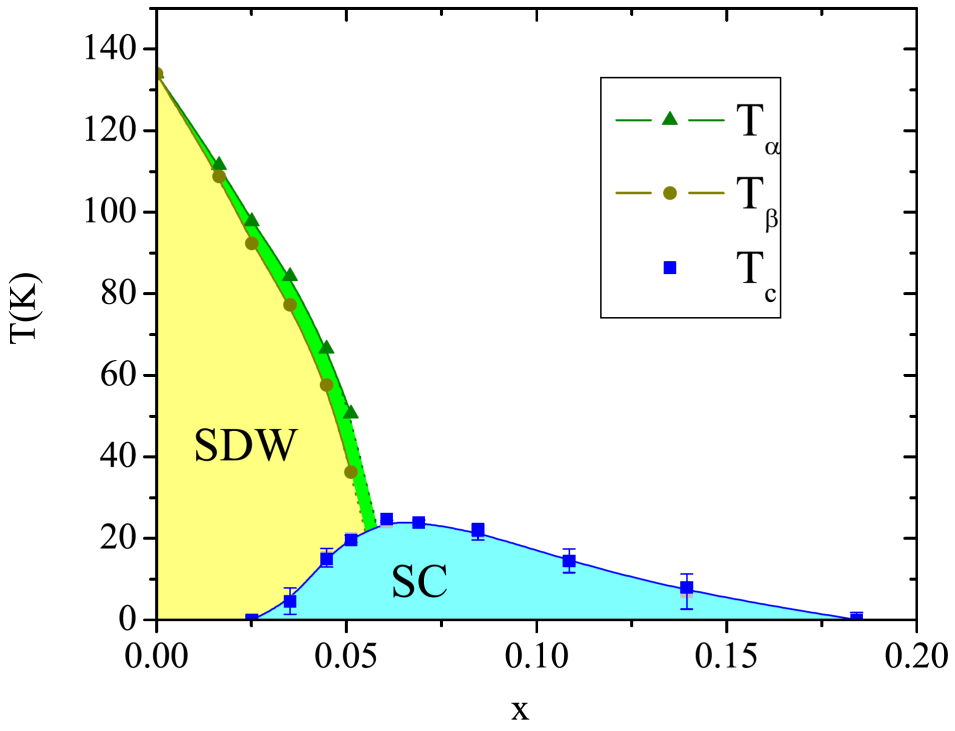

Figure 1.3: Phase diagram for $Ba[Fe_{1-x}Co_x]_2As_2$. The parent compound exhibits antiferromagnetism below 145 K, however this temperature decreases with chemical substitution. The optimal T_c is approx. 25 K in this system, one of the highest in the transition metal subsituted 122s (from Ref. [44]).

the only doped system with single crystals that can support quantum oscillations [51]. As in the case of substitution on the AE site, this produces a relatively high T_c of approx. 35 K which supports the observation that pairing is occurring in the Fe plane since doping outside of the plase should disrupt the superconductivity less and produce higher transition temperatures.

Finally, the most modifiable site seems to be the Fe site, into which most transition metals can be substituted. Indeed, the list of succefully grown single crystals includes systems doped with Cr, Mn, Ru, Co, Rh, Ir, Ni, Pd, Pt, Cu, and Zn (see references listed in Chapters 5 and 6). Interestingly, T_c in TM substitutes 122s have never been observed above 25 K, although different transition metal substituents produce transition temperatures as low as 4 K [21]. One can argue that this relatively low max T_c is due to disruptions in the the superconducting Fe plane. However this argument does not explain why the different substitution produces such a wide range of transition temperatures. One possible explanation for this invilves the pairing symmetry of the system: if the iron-based superconductors have a sign-changing pairing symmetry, this could cause lowering of the transition temperature. A brief discussion of the pairing symmetry is found in the next section and a more thorough explanation of this theory will given in Chapter 6.

1.2 Pairing Symmetry

The ultimate goal of most research groups studying superconductivity is to increase T_c to a temperature that is useful for potential applications. One way

to do this in principle would be to grow every material possible, including the infinite combinations of elements and allotropes thereof. This would be a time consuming and expensive process and almost certainly more efficient methods would be preferred.

A way to narrow this search for high-T_c superconductors would be to understand the pairing mechanism, that is, the interaction that causes electrons to be attracted and form Cooper pairs. In conventional low temperature superconductors this is phonons, and by searching for superconductors with higher Debye frequencies (as in the case of MgB_2) we can hope to increase T_c. However, in high temperature superconductors the pairing mechanism is yet unknown. In principle, once we understand the nature of the interaction that causes pairing we should be able to limit our search to materials that have similar (and stronger) interactions and thus would be expected to enhance the pairing strength and transition temperature.

To determine the pairing mechanism it is helpful to know the pairing symmetry of the material. In the original derivation of electron pairing by Cooper [52], he began with a simple model of two electrons in the Fermi sea with equal and opposite momentum (the lowest energy state). Here we use a similar derivation adapted from Refs. [33] and [53] as well as lecture notes from Profs. S. Anlage and V. Galitski. We start with a pair wavefunction of the form:

$$\psi = \sum_k g(\mathbf{k}) e^{i\mathbf{k}\cdot(\mathbf{r_1}-\mathbf{r_2})} \tag{1.1}$$

where g($\mathbf{k}$) are the weighting coefficients and the bolded $\mathbf{k}$ are wavevectors. If

we put this into the Schrödinger equation and rearrange to solve for g($\mathbf{k}$) we obtain:

$$g(\mathbf{k}) = \frac{\sum_{\mathbf{k}'} V_{\mathbf{k}\mathbf{k}'} g(\mathbf{k}')}{2\epsilon_{\mathbf{k}} - E} \tag{1.2}$$

where E is the energy eigenvalues, $\epsilon_{\mathbf{k}}$ is the plane-wave energy, and $V_{\mathbf{k}\mathbf{k}'}$ is the interaction, or pairing, potential. The symmetry of this pairing potential provides some insight into the pairing mechanism. Because the superconducting wavefunction determines the gap, $\Delta(\mathbf{k})$, the superconducting gap has the same directional dependence as g($\mathbf{k}$). Symbolically, this equates to:

$$\Delta(\mathbf{k}) \propto g(\mathbf{k}) \propto V_{\mathbf{k}\mathbf{k}'} \tag{1.3}$$

Alternatively, the superconducting gap, $\Delta_{\mathbf{k}}$, can be calculated using the second quantization formalism of BCS theory using creation and annihilation operators $c^{\dagger}_{\mathbf{k}}$ and $c_{\mathbf{k}}$ to count occupied electron states we can write the Hamiltonian of the superconducting state as:

$$H = \sum_{\mathbf{k}\sigma} \xi_{\mathbf{k}} c^{\dagger}_{\mathbf{k}\sigma} c_{\mathbf{k}\sigma} + \sum_{\mathbf{k}\mathbf{k}'} V_{\mathbf{k}\mathbf{k}'} c^{\dagger}_{\mathbf{k}\uparrow} c^{\dagger}_{-\mathbf{k}\downarrow} c_{-\mathbf{k}'\downarrow} c_{\mathbf{k}'\uparrow} \tag{1.4}$$

The first term in this Hamiltonian involves the number of pairs and the second term involves the creation of a pair with momentum $\mathbf{k}$ and the annihilattion of a pair with momentum **k'**. From here we can either use the variational method or use a canonical transformation to solve the Schrödinger equation, but both methods give the same relationship between the energy gap and excitation spectrum, $E_{\mathbf{k}}$:

$$\Delta(\mathbf{k}) = -\frac{1}{2}\sum_{\mathbf{k}'} V_{\mathbf{k}\mathbf{k}'}\frac{\Delta_{\mathbf{k}'}}{E_{\mathbf{k}'}} \tag{1.5}$$

From this one can show that (Ref. [33]:

$$E_{\mathbf{k}} = (\Delta_{\mathbf{k}}^2 + \xi_{\mathbf{k}}^2)^{1/2} \tag{1.6}$$

This gap need not be only positive values; it can be shown that the gap can have a phase factor and thus change sign along different momenta in the Fermi surface.

From either of these results we can see that Eqn. 1.3 holds and thus measuring the gap symmetry will give the pairing potential symmetry. For example, in the cuprates the crystal lattice is tetragonal (four-fold symmetric in the plane). Under a 90° rotation, if the gap does not change sign it will have the same symmetry as the lattice and is referred to as s-wave, taking the name from orbital structure. If, however, the gap changes sign under a 90° rotation, this would be an example of d-wave symmetry. One of the hallmarks of phonon mediated superconductivity is an s-wave pairing symmetry, meaning that the superconducting gap has the same symmetry as the crystal lattice. When it was discovered that the pairing symmetry in cuprates was d-wave (lower symmetry than the lattice) it was evidence that phonons were not the cause of pairing in those materials. In iron-based superconductors, the AFM ordering and lack of isotope effect points to a more exotic pairing mechanism, likely spin fluctuations [54, 55, 56, 57].

Measuring the exact nature of the Fermi surface in these materials is not

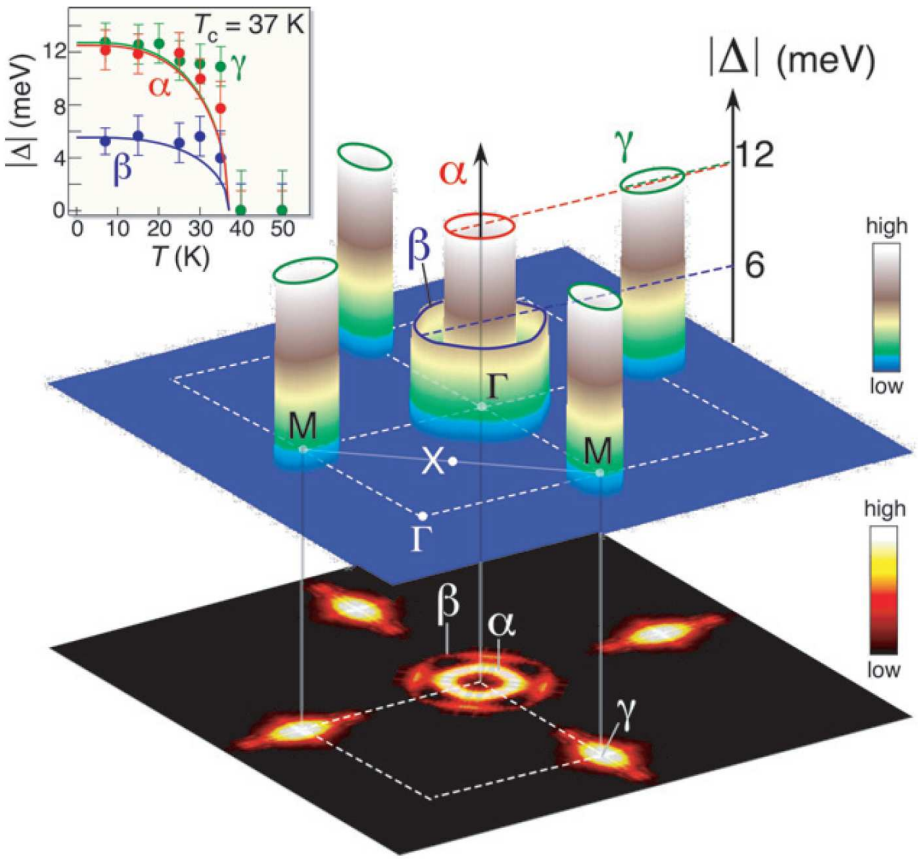

Figure 1.4: Fermi surface of $Ba_{1-x}K_xFe_2As_2$ determined by ARPES [58]. According to band structure calculations there are five bands crossing the Fermi energy: some (probably 3) hole-like bands around the Γ point (referred to here as the α and β sheets) and several (probably 2) electron-like bands around the M point (from Ref. [58]).

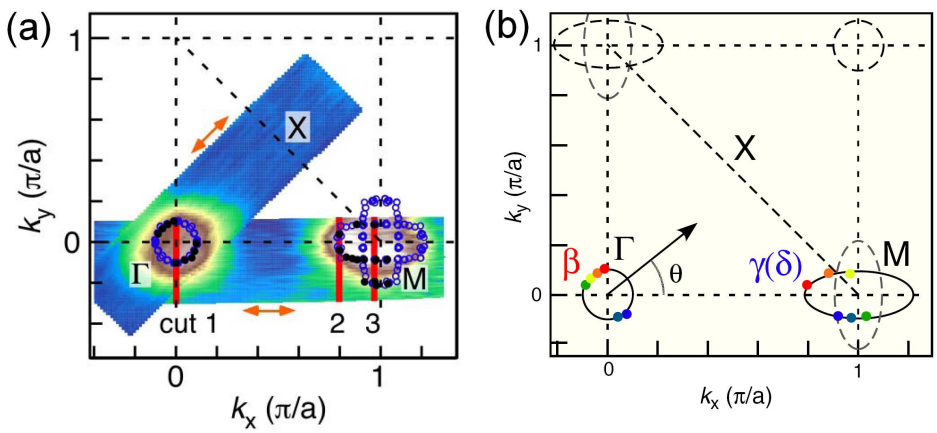

Figure 1.5: Fermi surface of $BaFe_{2-x}Co_xAs_2$ determined by ARPES [59]. As in the previous figure there are three hole-like bands around Γ point and two electron-like bands around the M point. The partial nesting of the bands may be responsible for the antiferromagnetism (from Ref. [59]).

easy. Band structure calculations show that the parent compound may have as many as five bands [37, 55, 60], however measurements have not been confirmed for all of these experimentally as several of them are overlapping. Angle resolved photoemission spectroscopy (ARPES) is one of the most direct ways to image the Fermi surface, however it suffers from being a surface-sensitive probe. Figures 1.4 and 1.5 present results of ARPES measurements on hole-doped [58] and electron-doped [59] $BaFe_2As_2$. The data shows two hole-like bands and one electron-like band for $Ba_{0.6}K_{0.4}Fe_2As_2$ and one hole band and two electron bands for $BaFe_{1.85}Co_{0.15}As_2$. It should be noted that the resolution is such that nearly degenerate bands would be indistinguishable.

Quantum oscillation measurements on the parent compounds, however, show a slightly different picture. While ARPES measurements show these bands as

quasi-two dimensional, Shubnikov-de Haas oscillation measurements of detwinned $BaFe_2As_2$ show one hole band and two electron bands that are three-dimensional and closed [61]. Despite slight discrepancies seen between different measurements, there are similarities between these results that have motivated theoretical studies. Hole-like bands are always observed at the Γ- point and electron bands at the M-point of the brillouin zone. Additionally, most of these studies show that the bands are somewhat two-dimensional and cylindrical. With hole doping, measurements show that the hole bands become larger; similarly, the electron bands increase in size with electron doping. This is not surprising, but it is reassuring.

In addition to multiple Fermi surfaces, there are also two superconducting gaps as measured by spectroscopic [58, 25] and thermodynamic [62, 63] studies. This combined with the Fermi surface described above leads to the the most commonly used picture when calculating superconducting properties of this system: one gap on the hole band at the Γ-point and the other gap on an electron band at the M-point. Figure 1.6 shows several possible symmetries that can exist with this band configuration (see reference [37]).

Early on it was proposed by several groups that there may be a sign change between the two gaps, what is now known as $s_\pm$ superconductivity [54, 55, 64]. While this seems to be the most popular pairing symmetry, others have not been ruled out, including d-wave [55] and a multiband s-wave without the sign change (often with the retronym s_{++}) [65, 60]. Finally, complicating all of this is the possibility of nodes in the gap. A d-wave symmetry would have symmetry-imposed nodes in the gap, however there can also be so-called "accidental" nodes: nodes that do not change the

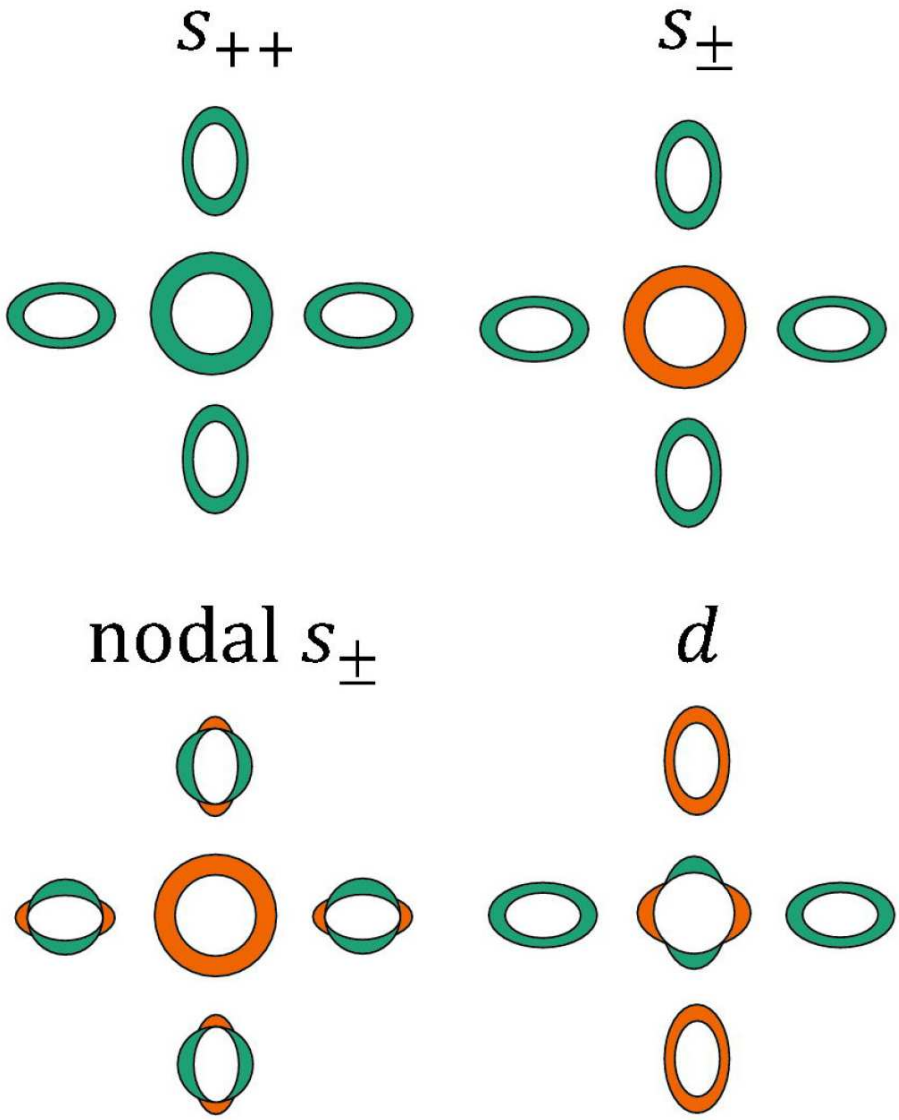

Figure 1.6: Possible pairing symmetries for multiband superconductors. The Fermi surface shown here is a simplified version of what may be present in iron-based superconductors, however it may be enough to capture some of the physics. There are two gaps around cylindrical Fermi surfaces: one at the Γ point and one at the M point, and there may be a sign change between them. It is possible, using this configuration, to have s-wave, d-wave, or a sign changing s-wave symmetry, any of which may have accidental nodes (from Ref. [37]).

symmetry (compare "$s_{\pm}$" to "nodal $s_{\pm}$" in figure 1.6). Calculations have shown that none of these can be ruled out energetically [66, 37], however thermal conductivity measurements show nodes in the c-axis but none in the plane for optimally electron doped 122s [67, 68]. Note that this includes most of the materials discussed in Chapters 5 and 6.

1.3 Open Questions

There are, clearly, still far more questions than answers for the iron-based superconductors. What is the pairing symmetry? Is it the s-wave or d-wave? Are there nodes? If so, are they seen in every material, or only some?

What is it that chemical substitution actually does to the crystal? Can it be described more accurately as chemical pressure, or is charge doping the correct picture? Is pressure alone (chemical or external) enough to induce superconductivity?

Finally, what is it that controls T_c in iron-based superconductors? Why do some systems have higher transition temperatures than other systems when there seems to be very little other difference between them?

In this thesis I attempt to address some of these questions. Chapter 2 covers the experimental techniques used in my various studies. Specifically, I discuss electronic transport properties, how they are obtained, and how they can be used to help determine the pairing symmetry. Chapter 3 covers my work on superconductivity in undoped $SrFe_2As_2$. There I show that under certain growth conditions superconductivity can be stabilized in a system where the magnetism has not been

suppressed. Although the volume fraction is low (typically less than 10%) this discovery shows that these systems are very close to superconductivity even in the undoped materials.

Chapter 4 covers substitution on the alkali earth site of the 122 family. I discuss the growth of solid solutions of $Ca_{1-y}Sr_yFe_2As_2$ and $Sr_{1-x}Ba_xFe_2As_2$ to determine the effects of chemical pressure on the electronic properties of the material. I show that chemical pressure alone is not enough to account for superconductivity in these systems, as is often claimed for isovalent substitution in the case of Ru substitution for Fe or P substitution for As.

In Chapter 5 I discuss transition metal substitution in 122s and question the nature of substitution and whether the charge doping picture is an accurate description. To this end I substitute Ni and Pt in to $SrFe_2As_2$ and observe superconductivity in both systems, then compare the transport properties to determine the different effects that similar transition metals have on the system.

Finally, in Chapter 6 look further into transition metal subsitution by discussing electronic transport properties from the literature as well as my own results. I use measurements of the transport scattering rate to answer the question of why the transition temperature varies greatly in these systems, and then use these measurements to place constraints on the pairing symmetry of the 122s.

Chapter 2

Experimental Details

In this chapter I discuss the experimental methods used in this thesis. First, I explain the techniques used to grow and characterize single crystals of iron-based superconductors. Next, I cover how and why I performed electronic transport measurements. Finally, I discuss what is meant by pairing symmetry and how we can use transport measurements to determine the symmetry of the system.

2.1 Sample Preparation

The first step in most of the low temperature measurements discussed in thes thesis is obtaining a sample with the desired properties. One possible way to probe the many interesting properties of strongly correlated electron systems is to grow our own materials. This affords the opportunity to tune the various properties of materials through chemical substitution to create systems with precisely the attributes or interactions that we want to measure. Chemical substitution can have many effects including carrier doping and chemical pressure, and it can introduce magnetic or nonmagnetic impurities and change the scattering in the system. Each of these effects can produce drastic effects on a material's properties, potentially revealing new and interesting physics.

2.1.1 Single Crystal Growth

There are many ways to grow crystals, but the flux (or solution) method of crystal growth is one of the most straight-forward ways to produce large single crystals. This process is remarkably simililar to how one would grow sugar crystals (rock candy) with water as the solvent: sugar is dissolved in hot water, then cooled. As the water cools, the solubility of the sugar in the water decreases and at the saturation point the sugar begins to crystallize. I used this same process here: the components of the desired crystal are placed in a nonreactive crucible and dissolved into a molten metal solvent called the flux. The solvent is heated to a temperature high enough so that the components of the desired crystal are dissolved, then as the flux is cooled the solubility decreases and the crystals begin to form. By choosing appropriate solvents and heat schedules large crystals can be grown, limited only by the size of the crucible.

To grow exceptionally clean crystals it is best to choose a flux that will not remain as inclusions inside the formed crystals. For this reason we chose a flux that would become part of the final crystal. This approach is referred to as the self-flux technique. For the 122 samples grown in this study I used the self flux technique and chose FeAs as the flux. Pure elemental iron (99.999%) and arsenic (99.99%) from Alfa Aesar were mixed in a ratio of 1:1 and sintered in a furnace at 700 C for 24 hours (see Fig. 2.1 for the Fe-As phase diagram). The reacted FeAs was then removed from the quartz tube, ground in a planetary ball mill until well powdered, then if necessary sealed back into the quartz tube and reacted again, the result of

which is binary FeAs. X-ray spectroscopy revealed a small amount (a few percent) of the impurities Fe_2As and $FeAs_2$, however this did not seem to be a problem for the growth.

In addition to FeAs, to grow transition metal substituted crystals we made binaries with the other elements, e.g. NiAs, CoAs, etc. PtAs did not form, however, so instead a mixture of $PtAs_2$ and elemental Pt was used as the flux to grow these crystals. The flux was then combined with the alkali earth element (Ca, Sr, or Ba) in a ratio of 1:4, with transition metal substitution occurring in the choice of flux. For example, to grow a batch of crystals with 5% Ni in place of Fe (as in $SrFe_{1.9}0Ni_{0.10}As_2$) you would use the ratio 1:3.8:0.2 for Sr:FeAs:NiAs. This mixture is again placed in a nonreactive crucible and sealed in a quartz tube under 1/4 atm. argon gas (Fig. 2.3).

A major consideration when growing large single crystals is the heat schedule. The idea of dissolving elements in a molten metal flux and slowly cooling it is simple enough, however if the phase diagram is complicated, many other compounds can form at different temperatures (see Fig. 2.1 for example). In the above example of sugar dissolved in water this isn't an issue, but when growing crystals with two or more elements, there are often other phases that can form at comparable or even higher temperatures than the desired crystals. For example, when growing $CaFe_2As_2$ in Sn flux $CaFe_4As_3$, called the 1-4-3 phase, forms preferentailly under some growth conditions. By changing the heat schedule and the ratio of Ca to FeAs this phase can be avoided [70]. The heat schedule for growing transition metal substituted 122 materials has been optimized to avoid these impurity phases: first the tube was

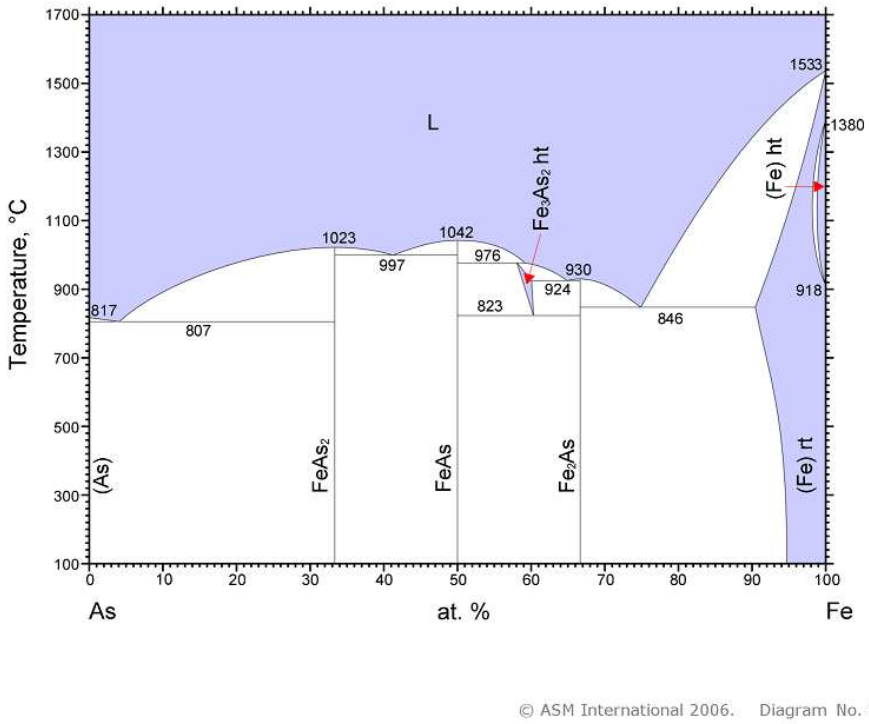

Figure 2.1: Binary phase diagram for Fe-As. Note that FeAs has a high melting point, 1042 C, which makes it difficult to decant or centrifuge the liquid flux, (from Ref. [69]).

heated above the melting point of FeAs (1042 °C) to approx. 1200 °C where it was held for some time, typically ∼24 h to make sure everything was dissolved. The material was then cooled slowly at a rate of 2 - 4 °C/hr to below the FeAs melting point at which point the tube was furnace quenched (Fig. 2.2).

Since FeAs has a melting point of 1042 °C, nucleation of the solid phase is expected to occur near to but above this temperature. For this reason the materials in the quartz tube are heated as high as possible to allow for the maximum amount of solute to dissolve in the flux. Unfortunately, quartz softens around 1200 °C, so one cannot go much higher than that without risk of breaking the tube. To help prevent the collapse of a slightly softened tube, 1/4 atm. of argon gas is added at room temperature (300 K) so that at 1200 °C (or 1473 K) the pressure inside the tube should be about 25% greater than the pressure outside the tube which will prevent the collapse.

After the solution is cooled to room temperature, crystals can then be removed from the flux by one of two ways: decanting or mechanical separation. During the process of decanting, the quartz tube is turned upside-down while still above the melting point of the flux, causing the flux to spill out of the crucible and away from the crystals which are typically attached to the side of the crucible. Quartz wool can be placed on top of the crucible to catch any crystals that might not remain attached to the crucible. The quartz tube may also be placed in a centrifuge and the centrifugal force can be used to remove more of the liquid flux than would be removed by gravity only. This process has the benefit of making it much easier to separate the crystals from the remaining flux after the growth, but it must be done

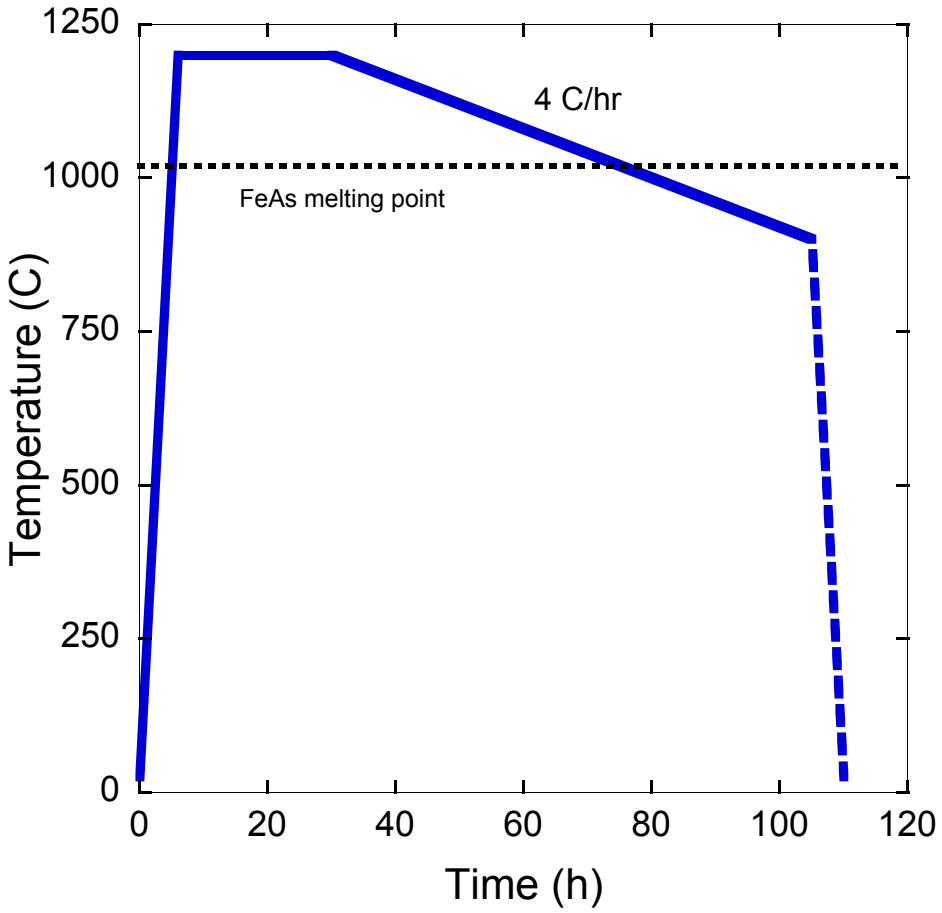

Figure 2.2: Typical growth schedule for 122 single crystals. The cooling rate is sometimes decreased to 2 °C/hr to increase crystal size, however I found that often a faster rate can still produce crucible-limited crystals.

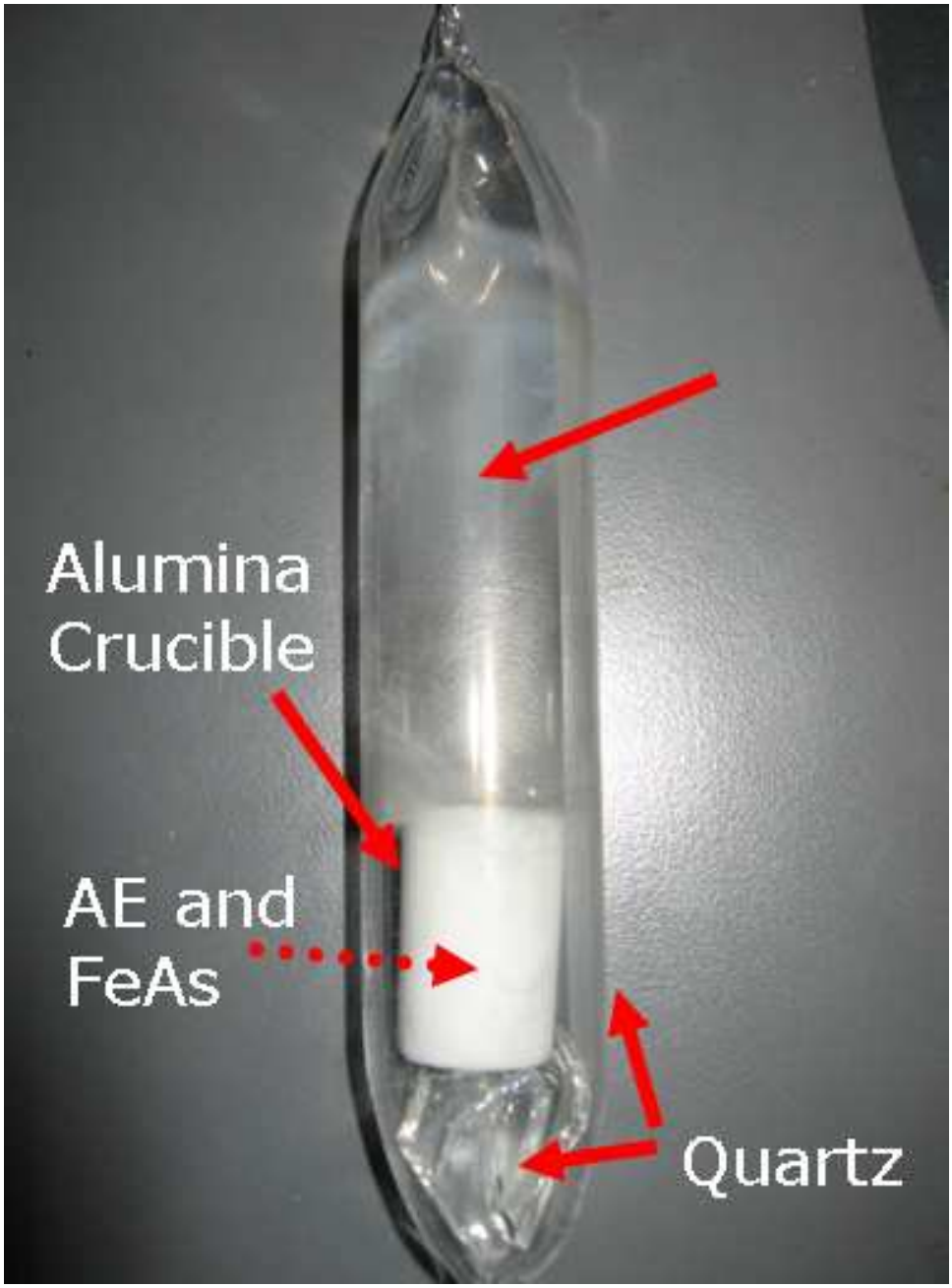

Figure 2.3: Single crystal growth tube before placing into furnace. Elemental components and FeAs flux are placed in an alumina crucible and sealed in a quartz tube under an inert Ar atmosphere. A small piece of quartz has been placed below the crucible to prevent the tube from cracking due to the unequal thermal expansion of the crucible and tube.

above the melting point of the flux which is 1000 °C in the case of FeAs. It can also add additional internal strain to the crystals from either the force from the centrifuge or the rapid cooling (called a quench) when the tube is removed from the furnace.

The other method of harvesting crystals is to cool the solution to room temperature and then mechanically separate the crystals from the hardened flux. This is the method most often employed by our group since it is safer than spinning a quartz tube at 1000 °C, both for the user and the batch of crystals. This method can also lead to internal strain in the crystal, in this case arising from the different thermal expansions of the crystal and hardened flux. Once cool, the quartz tube and crucible can be broken and the crystals can be removed easily from the solid flux and prepared for measurements. Fig. 2.4 shows a picture of a single crystal of Ni-substituted $SrFe_2As_2$ removed from the remaining flux using mechanical separation. The crystal face is 1 x 1 cm^2, much larger than is required for transport measurements. Such large single crystals of this size can be used for inelastic neutron scattering or other measurements that require large mass.

2.1.2 Preparing Samples for Measurement

Some measurements can give better results with certain shapes or sizes of crystals, so it is often important after the crystals are removed from the melt to cut them to the correct shape. Single crystals of iron-based superconductors with the 122 structure are ideal for transport measurements since they form in flat plate-like

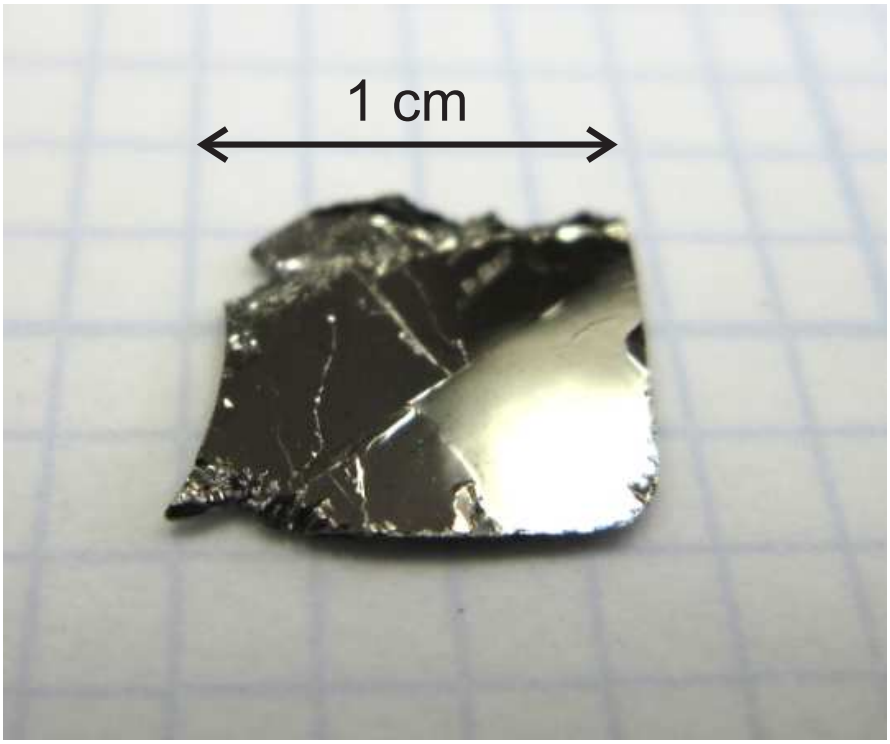

Figure 2.4: Photograph of a typical as-grown single crystal of $SrFe_{2x}Ni_xAs_2$ harvested from flux growth. The arrow shows the large platelet dimension, indicative of crystals limited by crucible size (from Ref. [5]).

shapes and can easily be cleaved to leave very thin samples with thicknesses less than 50 μm. In addition to cleaving easily, the samples can be cut to the correct size by placing a razor blade on top of the sample and tapping the razor with a hammer. For resistivity mesurements a long, thin sample produces a larger signal, while for Hall coefficient measurements only the thickness of the sample matters (see Section 2.4 for a full description of this). After crystals have been shaped they can also be resealed in a quartz tube and annealed if necessary, as in the case of Ni substitution in $SrFe_2As_2$ (see Section 5.1.2).

To measure the transport properties of a material good contacts must be made to the sample after it has been cut to shape. We typically use 50 μm diameter Au wires, however for small samples (less than 0.5 mm long) it is sometimes useful to use a thinner, 25 μm diameter wire. The two main criteria for judging the goodness of a contact are the contact resistance and the strength of the contact (*i.e.*, how much physical stress can be applied to the contact before it breaks).

When working with iron-based superconductors I employed several methods of making contacts:

Silver epoxy - Two-part silver epoxy (EPO-TEK H20E) can be used to provide mechanically strong contacts to samples. Unfortunately, contacts made using this method usually have high contact resistances (tens of ohms at room temperature) and the epoxy must be cured before it solidifies. The curing can be done slowly at 100 °C for 2 hours or quickly at 175 °C for 45 seconds, depending on whether higher temperatures can damage or oxidize the sample. The curing time not only makes this a relatively slow contact method, but leaves the samples exposed to air

and heat for a long time which causes oxidation.

Silver paste or paint - The most common contact method employed is to use silver paint or paste (Dupont 4929N) that hardens quickly in air and provides good electrical contact. The contact resistance at room temperature is typically $\sim 1\ \Omega$ and decreases with temperature, however the contact strength is weak and contacts can fall off the sample if manipulated too strongly. Additionally, if the surface is slightly oxidized, the contact resistance can increase to tens or hundreds of ohms. The benefit of this technique is that contacts can be made quickly and at room temperature which decreases surface oxidation. Contacts made in this way can also be removed with acetone or ethanol which is particularly useful if a sample needs to be annealed at high temperatures or measured using a technique that does not require contacts such as magnetic susceptibility or specific heat. Additionally, characterization using x-ray diffraction or wavelength dispersive spectroscopy (section 2.2) is more accurate if contacts are not present.

Solder - Soldering is a good method for making permament contacts with relatively low contact resistance. The contact resistance is less than $0.5\ \Omega$ at room temperature and can give be much lower at low temperatures (essential for low noise measurements at dilution refrigerator temperatures). The contacts are also quite strong and can withstand a considerable amount of manipulation without breaking. This permanence can be a problem, however, since contacts cannot be removed or repaired easily; occasionally while attaching wires to a sample, two contacts that are close together can accidentally short together if the user is not careful enough or the sample is very small. With silver paste or epoxy the contacts can be washed

away with a solvent, however with solder the sample must be discarded and a new one prepared.

Soldering iron-based superconductors in the 122 family is not difficult since the crystals are typically large (larger than 2 mm) however the correct combination of solder and flux must be used to properly wet the surface. For 122 materials I used the standard 60% Pb/40% Sn solder and Indalloy #2, an aggressive flux that is often used to solder to stainless steel.

2.1.3 2, 4, and 6 Probe Techniques

Depending on the type of measurement and size of the crystal there are several orientations for contacts (illustrated in Figure 2.5):

Two Probe – [Fig. 2.5(a)] The two-probe technique is usually only used on samples that are so small that one can only fit two contacts, for example the RuthOx (RuO_2) thermometer used in the dilution refrigerator. The problem with this technique is that the measuremed resistivity will include the contact resistance. While this is not much of a problem for a RuthOx thermometer which has a resistance between 2 and 20 kΩ and a contact resistance of less than 1 Ω, the error in measurement becomes a very large problem when measuring the resistivity of iron-based superconductors that have resistances less than 1 Ω and comparable contact resistances.

Four Probe Longitudinal – [Fig. 2.5(b)] This is the preferred technique for measuring resistivity. Four contacts are applied to a bar-shaped sample; the two

outer contacts are used to drive a current while the two inner contacts pick up the voltage drop. A voltmeter has a high input impedence so that most of the current should flow through the sample and not the voltmeter. For this reason the contact resistance of the voltage leads can be ignored since there should be very little current flowing through the voltage leads and thus little voltage drop across them. In this way the resistance of the contacts is excluded from the measurement, which is why this is the preferred method to accurately measure the resistance of low resistance samples.

Longitudinal resistivity, ρ_{xx}, is obtained by measuring the resistance of the sample and then multiplying by a geometric factor, α:

$$\begin{aligned} \rho_{xx} &= R_{xx}\alpha \\ &= \frac{V_x}{I_x}\frac{t \cdot w}{l} \end{aligned} \tag{2.1}$$

where t, w, and l are the sample thickness, sample width, and distance between the voltage contacts, respectively. For more details on how the resistance is measured, see section 2.4.

Four Probe Transverse – [Fig. 2.5(c)] This is the preferred method for measuring the Hall coefficient, or transverse resistivity. Again, four contacts are made, however in this method the preferred shape is more plate-like to allow space for the transverse voltage contacts. For best results, the voltage contacts should be as close to perpendicular to the current leads as possible to reduce the effect of longitudinal resistance, however this longitudinal contribution can be removed by

antisymmetrizing the data as described in section 2.4.3.

From Ashcroft and Mermin [71], we can see that the Hall coefficient is just the slope of the transverse resistance, R_{xy}, as a function of magnetic field multiplied by the thickness of the sample:

$$\begin{aligned} R_H &= \frac{E_y}{j_x \cdot H} \\ &= \frac{V_y/w}{I_x/(w \cdot t \cdot H)} \\ &= \frac{V_y}{I_x}\frac{t}{H} \\ &= R_{xy}\frac{t}{H} \end{aligned} \tag{2.2}$$

From this expression we can see that thinner samples provide a larger transverse resistance which is easier to measure accurately.

Six Probe – [Fig. 2.5(d)] This method is a combination of the longitudinal and transverse techniques described above. Six contacts are made to the sample - two for the current, two for the longitudinal resistivity and two for the transverse resistivity. The advantage of this method is that it enables us to simultaneously measure transverse and longitudinal resistance. By doing so, errors due to the measurement of sample thickness are cancelled out in calculations of the scattering rate. To see this more clearly I substitute the results from Equations (2.1) and (2.2) into the transport scattering rate (see Equation (2.20)) obtained later in section 2.4.4:

$$\Gamma = \frac{e\rho_{xx}}{m \cdot R_H}$$

$$= \frac{e \cdot R_{xx} \frac{w \cdot t}{l}}{m \cdot (R_{xy}/H)\, t}$$
$$= \frac{e \cdot R_{xx} \frac{w}{l}}{m \cdot (R_{xy}/H)} \tag{2.3}$$

Equations (2.1), (2.2), and (2.3) imply that accurate measurements of the geometric factor are needed to calculate the resistivity or Hall coefficient from the measured resistance. In this study the geometric factor is measured by using an eyepiece for the microscope that has divisions etched into it (made by Leica for their microscopes) and by looking through this eyepiece the size of the sample can be determined. With the miscoscope on the lowest power I was able measure up to 5 mm with 50 μm divisions. At higher power, the resolution can be as fine as 6 μm. Typical sample dimensions are 1.0 $\times$ 0.5 $\times$ 0.1 mm^3 so the largest source of error is the measurement of sample thickness. Additionally, because iron-based superconductors are layered and cleave very easily, layer decoupling or delamination is another potentially large source of systematic error in thickness measurements. Because of this potentially large error, many samples must be measured before an absolute resistivity can be given, however scattering rate measurements performed using the 6-wire technique do not suffer from this problem because the thickness cancels our when calculating the transport scattering rate. For this reason I use this technique in chapter 6 to obtain accurate measurements of the scattering rate.

2.2 Characterization

A material typically becomes vastly less interesting to researchers if it has properties that have already been reported and are well understood, also, it is best

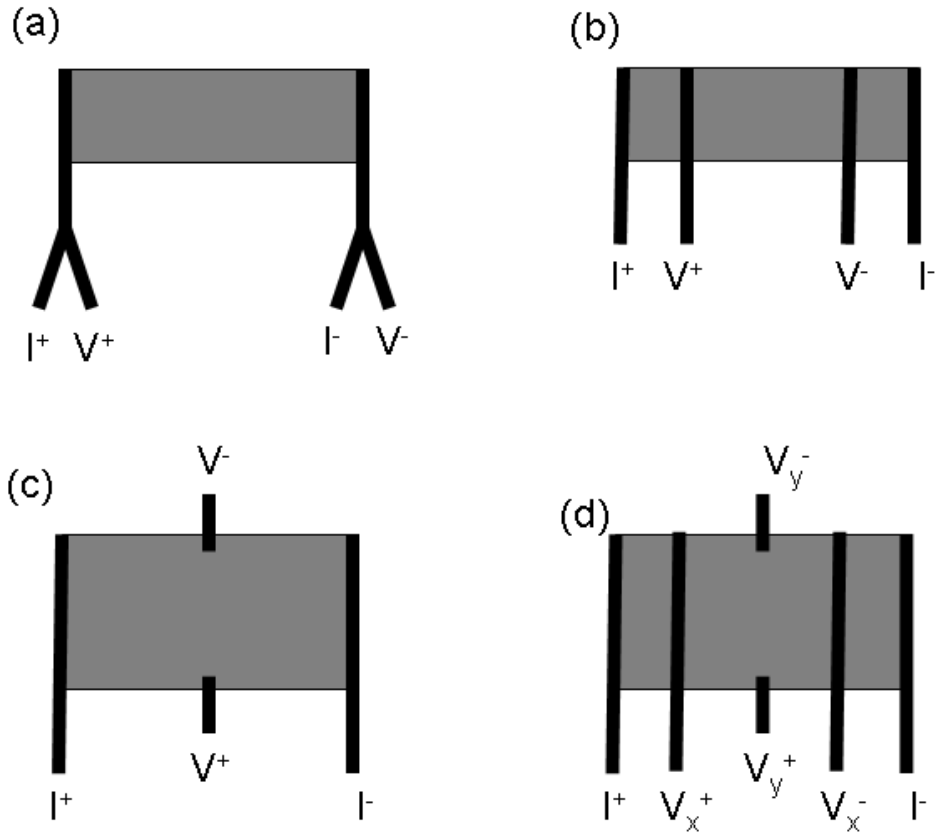

Figure 2.5: (a) 2-wire, (b) 4-wire longitudinal, (c) 4-wire transverse, and (d) 6-wire measurement configurations for electrical transport measurements.

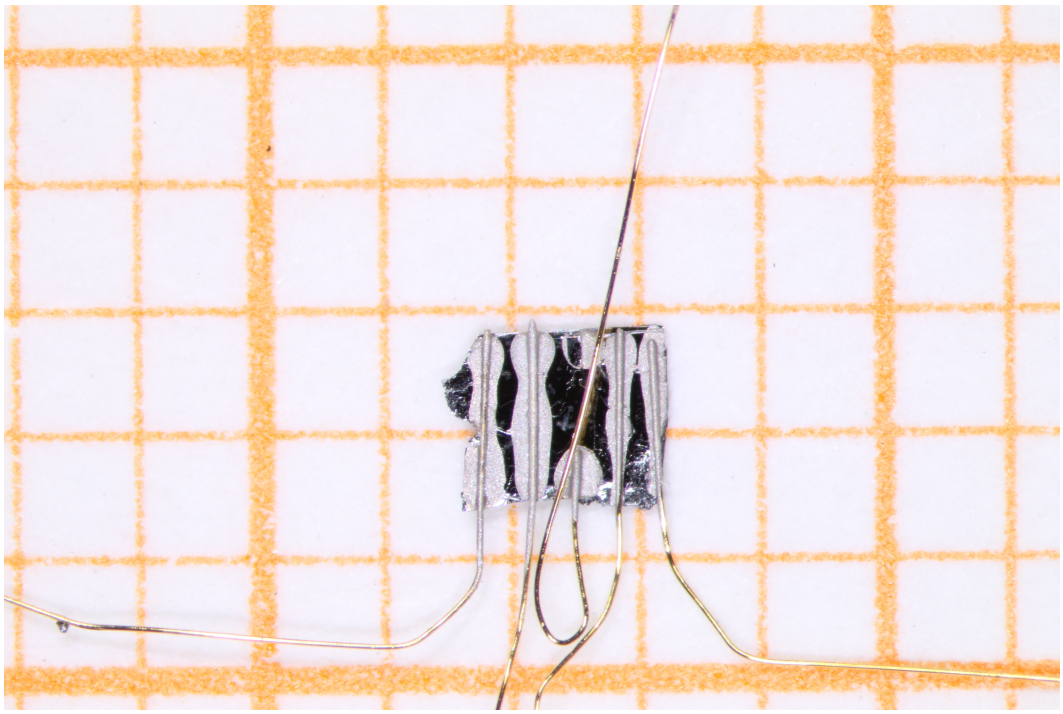

Figure 2.6: Picture of sample $SrFe_{1.80}Pd_{0.20}As_2$ B33 6W1 showing 6-wire lead configuration.

to know precisely what you are measuring before you begin. As was previously mentioned in section 2.1.1 it is often possible to grow unintended crystal phases, such as the $CaFe_4As_3$ phase, or for the the actual level of substitution to vary greatly within a batch of crystals (as in the case of Pt-substituted $SrFe_2As_2$, see Chap. 5). In this section I also discuss how I obtained the crystallographic information. For an example of the importance of crystal structure, see chapter 4 for discussion of how bond angles affect the properties of 122s.

2.2.1 X-ray Diffractometry

There are three techniques that are most often used by our group o determine the crystal structure of samples:

Powder diffractometry - The most frequently method of crystallography used by our group is powder diffraction. To this end, we use a Bruker D-5000 diffractometer and employ the Cu Kα emission line. Single crystals are collected, powdered, and attached to microscope slides using petroleum jelly. This technique is preferred because it can be used to obtain lattice parameters in all directions simultaneously, however it is destructive of your samples and requires a relateive large amount of powdered material to get a large signal at the detector.

Single crystal x-ray diffraction (reflection) - This method is preferred for obtiaining limited information about a single crystal without destroying the sample. This method involves attaching a single crystal to a microscope slide, I used a Bruker D-8 diffractometer to determine the lattice constant normal to the surface - in the

122 materials this is the c-axis lattice constant. I use the D-8 for this measurement because the sample stage can be rotated to obtain the peak from a single crystal, however the down side to this method is that only the lattice constant for one direction can be obtained at a time.

Single crystal x-ray diffraction (transmission) - Transmission x-ray spectroscopy is the most powerful method for structural refinement employed by our group. P. Zavalij, a crystallographer in the Chemistry Department [72] did this characterization for our group. Transmission x-ray spectroscopy was performed using a Bruker Apex2 diffractometer. A full description is outside the scope of this thesis, however it should be noted that this technique will be important in Chapter 3 in which I discuss superconductivity in undoped $SrFe_2As_2$ arising from lattice distortion.

2.2.2 Energy- and Wavelength Dispersive X-Ray Spectroscopy

To determine the elemental composition of single crystals I typically used one of two similar methods: energy dispersive x-ray spectroscopy (EDS or EDX) and wavelength dispersive x-ray spectroscopy (WDS or WDX). For EDS measurements a Hitachi S-3400 Variable Pressure Scanning Elelctron Microscope was used to generate a high energy (keV) beam of electrons. When a sample bombarded with the electrons it emits characteristic x-rays that can be analyzed to determine the chemical composition using the EDS analyzer attachment on the Hitachi SEM [73]. It is important to realize that EDS can give false or ambiguous results since several different kinds of atoms can have peaks at approximately the same energy.

In WDS the characteristic x-rays are diffracted before being analyzed and thus only photons of a specific wavelength are measured at one time. This method provides better spectral resolution than EDS and is considered the more accurate of the two techniques. However, as with reflection vs. transmission x-ray spectroscopy discussed in the previous section, the strength of the EDS measurement is that it can provide useful results quickly and can be performed by members of our group, whereas crystals are given to technicians in the NanoCenter for WDS measurements. For this reason EDS is more often employed by our group for early characterization, and WDS is used for more detailed studies.

2.3 Temperature and Magnetic Field Control

In this section I describe the techniques and equipment used for producing the field and temperature environment necessary for my measurements. The lowest temperature reached in this study was 1.8 K, which is simple enough to achieve using liquid ^{4}He (LHe). The boiling point of ^{4}He is 4.2 K, so to reach lower temperatures one must pump on the vapor from the cryogen and thereby decrease the temperature by evaporative cooling. To reach high or intermediate temperatures requires the careful application of heat. To control the temperature I balanaced the cooling power of the liquid helium against the applied heat from a resistive heater. Fortunately there are several systems available to use that simplify (or at least automate) the process of temperature control.

2.3.1 Physical Properties Measurement System

The Physical Properties Measurement System (PPMS) by Quantum Design is a versatile system that I used to control the sample environment as well as measure the longitudinal and transverse resistivity of materials. The principle of cryogenic operation behind the PPMS is that it pulls liquid helium (^{4}He) into a small pot from a main bath, and then pumps on that bath to lower the pressure, thereby lowering the temperature. The operation is similar to that of a dipper probe (sec. 2.3.3) that is also used in this study, but there are a few proprietary differences with how the helium is let into the pot [74]. The lowest temperature that can be achieved is approximately 1.8 K and temperature stability can be achieved up to 300 K. The PPMS also can have a superconducting magnet installed. At the University of Maryland we have two PPMS's; one can apply magnetic fields up to 9 T whiile the other can reach 14 T.

After wires are attached to a sample, the sample can be mounted to a sample platform, or "puck", that can be inserted into the dewar for transport measurements. Typically I used the AC transport option and measured the resistance of two samples simultaneously [75]. The PPMS uses the Model 6000 resistance bridge to accurately measure resistances below 1 mΩ, which is especially useful for very small or highly conductive samples.

2.3.2 Magnetic Properties Meaasurement System

Magnetic susceptibility measurements were performed in a Magnetic Properties Measurement System (MPMS) built by Quantum Design [76]. The MPMS uses a Superconducting Quantum Interference Device (SQUID) to measure the change in magnetic flux through a pickup loop as a sample is drawn through it. Samples are placed in a drinking straw or other long, uniform sample hold with minimal background, and a small magnetic field is applied (typically 1-100 mT). A small magnetic moment forms in the sample in response to the applied field and the sample is then pulled through the SQUID loop, creating a variation in the magnetization that can be measured [76]. The output voltage from the SQUID readout can be converted into the magnetic moment of a sample or the susceptibility (χ = M/H). Like the PPMS, the MPMS can reach temperatures as low as 1.8 K, while the maximum field is 7 T.

Magnetic susceptibility measurements are only discussed in passing for most of this thesis and are typically only used to show that there is in fact a full volume fraction of the sample exhibiting superconductivity. However, these measurements will play an important role in chapter 3 where I use susceptibility data to show that the superconducting volume fraction is correlated with lattice disorder.

2.3.3 Dipper Probe

For some measurements to provide temperature control I ised a 2K dipper probe built by Cryomagnetics. The principle of operation is similar to the PPMS:

a small (needle) valve is used to draw liquid helium from a bath into a 1K pot. A pump is then used decrease the pressure (and temperature) of the liquid in the pot, cooling the system to a base temperature of 1.8 K. A tail (Fig. 2.7) with the samples to be measured is attached to the 1 K pot. A heater and thermometer are attached to the tail as well to adjust and measure the temperature of the tail. There are 42 experimental wires running from the samples up to the top of the cryostat that are made of a high resistance material (Constantan) to minimize the heat transfer from room temperature to the tail.

We use a Cernox thermometer to measure the temperature of the system. The resistivity of the thermometer increases monotonically with decreasing temperature so that the temperature of the system can be given as a function of measured resistance of the thermometer. To measure the resistance of the thermometer we use a Lakeshore Model 336 resistance bridge (LS336), which is similar in operation to the LS370 described in sec. 2.4.1. The LS336 also provides temperature stability by controlling the amount of power applied to the heater. The PID settings were determined through trial and error. The LS336 accepts a resistance setpoint and will apply heat to the system until the temperature stabilizes at the setpoint.

2.3.4 15/17 T Superconducting Magnet

In many of my measurements, I need to apply a magnetic field. The magnetic field comes from a superconducting solenoid built by Oxford Instruments and can reach 15 T when in a 4.2 K LHe bath. If the temperature of the bath is reduced

to 2.2 K (by decreasing the pressure over the bath), the magnet can reach 17 T. Because superconducting magnets have zero resistance, a large, constant magnetic field can be held indefinitely.

The magnet has a field-compensated (i.e. zero field) zone approximately 12 inches above the center of the magneti so that one can measure the resistance of a thermometer without concerns about errors arising from the magnetoresistance. The 1 K pot of the dipper probe nomally resides in the field compensated zone, so to put the samples in the center of field samples are attached to a "tail" that extends into the field region. The tail is a solid piece of OFHC copper that has been machined into a "shovel" shape (built by the company eMachine Shop, see Fig. 2.7) to allow for the maximum amount of surface area for the samples while minimizing eddy currents that could heat the system.

2.4 Electronic Transport

The motion of electrons in a metal can be described approximately using the free electron model proposed by Drude [71]. This model treats electrons in a metal as a gas of independent particles that move without interactions until they collide with defects or each other. This model assumes that electrons are hard spheres and that there is a time, τ, between collisions that is characteristic of the material. At low temperatures in the normal state, this relaxation time is a measure of impurities and will be discussed later in this chapter. The Drude model, while effective at describing the conductance of metals at room temperature, drastically

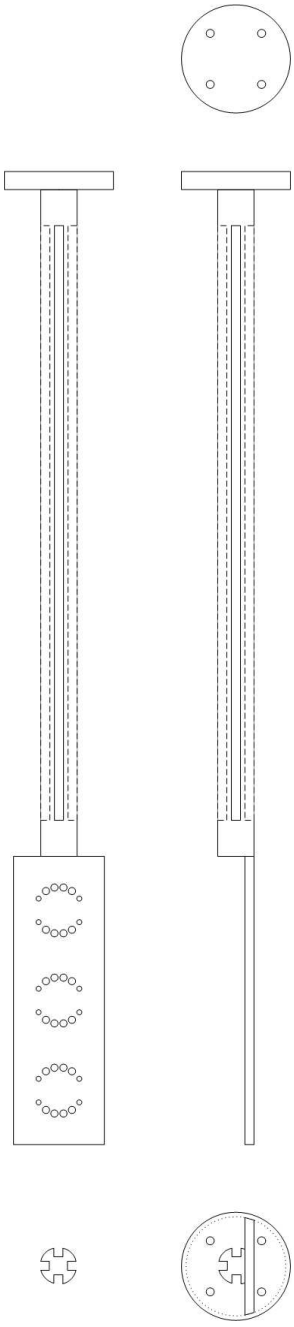

Figure 2.7: Schematic drawing of dipper tail. Tail is approximately 12" long and 1.5" wide. Grooves are cut in the side to minimize the area for eddy currents. See my lab notebook for full details.

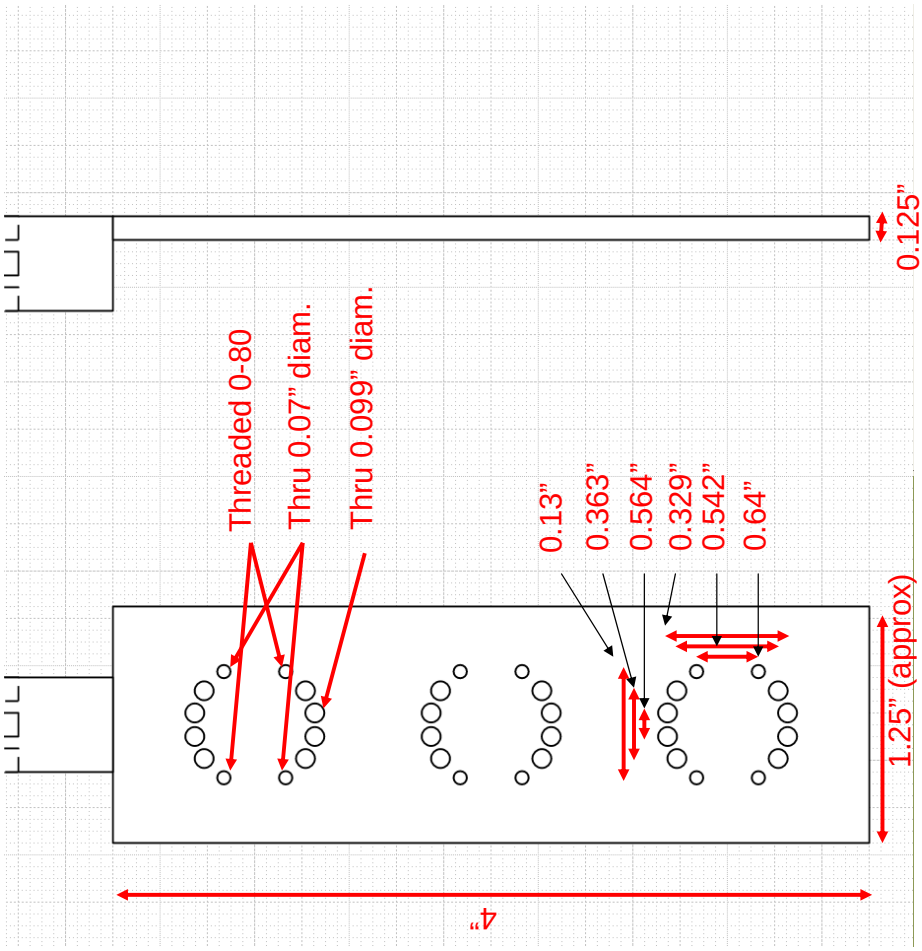

Figure 2.8: Schematic drawing of dipper tail zoomed in on the head where samples are attached. Through holes are cut in the plate to accommodate the pins for a He-3 PPMS puck.

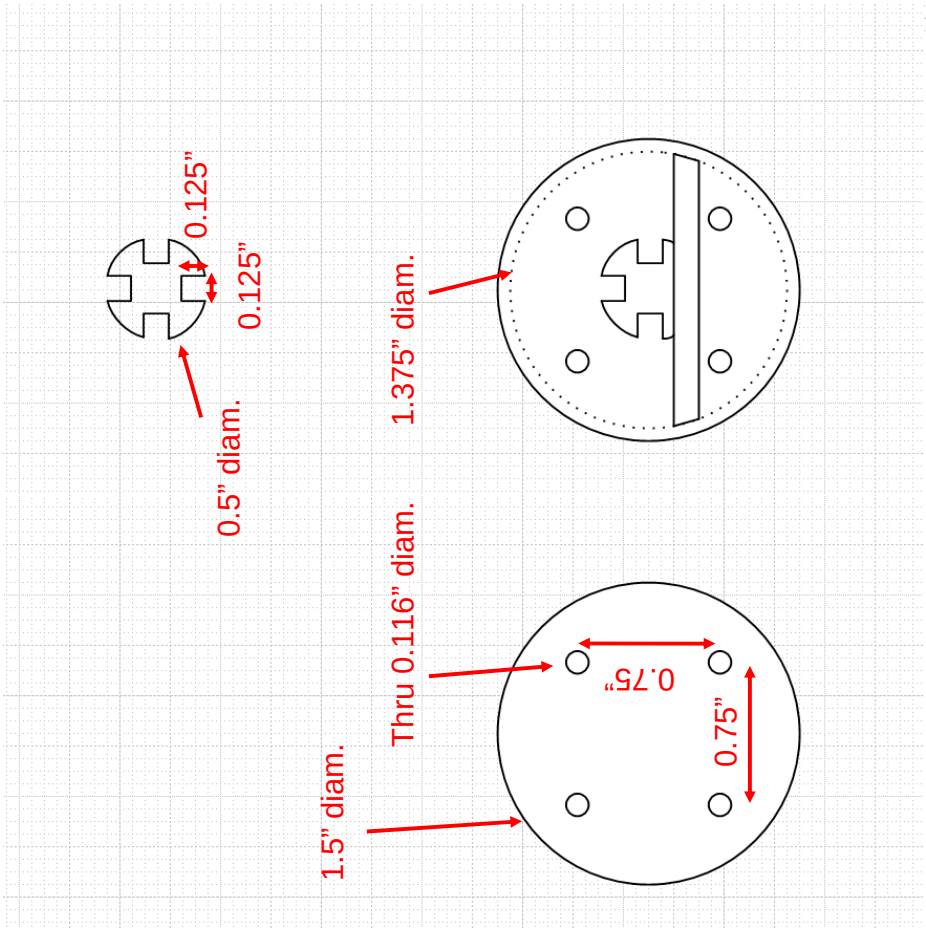

Figure 2.9: Schematic drawing of dipper tail zoomed in on the bottom where the tail attaches to the 1 K pot. This configuration of holes is designed for the Cryomagnetics 1 K dipper probe. For the dilution refrigerator an adaptor is needed.

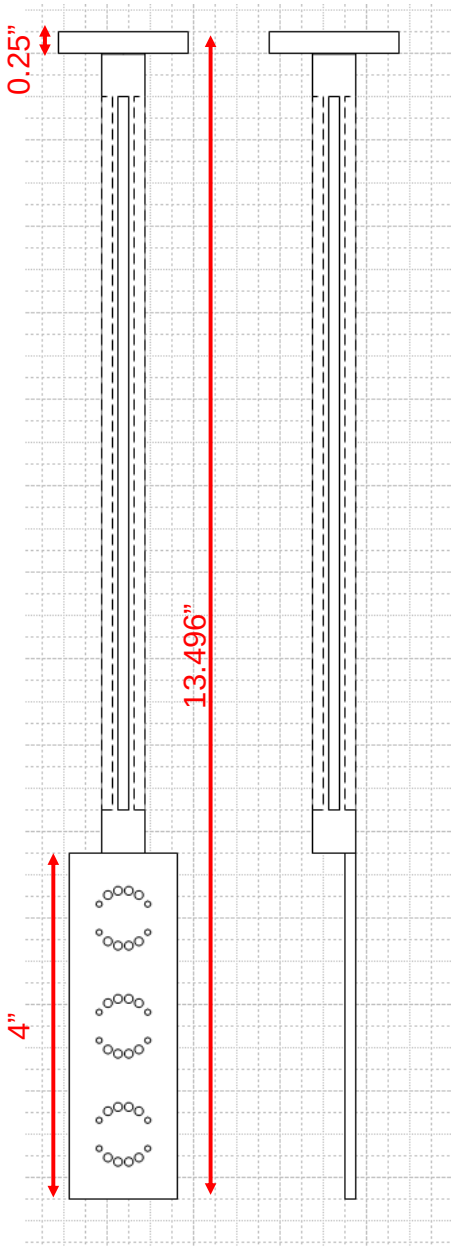

Figure 2.10: Schematic drawing of dipper tail; side view. The tail is designed so that the center of the 4-inch head is in the center of the magnetic field.

overestimates the specific heat (by about 100 times), and underestimates the drift velocity (by approximately a factor of 10) [77]. This problem was solved by Sommerfeld developed a better model by replacing the Maxwell-Boltzman distribution with the Fermi-Dirac distribution to take into account the Pauli exclusion principle. In Sommerfeld's model, instead of every electron conducting heat, only electrons near the Fermi surface contribute to the conductance, far fewer than in the single Drude model.

At first glance it is surprising that electrons can behave as if ther were weakly interacting. Negatively charged electrons are moving through a lattice of positive ions that are in turn surrounded by negatively charged shells of valence electrons. This realization leads to Fermi liquid theory in which electrons are pictured as being in a sea. With the addition of energy, quasiparticles are excited out of the sea into unoccupied states and contribute to the transport properties of a system. These quasiparticles have spin 1/2, however they can have an effective mass that is very different than the mass of bare electrons [78]. In iron-based superconductors, the effective mass is approximately 2 m_e [79, 61, 80].

2.4.1 AC Resistance Bridges

Measurements of the electrical conductivity provide a direct measure of the charge carriers and have the benefit of being one of the simplest measurements to perform. In this section I derive equations for transport properties and discuss the equipment and measurement techniques I used to measure resistance. Accurate

resistivity measurements are important to low temperature physics: in addition to measuring the properties of a material, we also use resistance measurements of thermometers to determine the temperature of the system.

A resistance bridge (or Wheatstone bridge) is a circuit where three well-known resistors are balanced with a fourth, unknown resistor to determine its resistance. By adjusting the resistance of one or more of the known resistors, you can effectively change the resistance range over which the measurement is accurate. This is the main principle behind the operation of the Lakeshore model 370 AC resistance bridge (LS370) that I used frequently [81] when not using the PPMS (see section 2.3.1).

The LS370 uses a low frequency AC signal to minimize the effects of lead capacitance and thermopower of leads and a lock-in amplifier to accurately measure resistance up to 2 MΩ and down to 2 mΩ. The LS370 offers two resistance ranges per order of magnitude in exponential steps: 2 Ω, 6.32 Ω, 20 Ω, 63.2Ω, *etc.* By choosing the appropriate resistance range for the sample/thermometer under test, the accuracy of the measurement is greatly increased.

According to the LS370 manual the accuracy may be as good as ±0.03%, although this can be enhanced by using one of the scanners. To measure more than one channel at a time, the LS370 can be combined with a scanner (multiplexer) that can switch between as many as 16 channels. We have two scanners: model 3716L and 3708. The 3716L scanner can switch between 16 channels and it is optimized for low-resistance samples. The 3708, however, is optimized for ultra-low resistance samples and can provide an even lower-noise measurement than the 3716L. Both scanners leave unused leads floating which facilitates 6-wire measurements.

2.4.2 Longitudinal Resistivity

Longitudinal resistivity measurements are the cornerstone of my electrical transport measurements. The resistivity of a material includes information about the effective mass of the quasiparticles, the scattering rate, and the carrier density. The equation of motion for an electron in an electric field, ε, is:

$$\vec{F} = m\vec{a} = m\dot{\vec{p}} = -e\vec{\varepsilon} - \frac{\vec{p}}{\tau} \tag{2.4}$$

In the steady state where $\dot{\vec{p}}$=0 we see that $\vec{p}$ = -e $\vec{\varepsilon}\tau$ and thus the drift velocity is given by:

$$\vec{v}_D = \frac{-e\tau}{m}\vec{\varepsilon} \tag{2.5}$$

The current density, $\vec{j}$, is the number of charges moving through a given area and can be calculated with the drift velocity and charge density, n:

$$\vec{j} = -ne\vec{v}_D = \frac{ne^2\tau}{m}\vec{\varepsilon} = \sigma\vec{\varepsilon} \tag{2.6}$$

Where σ is the conductivity:

$$\sigma = \frac{ne^2\tau}{m} \tag{2.7}$$

σ is a function of the carrier concentration, n, and scattering time, τ. This will become more important when we calculate the scattering rate, Γ.

Many interesting effects can be detected by performing resistivity measurements that are outside the scope of this dissertation. However, the following examples come up in the course of my discussion of iron-based superconductors:

Phase transitions - Some signature of phase transitions can be seen in transport measurements. For example, if a material enters the superconducting state, we see resistivity drop to zero. A we will see in later chapters, magnetic and structural transitions can also lead to a sharp change in the resistivity. In fact, both magnetic and structural transition temperatures can be determined from resistivity measurements [82]. The resistivity can either decrease or increase through a magnetic transition because of a change in the number of carriers or the magnetic scattering. We will see both kinds of behavior in the 122 family.

Residual resistivity - The resistivity at room temperature is determined mainly by phonon scattering and is relatively insensitive to impurities. As we approach zero temperature, however, the resistivity becomes limited by impurities which provide scattering centers and shorten the scattering time, τ [83, 84]. The zero temperature resistivity (residual resistivity, ρ_0) is strongly dependent on impurities and as such can be used as a measure of crystal quality. Since the room temperture resistivity is roughly impurity-independent, crystal quality can be determined by the quantity R(300K) / R(0K), also known as the residual resistivity ratio, or RRR. Pure samples of good metals can have a RRR larger than 1000, however most of the transition metal doped 122s would be considered dirty with RRR values ~ 2. A much cleaner but closely related system, optimally doped $BaFe_2As_{2-x}P_x$, can have a RRR larger than 20, indicative a mean free path long enough to see quantum oscillations [85].

Temperature dependence - The temperature dependence of a material's resistivity can often be used to determine the dominant scattering mechanism in the system. At high temperatures (above $\theta_D/2$) one expects a resistivity linearly pro-

portional to temperature due to electron-phonon scattering. At low temperatures, however, one can see a variety of different temperature dependencies. Electron-phonon scattering (Umklapp scattering) has a T^5 dependence and is observed in very clean metals but only at the lowest temperatures. Electron-electron scattering is observed more frequently and has a T^2 dependence that comes from the fact that electrons can only be scattered into vacant states. Both the number of available electrons near the Fermi surface and the number of vacant states are proportional to $kT^*n(E_F)$ so that the probability of scattering becomes $(kT^*n(E_F))^2$[84].

Behavior that deviates from the T^2 dependence is often taken as a sign of some other interesting physics. Resistivity that is linear down to low temperatures is often observed near superconductivity and some groups have argued that this can be used as a sign of quantum critical behavior. This linear behavior has been observed in cuprates [86], heavy fermions [87], organic superconductors [88], as well as in iron-based superconductors. For example, a correlation between T_c and T-linear resistivity was observed in $Sr_{1-x}K_xFe_2As_2$ [89].

2.4.3 Transverse Resistivity in Magnetic Fields

In a magnetic field, particles of charge q feel a Lorentz force **F** perpendicular to the magnetic field and velocity of the particle, where $\mathbf{F} = q\ \mathbf{v} \times \mathbf{B}$. This force is also felt by charge carriers in a conductor. The results is that a material placed in a magnetic field will develop a voltage perpendicular to the current [71]. This is just the two-dimensional version of eqn. 2.4 which we can write as:

$$\frac{d\vec{p}}{dt} = -e(\vec{\varepsilon} + \frac{\vec{p}}{m} \times \vec{B}) - \frac{\vec{p}}{\tau} \tag{2.8}$$

In the steady state $\dot{p}_x$=$\dot{p}_y$=0 and we obtain:

$$\vec{\varepsilon} = -\vec{v} \times \vec{B} + \frac{m}{e\tau}\vec{v} \tag{2.9}$$

If we then convert velocity to current density using equation 2.6, in 2D we get:

$$\begin{bmatrix} \varepsilon_x \\ \\ \varepsilon_y \end{bmatrix} = \frac{1}{\sigma_0} \begin{bmatrix} 1 & \omega_c\tau \\ \\ -\omega_c\tau & 1 \end{bmatrix} \begin{bmatrix} j_x \\ \\ j_y \end{bmatrix} \tag{2.10}$$

Where σ_0 is given by equation 2.7 and $\omega_c = \frac{eB}{m}\tau$. We can define the resistivity tensor:

$$\vec{\varepsilon} = \overleftrightarrow{\rho}\vec{j} \tag{2.11}$$

$$\overleftrightarrow{\rho} = \begin{bmatrix} \rho_{xx} & \rho_{xy} \\ \\ -\rho_{xy} & \rho_{yy} \end{bmatrix} \tag{2.12}$$

From Eqn. 2.12 we can see that the longitudinal resistivity, ρ_{xx}, is the same as derived earlier in the 1D case, however we also have a new term, the transverse resistivity ρ_{xy} given by:

$$\rho_{xy} = \frac{\omega_c\tau}{\sigma_0} \tag{2.13}$$

$$= \frac{\frac{eB}{m}\tau}{\frac{ne^2\tau}{m}}$$

$$= \frac{B}{ne} \tag{2.14}$$

Finally, we can define the Hall coefficient, R_H:

$$R_H = \frac{\rho_{xy}}{B} = \frac{1}{ne} \tag{2.15}$$

By measuring the transverse resistivity as a function of field the sign of the charge carriers as well as the carrier concentration can be determined.

There is, however, at least one important assumption used here, namely that the material has one conducting band and thus one species of carrier. With both electron- and hole-like bands the Hall coefficient becomes (from [90]:

$$eR_H = \frac{1}{\sigma^2}\left(\frac{\sigma_h^2}{n_h} - \frac{\sigma_e^2}{n_e}\right) \tag{2.16}$$

In a system with equal hole and electron bands the metal is called "compensated" and the Hall coefficient is reduced. For this reason measurements of the Hall coefficient are mainly useful in determining the carrier concentration in one band systems. In chapter 6 I use this meaurement of carrier concentration for iron-based superconductors, however although these systems have as many as five conducting bands I show that it acts as though there is only one band and that the electron-like band dominates the transport properties.

As we saw earlier in this chapter, the Hall coefficient can be obtained from measurements of the transverse resistivity as a function of magnetic field. It is measured in much the same way as the longitudinal resistivity but with a different configuration of leads. So far only the ideal case, with two parallel voltage contacts, has been considered [see Fig. 2.5(c)], however it is very easy to have a small mis-

alignment of the voltage leads that would cause a longitudinal component to appear in the measurement. For thicker samples or large misalignments this longitudinal term can be on the order of or greater than the transverse voltage that you are actually trying to measure. For this reason we antisymmetrize the data before analyzing it.

The longitudinal component of the magnetoresistance of a material should always be an even function of field, *i.e.*, $R_L(H) = R_L(-H)$, since any deflection of the charge carriers should go unnoticed by the longitudinal voltage lead configuration. The transverse component, however, should be odd in field, *i.e.*, $R_T(H) = -R_T(-H)$. The total magnetoresistance is of the form: $R(H) = R_L(H) + R_T(H)$, where the subscripts "L" and "T" denote longitudinal and transverse resistances, respectively (called R_{xx} and R_{xy} in previous sections but generalized here as R_L and R_T). By measuring the magnetoresistance in positive and negative field, then subtracting them we can separate out the transverse component, *i.e.*:

$$
\begin{aligned}
{}^1/_2\,(R(H) - R(-H)) &= {}^1/_2(R_L(H) + R_T(H)) - {}^1/_2(R_L(H) - R_T(H)) && (2.17)\\
&= R_T(H) && (2.18)
\end{aligned}
$$

This is known as antisymmetrization. Similarly, we can symmetrize the data by adding the positive and negative field sweep data to obtain the longitudinal (even) part of the signal.

When taking a measurement of the Hall coefficient we measure the magnetiresistance at a constant temperature and typically sweep the field from -5 T to +5 T,

measuring every 0.5 T. We then antisymmetrize the data, subtracting the negative field values from the positive values. I then fit this curve to a line and find the slope, which is proportional to the Hall coefficient R_H.

2.4.4 Scattering Rate

In the Drude model, electrons experience collisions with a characteristic time, τ, usually referred to as the relaxation time or mean free time [71, 77]. This relaxation time shows up in many of the equations that describe electronic transport as we have already seen in this chapter (see Eqn. 2.7). Often in discussions of the Drude model, the relaxation time is discussed first since it is fundamental to the theory. Here I have placed this discussion after a discussion of transverse and longitudinal resistivity for reasons that will become obvious.

At low temperatures, the transport scattering rate, $\Gamma=\tau^{-1}$, is a measure of impurity scattering in a metal and can be determined from the resistivity and Hall coefficient. Rearranging Eqn. 2.7 we see:

$$\Gamma = \frac{ne^2\rho}{m^*} \tag{2.19}$$

Substituting into Eqn. 2.15 gives:

$$\Gamma = \frac{e\rho}{m^* R_H} \tag{2.20}$$

From measurements of Γ at zero temperature we can obtain information about the level of impurity scattering in a system, similar to the informations one finds from

the residual resistivity ratio. However, when comparing these impurity measurements between two systems, the scattering rate is the more fundamental quantity as it does not depend on the carrier concentration. On the other hand, comparing the zero temperature scattering rate for several different samples of copper will give the same information as the residual resistivity, so a measurement of the carrier concentration is unnecessary.

In Chapter 6, I use the scattering rate to find information about the pairing symmetry in iron-based superconductors. It was shown by Abrikosov and Gor'kov that impurity scattering has the effect of averaging the gap function over the fermi surface [91]. One implication of this is that systems with gap functions that change sign will be strongly affected by impurity scattering. Since the scattering rate is a measure of impurity scattering, I was able to use it to show that pair breaking effects are what cause the range of transition temperatures seen in 122 materials.

2.5 Magnetic Susceptibility

Ideally, superconductors expel all magnetic field, a property known as the Meissner effect. Of course real superconductors typically do not show an ideal magnetization because of vortex pinning and impurities. Because of this expulsion of field, a superconductor can be called a perfect diamagnet in that it creates an internal field exactly opposite to the applied field. The MPMS reports results for the magnetization in emu. If we divide this result by the applied field and the mass of the sample I obtain the susceptibility per gram. If I then multiply by the density and

a factor of 4π I can obtain the volume magnetic susceptivility, χ_v. In these units, below T_c a bulk superconductor should have a volume magnetic susceptibility of -1. By measuring the magnetic susceptibility as a function of temperature I can then determine the transition temperature as well as the superconducting volume fraction of a sample.

In the MPMS, magnetization measurements are performed by first cooling the sample to the base temperature (1.8 K) in zero magnetic field, then applying a small magnetic field, typically 1 - 100 mT. Thye magnetic susceptibility is then measured while increasing the temperature of the sample above T_c (giving us the zero-field-cooled (ZFC) curve). Next, the susceptibility is measured while the sample is cooled back down below T_c without removing the magnetic field. This second result is called the field-cooled (FC) curve. In an idealized sample with no defects or vortex pinning, it shouldn't matter whether a sample is cooled down in a magnetic field or cooled down in zero field; in both cases the sample should show perfect diamagnetism. In real samples, however, there is a difference between the two curves (see Fig. 2.11). If a type II superconductor is cooled down in a magnetic field some of the magnetic flux will be trapped (pinned) inside the sample, thus reducing the diamagnetic response. The ZFC curve is a more accurate representation of the superconducting volume fraction because it has less flux trapped inside the sample than the FC curve. In this thesis I present magnetic susceptibility data and will only show the ZFC curves. In iron-based superconductors, the FC curve shows some diamagnetic response, but never the full response of the ZFC curve.

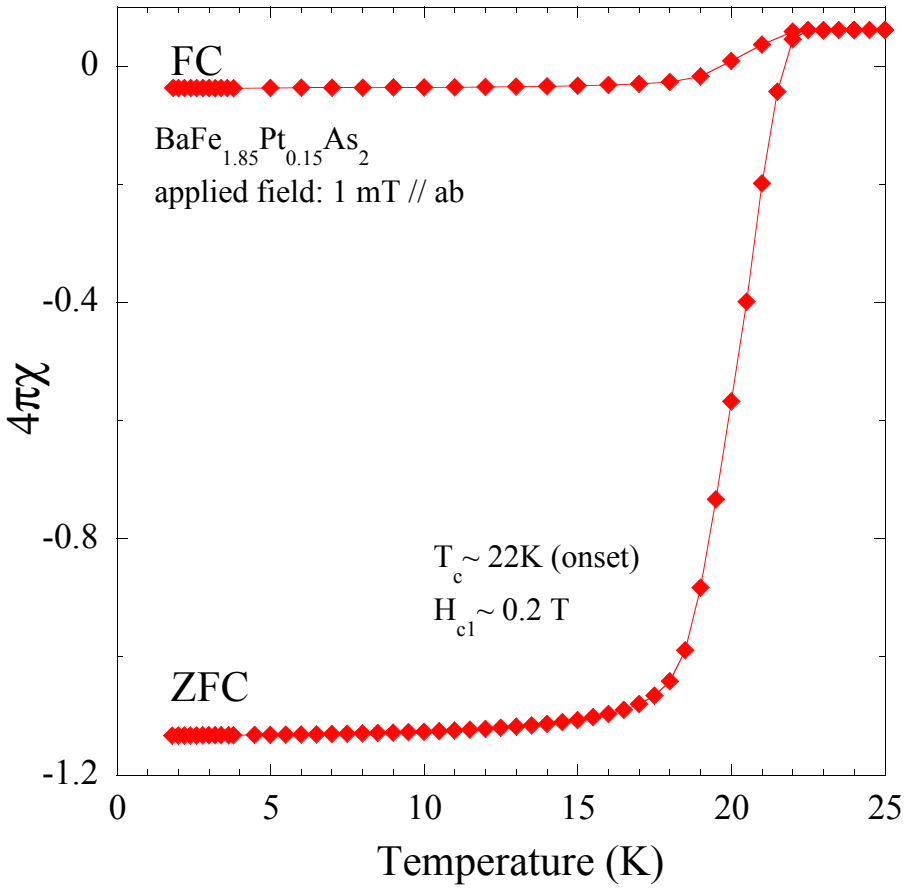

Figure 2.11: Field cooled (FC) and zero-field cooled (ZFC) magnetic susceptibility curves for $BeFe_{1.85}Pt_{0.15}As_2$. The ZFC curve is unaffected by pinning and is the correct measure of superconducting volume fraction. The apparent 115% volume fraction is due to error in the calculation of the demagnetization factor.

2.6 Pairing Symmetry and Scattering Rate

Superconductivity occurs because of the pairing of electrons; disrupting this pairing in any way should affect the properties of a superconductor. In the first superconductors that were discovered (elements and binary compounds) the "glue" that held the electrons together (called the pairing mechanism) is phonons. At low temperatures, phonons are able to produce an attractive interaction between two electrons which binds them together into a Cooper pair. Although phonons are the pairing mechanism for elemental superconductors, in general the pairing mechanism need not be lattice vibrations; in principle any interaction that can produce an attractive potential could cause electrons to pair. Although a more in-depth discussion of potential pairing mechanisms would be out of place in this thesis, it should be noted that different mechanisms can produce a superconducting gap with differing momentum dependence and pairing symmetry. For iron-based superconductors, three likely models for pairing symmetry are shown in Figure 1.6.

Anderson's theorem states that in an s-wave superconductor a small increase in scattering due to non-magnetic impurities should have no effect on T_c [33, 92]. If, however, the scatterering somehow breaks the pairs (either through averaging over the Fermi surface or spin-flip scattering) then the transition temperature will decrease according to the Abrokosov-Gor'kov function [93] (see Eqn. 2.21 and Fig. 2.12). The idea is that scatterind that causes pairs to break would decrease the transition temperature. The effect of nonmagnetic impurity scattering is to average the gap over the Fermi surface [33], so in an s-wave superconductor where the gap

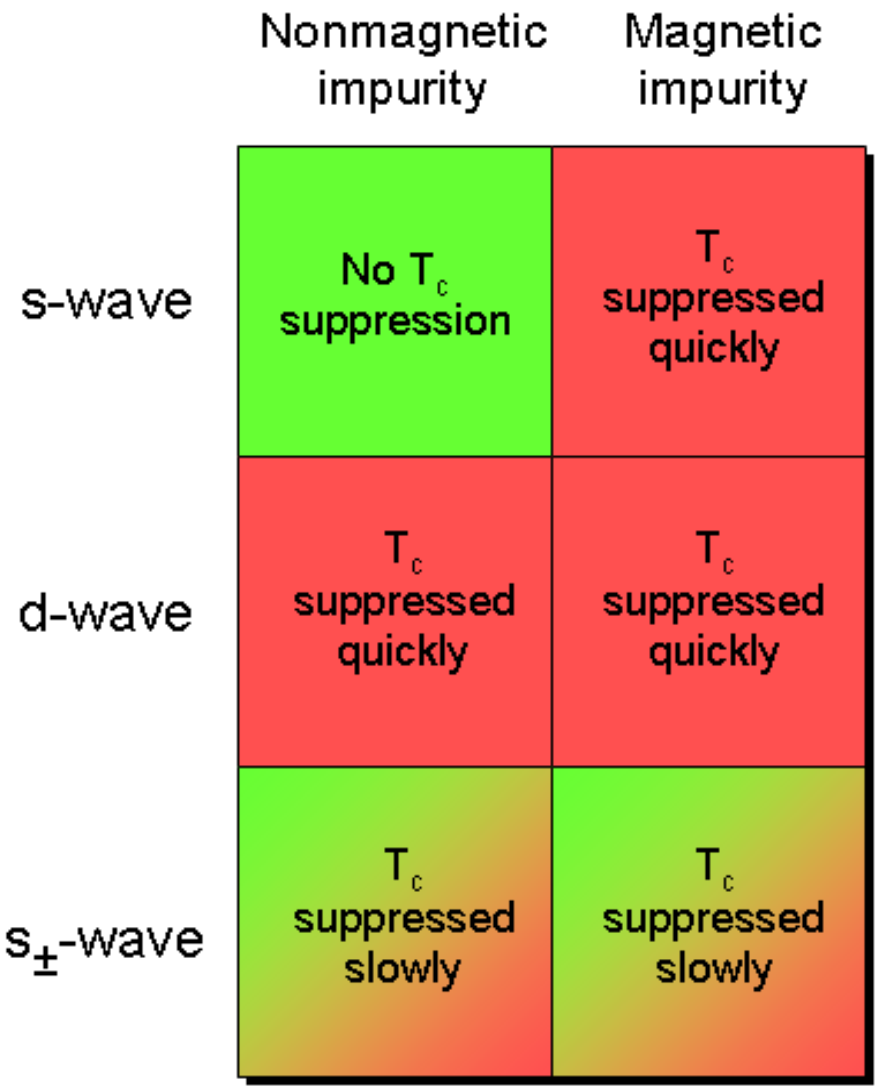

Figure 2.12: Rate of suppression of superconducting transition temperature, T_c for different order parameters and types of scattering.

does not change sign nonmagnetic impurities should have no affect on the transition temperature. In a d-wave superconductor, however, the average of the gap over the fermi surface is zero ($\langle\Delta\rangle_{FS} = 0$), so the effect of nonmagnetic impurities is to decrease the gap and the transition temperature.

Another way to break pairs is by flipping the spin of one of the electrons, as in the case of magnetic impurity scattering. In both s- and d-wave [94] order parameters, magnetic impurities would create pair-breaking scattering because an electron in a singlet pair scattering off of a magnetic impurity would flip its spin and thus no longer pair [91]. Pair breaking was studied theoretically by Abrikosov and Gor'kov [91]. For magnetic scattering in a conventional s-wave superconductor they found that the suppression of T_c with scattering obeys [26, 95, 96, 91]:

$$ln\left(\frac{T_c}{T_{c0}}\right) = \psi\left(\frac{1}{2}\right) - \psi\left(\frac{1}{2} + \frac{\alpha}{2t}\right), \tag{2.21}$$

Where $t = T_c/T_{c0}$ and α is the pair-breaking parameter given by:

$$\alpha = \hbar \cdot \Gamma/(2\pi k_B T_{c0}) \tag{2.22}$$

Thus the rate of suppression of T_c in an s-wave superconductor with magnetic impurities is well known theoretically. Fig. 2.13 shows a plot of Eqn. 2.21.

With sign-changing order parameters the rate of suppression can vary drastically. In the case of a d-wave superconductor or a "perfect" $s_\pm$ superconductor, where the average of the gap over the Fermi surface is zero ($\langle\Delta\rangle_{FS} = 0$) both magnetic and nonmagnetic impurities should suppress T_c at a rate similar to that of

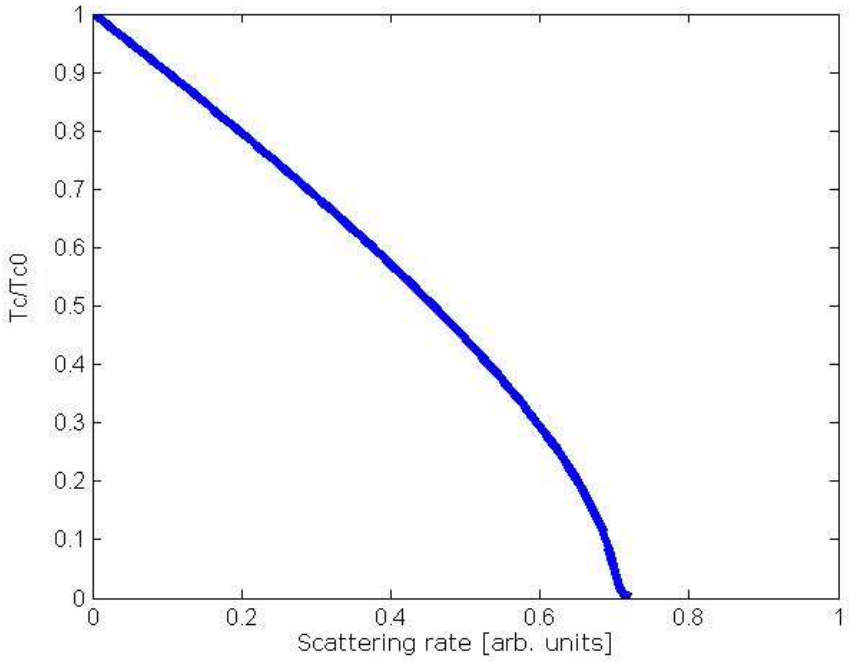

Figure 2.13: Plot of pairbreaking prediction by Abrokosov and Gor'kov [91]. Transition temperature decreases as magnetic scattering increases in an s-wave superconductor.

magnetic impurities in an s-wave superconductor [97] (see Fig. 2.12). Recently, calculations by V. G. Kogan [28, 98] on anisotropic superconductors ($\langle\Delta\rangle_{FS} \ll \Delta_{max}$) and by Efremov *et al.* [99] and Wang *et al.* [100, 37] on multiband superconductors have shown that this rate of suppression can change drastically depending on the relative strength of inter- and intraband coupling. In chapter 6 I use the scattering rate to determine the pairing symmetry of the 122s and speculate on the relative strength of inter- and intraband scattering.

Chapter 3

Superconductivity in the Undoped Parent Compound $SrFe_2As_2$

Portions of this chapter have been summarized or paraphrased from my published work, Refs. [1] and [2].

It has long been established that superconductivity in cuprate and heavy-fermion superconductors can be obtained by tuning the system via doping or pressure [34, 78]. Likewise, it has been found that superconductivity is stabilized in the iron pnictide materials by either electron- or hole-doping of the system, or by applying an external pressure [38, 36, 101]. In most pnictide superconductors, the undoped and unpressurized materials (also known as "parent" compounds) typically do not exhibit superconductivity, but rather undergo an antiferromagnetic ordering much like that seen in the cuprates and heavy fermion systems. The magnetically ordered phase can be suppressed through doping or pressure, and this suppression is often accompanied by the presence of superconductivity over a limited range of parameter space.

There are, however, exceptions to this typical behavior and superconductivity can sometimes be found in parent compounds. In the cuprates, superconductiv-

ity has been observed in materials in the T' phase with the chemical composition RE_2CuO_4, even though they are predicted to be a Mott insulator [102]. In the 122s there have been reports of partial superconducting transitions in $BaFe_2As_2$ [103, 104] and $CaFe_2As_2$ [105] with superconductivity attributed to strain. There have also been studies showing that, rather than strain, water intercalation in $SrFe_2As_2$ can induce superconductivity [106].

In this chapter I discuss my observation superconductivity in undoped, unpressurized $SrFe_2As_2$. Unlike previous studies, I found that the superconducting transition showed a full drop in resistance and a small but significant diamagnetic signal. This unexpected superconducting phase typically occupied less than 15% of sample volume, but it occurred in 90% of as grown samples and was robust with respect to applied magnetic fields. In this material, the superconducting phase occurs deep below the tetragonal-to-orthorhombic structural phase transition and coexists with antiferromagnetic order. Through systematic heat and pressure treatments and magnetization measurements, I find evidence of a controllable, reversible superconducting phase. I also found a small ferromagnetic moment that appears to be proportional to the superconducting volume fraction estimated from diamagnetic screening. I report an investigation into how the superconducting phase can be removed by heat treatment and how it can be reestablished by applied mechanical stress. Finally, using single-crystal x-ray crystallography, I uncovered a surprising relationship between the appearance of these phenomena and the level of lattice distortion associated with preferentially oriented planar defects, suggesting an intimate relationship between superconductivity, magnetism, and crystallographic strain in

this system of materials.

3.1 Experimental Details

$SrFe_2As_2$ single crystals were grown using the self-flux method described by Wang *et al.* [107] and in section 2.1.1. This process has enabled the growth of large crystals with typical dimensions $5 \times 5 \times 0.25$ mm^3, essentially limited by crucible size. Note that the flux is not decanted in this process, instead requiring simple mechanical separation of single crystals from the hardened flux matrix. This fact is important as it may cause residual strain in the crystals, the repercussions of which will be discussed later.

Structural properties were characterized by both powder and single-crystal x-ray diffraction measured at 250 K with Mo K-α radiation using Rietfeld (TOPAS-4) and single crystal (SHELXS-97) refinement. The lattice was determined to have the previously reported [108] I4/mmm structure with lattice constants a= 3.9298(3) Å and c = 12.320(2) Å. Reciprocal lattice precession images were generated from Bruker APEX2 software. EDS analysis determined that the crystals have the desired 1:2:2 stoichiometry with no impurity phases detected and gave no indication of of difference between superconducting and non-superconducting samples. Resistivity and magnetic susceptibility were measured in commercial MPMS and PPMS systems by Quantum Design.

3.2 Observation of Superconductivity

Figure 3.1 presents a comparison of the resistivity ρ(T) of several as-grown samples of $SrFe_2As_2$ normalized to the room temperature value to remove geometric factors. As shown, the samples exhibited virtually identical metallic behavior with a sharp kink at $T_0 = 198$ K. This kink has been associated with a structural phase transition (from tetragonal to orthorhombic upon cooling) that is coincident with the onset of antiferromagnetic (AFM) order [109]. At lower temperatures, a sharp drop in ρ(T) beginning at 23 K is consistently found in approximately 90% of as-grown samples synthesized under varying heating schedules. While a minority of non-superconducting samples do not show any trace of a resistive transition down to 18 mK, the majority of my samples consistently show a transition at the same temperature, with a midpoint at $T_c \sim 21$ K. These samples also show a large, anisotropic upper critical field (Hc_2) as shown in Fig. 3.2 and the top inset in Fig. 3.1.

The existence of superconductivity in the undoped "parent" compound is surprising, given that charge doping or applied pressure is typically necessary to invoke similar transition temperatures throughout this family of materials [15, 110, 5, 111, 112, 113, 111], and its intermittent appearance in different samples suggests that it is an unstable or parasitic phase. This system may be similar to the appearance of filamentary superconductivity at 1 K which is far above the bulk transition of 0.4 K in the heavy-fermion superconductor $CeIrIn_5$ [114]. However, etching and sanding the surfaces of my samples yielded no difference in ρ(T). Similarly, six-wire

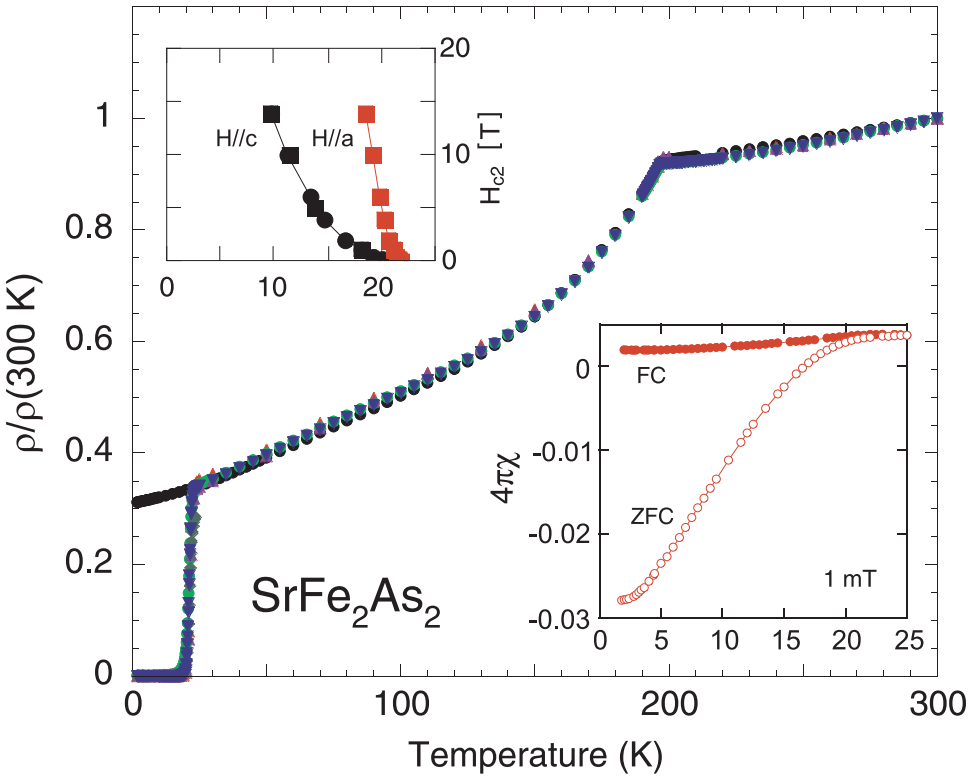

Figure 3.1: Comparison of resistivity of several as-grown specimens of $SrFe_2As_2$ normalized to 300 K, showing a complete superconducting transition in four of five samples. The data presented here is for samples R1, R3, R4, R5, and R7, with R1 being the only sample not showing superconductivity at 20 K. Top inset: H_{c2}(T) deduced from extrapolated resistive onset of T_c in two samples for two field orientations. Bottom inset: magnetic susceptibility of superconducting sample b1A measured with H = 1 mT//c (from Ref. [1]).

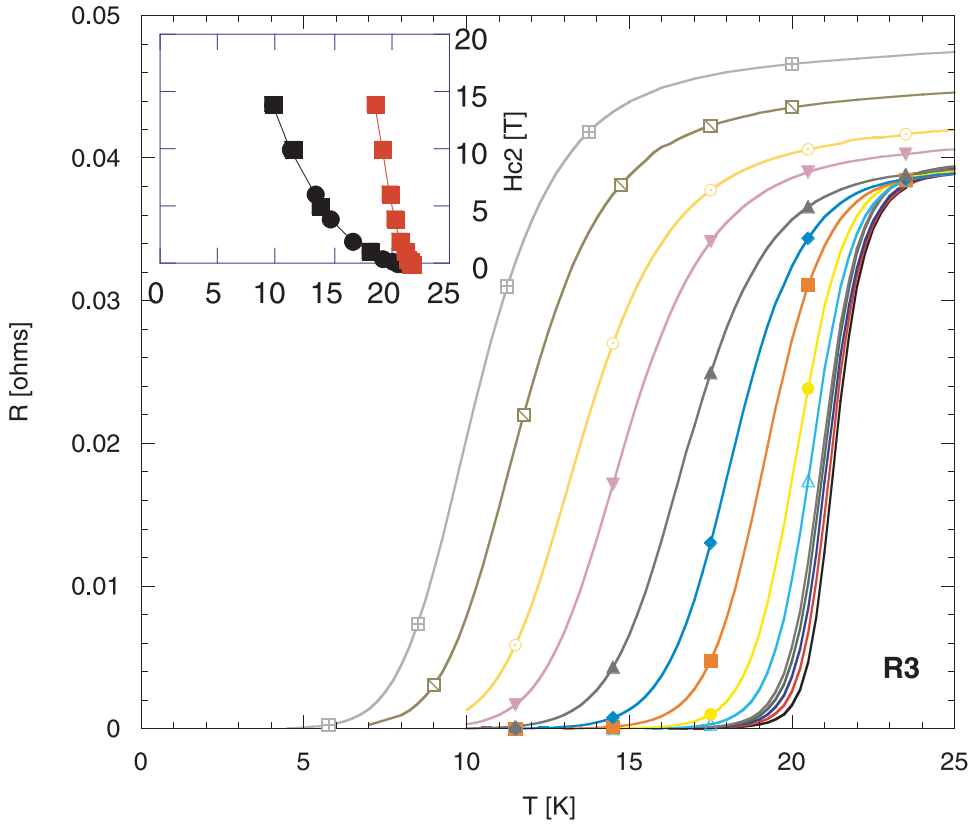

Figure 3.2: Resistivity vs. temperature for $SrFe_2As_2$ at fields from 0 to 14 T. Inset: H_{c2} curves of superconducting $SrFe_2As_2$ single crystals taken from the midpoint of the resistive transition. The upper critical field is anisotropic with fields parallel to the ab plane giving a higher upper critical field. Data is presented for sample R3.

resistivity measurements (with pairs of voltage leads on both the top and bottom of the crystal so as to measure voltage drops due to currents forced to travel through the thickness of the sample) suggest that the superconductivity is not confined to the sample surfaces.

Fig. 3.3 and the bottom inset in Fig. 3.1 show the onset of a small but distinct diamagnetic response in magnetic susceptibility. This response is consistent with the onset of partial volume fraction superconductivity below 21 K. Although the volume fraction is typically less than 10%, I have observed this fraction to reach as high as 15%, suggesting that a non-negligible volume of bulk superconductivity can be stabilized in $SrFe_2As_2$.

3.3 Annealing and Cold-Working Studies

The partial-volume superconducting phase in $SrFe_2As_2$ has proven to be particularly sensitive to mild heat treatment. In Figure 3.4 I show resistivity as a function of temperature for a single sample of $SrFe_2As_2$ taken both before and after an annealing treatment (data is for the same sample but with different electrical contacts made after heat treatment). As discussed above, there is a complete resistive transition observed for the as-grown crystal, suggesting a sufficient volume of the sample is superconducting to provide a complete shorted path between sample contacts, thus shorting out the voltage measurement. After heating the sample for only 10 minutes at 300 °C in a sealed argon environment devoid of oxygen, the superconducting transition is found to be completely suppressed. In other experi-

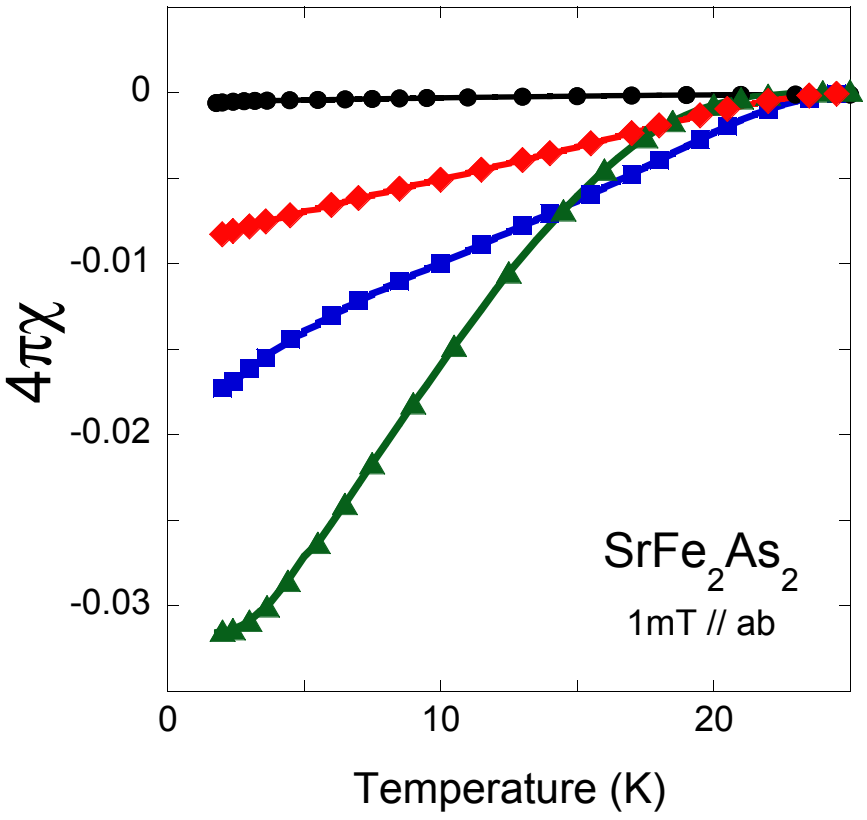

Figure 3.3: Diamagnetic screening in four $SrFe_2As_2$ single crystals as measured by magnetic susceptibility, showing the estimated superconducting volume fraction to range from zero to slightly more than three percent of the total volume of the samples. The volume fraction ranges up to 15% in as-grown crystals (from Ref. [2]).

ments (not shown), I determined that it takes as little as 200 °C to suppress this transition, with some samples still showing a partial drop or kink at the same T_c value after low temperature heating. Also, annealing in either air or sealed under an argon atmosphere has the same effect in suppressing the superconducting transition.

It may be thought that some type of impurity or oxidation phase that is changed after heat treatment may give rise to the change in superconducting properties in such samples. However, both EDS and WDS analysis performed on samples both before and after my annealing procedure, showed no changes to the chemical composition. This is unlike the scenario found in annealed cuprate superconductors, which show a drastic change in the superconducting properties associated with a reduction in oxygen present in the crystals [115, 116]; in contrast, there is no indication that oxygen plays any role in the phenomena reported here.

Surprisingly, this suppression effect can be reversed and superconductivity can be reintroduced to a sample that has been annealed. Because annealing is an effect that usually reduces strain, several other experiments were performed that involve introducing strain into the samples. Fig. 3.5 shows the results of one such experiment. A single crystal of superconducting $SrFe_2As_2$ (curve 1) was annealed to remove the superconductivity (curve 2). Upon application of external pressure using a standard piston cell, the superconducting transition that was suppressed with heat treatment appears to return as evidenced by a stronger partial transition in resistivity (curve 3). Finally, when the applied pressure is released a full superconducting transition is recovered (curve 4).

To investigate the role of mechanical stress in inducing superconductivity sev-

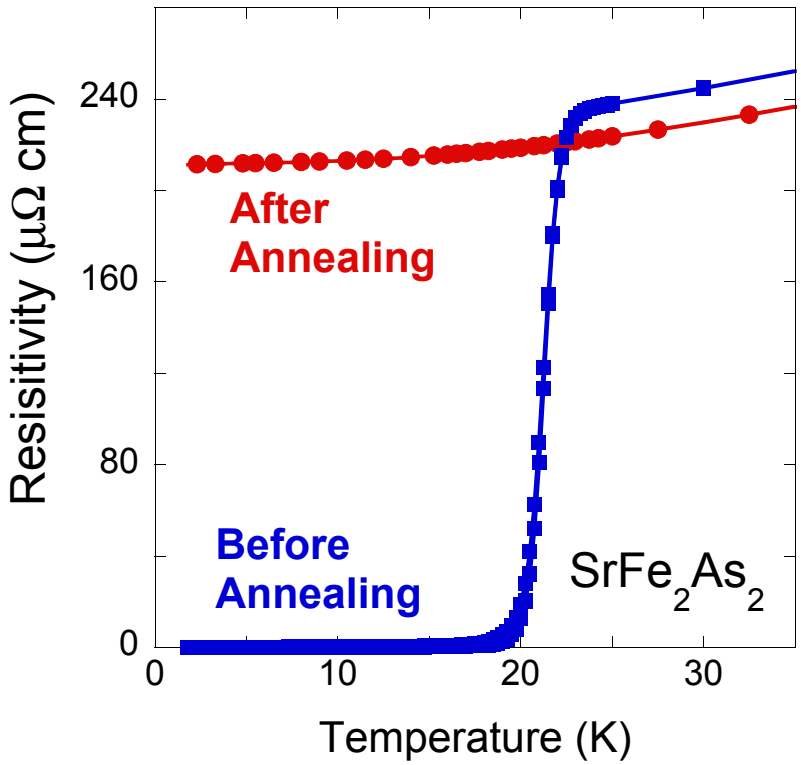

Figure 3.4: Resistivity of a single-crystal sample of $SrFe_2As_2$, measured before (blue squares) and after (red circles) a 10 minute annealing treatment at 300 °C in argon atmosphere. Data is not normalized (from Ref. [2]).

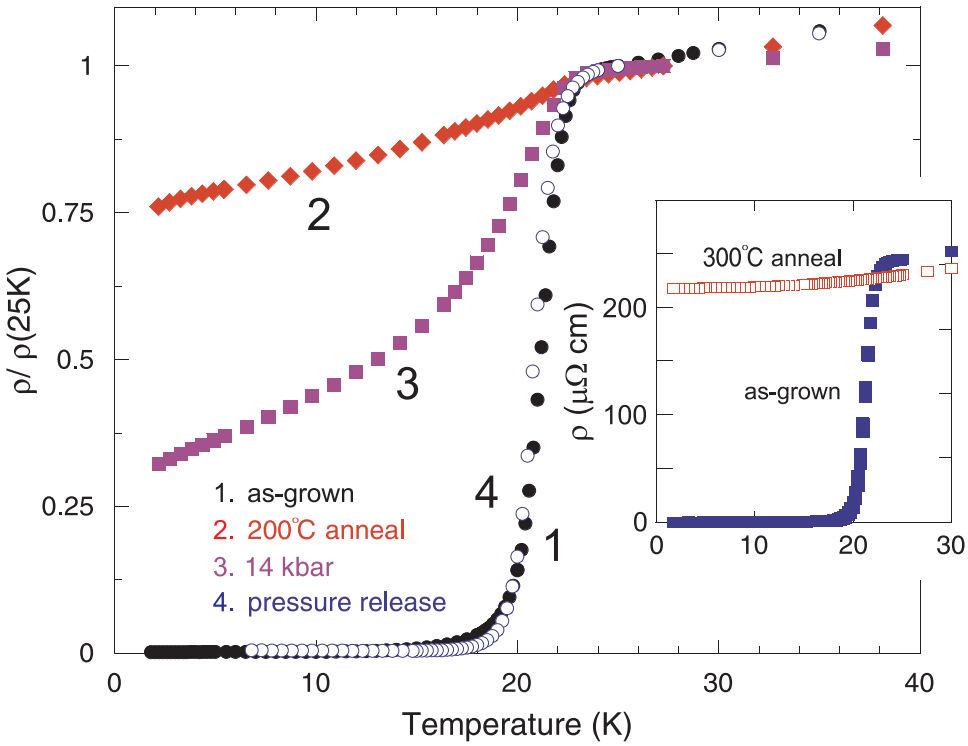

Figure 3.5: Heat treatment and applied pressure effects on resistive superconducting transition in one sample of $SrFe_2As_2$, following the sequence: 1) unannealed, as-grown sample, 2) 200°C heat treatment, 3) 14 kbar applied pressure, and 4) ambient conditions after release of pressure. Inset: a different superconducting sample subjected to 300°C heat treatment (from Ref. [1]). Data is presented for sample b1 R5.

eral other physical tests were performed, including cleaving, quenching with liquid nitrogen, and subjecting a sample to severe mechanical deformation. A large as-grown single-crystal sample was first annealed to remove any trace of superconductivity and then subject to several tests. Figure 3.6 presents the resistivity measurements taken after annealing the sample and after each stress treatment to check for any trace of induced superconductivity. First, the sample was plunged into liquid nitrogen to test the ability of rapid thermal cycling to induce superconductivity. Resistivity measurements found that the superconducting transition did not return. Next the sample was cleaved in order to investigate whether my standard procedure for preparing resistivity samples was in fact responsible for inducing superconductivity. The sample was carefully cleaved into two pieces using a steel razor blade, after which the resistivity of each half was measured. Again, there was no return of a superconducting transition, as shown in Fig. 3.6. Finally, a remaining 1 mm^2 piece of the sample was placed in a piston-type press and squashed until its surface area had doubled, requiring an applied force of 4,000 lbs on a 1 cm diameter piston.

In contrast to the previous two tests, this severe deformation was found to induce a return of the 21 K superconducting transition. Figure 3.6 presents the resistivity of the squashed sample in comparison to its resistivity just after annealing and after cleaving. The major difference between the three curves is in the appearance of the drop in resistivity at $T_c \sim 21$ K in the deformed sample. (The resistivity data were shifted and normalized to the values of the severely deformed sample at 25 and 300 K to remove a substantial increase in the residual resistivity and change in the geometric factor of the deformed sample arising from defects,

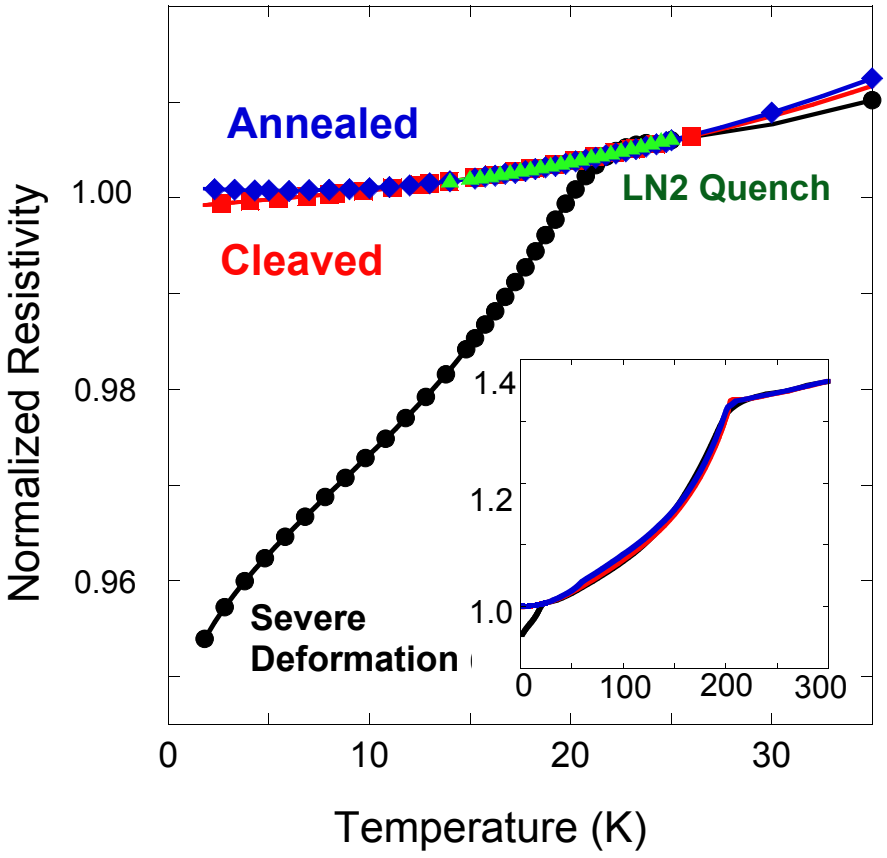

Figure 3.6: Electrical resistivity measurements of a single-crystal sample of $SrFe_2As_2$ subject to various treatments. The sample was first annealed at 300 °C to suppress any trace of superconductivity (blue diamonds), then quenched in liquid nitrogen from room temperature (green triangles), then cleaved with a razor blade (red squares), and one remaining piece subsequently pressed to >100% mechanical deformation (black circles). Data is shifted and normalized to the resistivity of the pressed sample at 25 K to remove spurious contributions from micro-cracks, etc. as discussed in the text. The inset shows the resistivity profile over the full temperature range (from Ref. [2]).

cracks, etc. introduced during the deformation process.) Although the measured drop is not a complete transition as in the previous study with applied quasihydrostatic pressure, it is presumed that the actual volume fraction of superconductivity may be larger than this drop implies, due to the possible introduction of fractures and voids in the sample that would interrupt a continuous superconducting pathway. Figure 3.7 presents scanning electron microscope images of the surface of a sample subject to the same deformation treatment, indeed showing the presence of micro-cracks throughout the sample. These cracks are presumably the reason for the absence of a complete superconducting transition to zero resistance, although more studies are required to make such a determination. Unfortunately, this level of mechanical deformation weakens the sample enough that it was difficult to do subsequent characterization measurements; I were unable to perform magnetization measurements to determine the superconducting volume fraction.

3.4 Lattice Distortion

The above experiment established that the superconducting phase can be suppressed with annealing and recovered by applying a stress to the crystal. Together, this data suggests that some form of internal crystallographic strain is the likely origin of the superconducting instability in undoped, unpressurized $SrFe_2As_2$. Defect structures have indeed been observed in other compounds with the $ThCr_2Si_2$ structure, such as URu_2Si_2 [117].

To investigate this, I performed single-crystal x-ray diffraction measurements

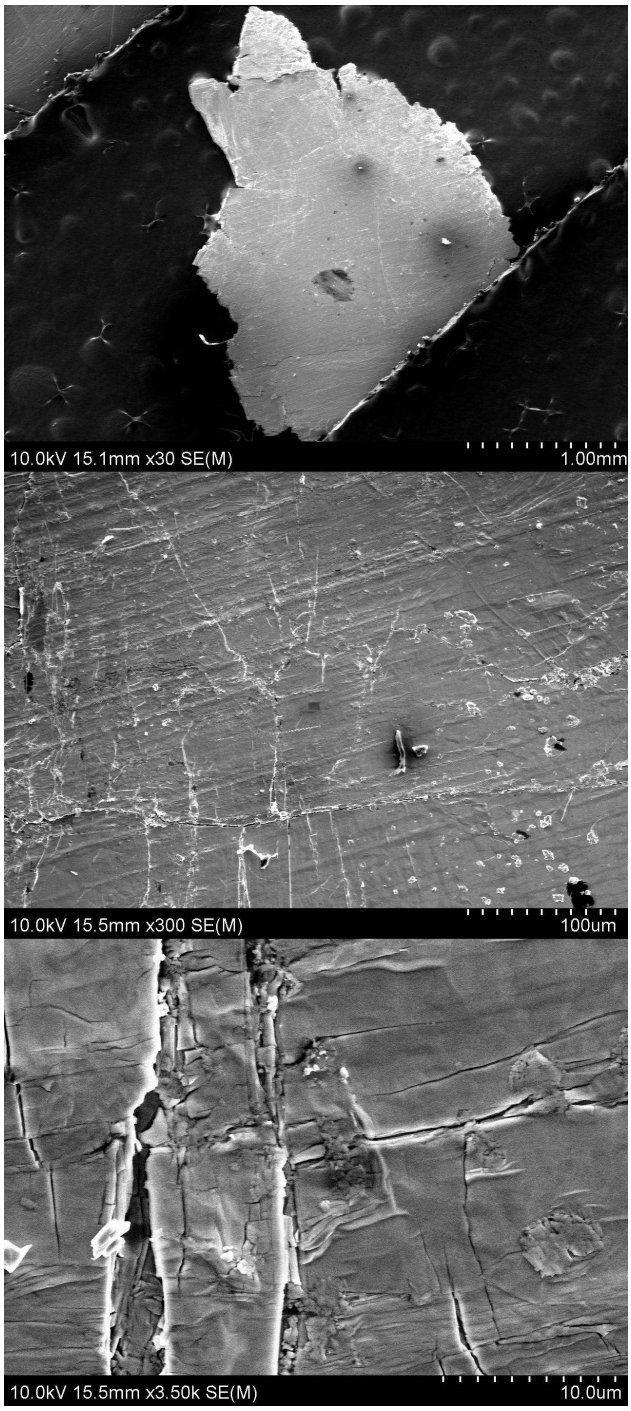

Figure 3.7: Scanning electron microscopy images of a single-crystal sample of $SrFe_2As_2$ subject to severe ($\sim 100\%$) deformation by a piston-type press. Panels a), b) and c) show pictures of the same sample at different magnification levels as indicated (from Ref. [2]).

on three characteristic samples exhibiting 0%, 1%, and 15% superconducting volume fractions. As shown in Fig. 3.8, the reciprocal-lattice data indeed showed evidence for the appearance of crystal lattice distortions with increasing volume fraction, as evidenced by an increasing ringlike smearing of diffraction spots. Interestingly, this smearing is present only in the (h0l) patterns and not in the (hk0) patterns, suggesting a form of planar defect that lies preferentially along the basal plane causing a distribution of orientations tilted about the basal plane axes. This scenario is corroborated by the recent report of enhanced c-axis resistivities in superconducting samples of $SrFe_2As_2$ and $BaFe_2As_2$ crystals [104].

Other studies have shown superconductivity in parent compounds, however they do not attribute this phase to anything structural. For single crystals of $BaFe_2As_2$ grown with In flux, a superconductind transition was observed in resistivity measurements. However low critical currents and a lack of diamagnetic signal led the authors to conclude that the superconductivity might be filamentary [103]. They did not observe suppression of superconductivity with annealing as I do here, and so reject the idea of strain-induced superconductivity. Instead, they observe an effect with surface treatment that I have not, and thus attribute their results to surface superconductivity. Another study on thin films of $SrFe_2As_2$ found that treating the films for several hours in air or water vapor can induce superconductivity [106]. Again, rather than strain effects, the authors concluded that the superconductivity may come from charge doping or Sr vacancies, although this claim has not been substantiated by measurements of the carrier density.

Studies of pressure-induced superconductivity in the 122 parent compounds

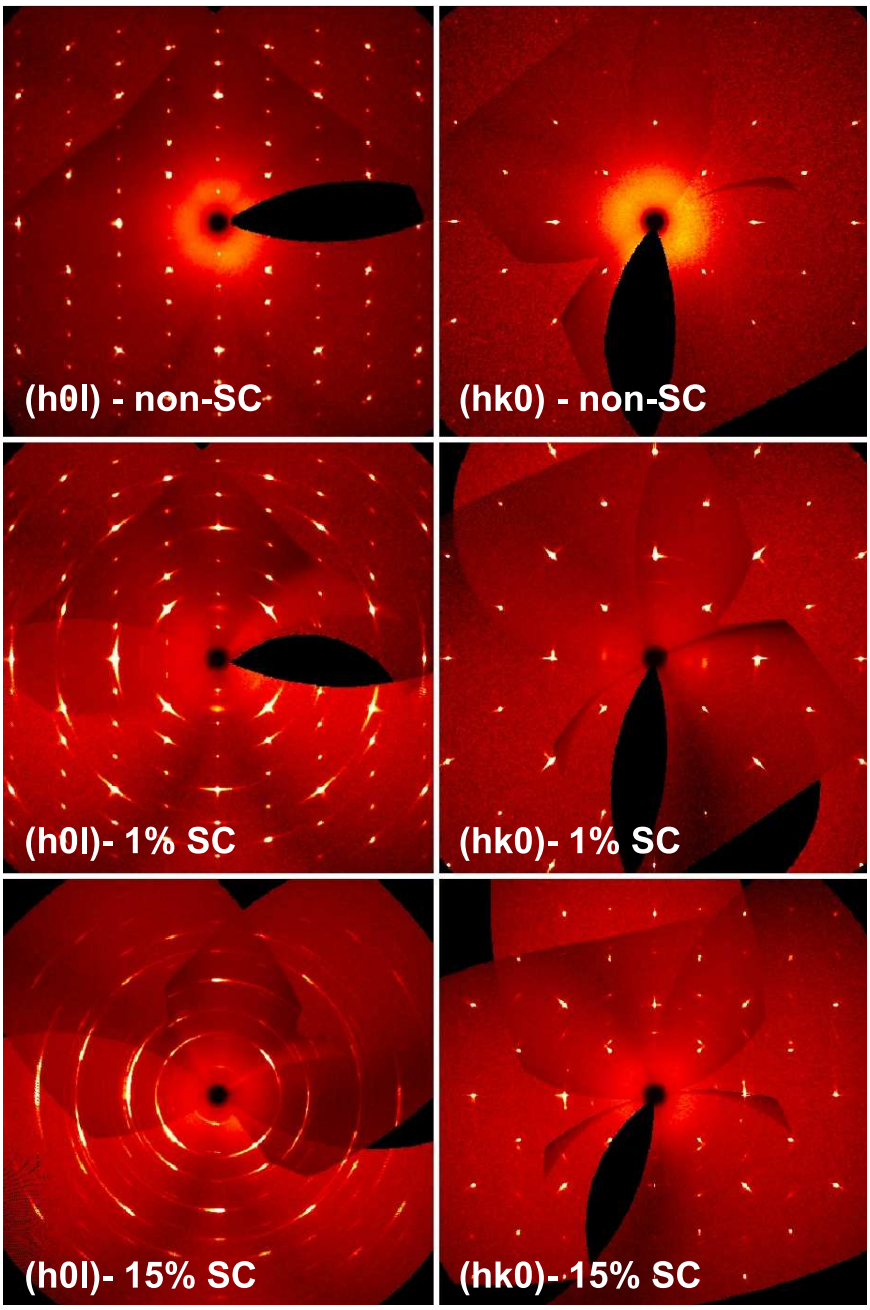

Figure 3.8: Reciprocal-lattice structure of $SrFe_2As_2$ from single-crystal x-ray diffraction measurements at 250 K for three characteristic samples with varying measured superconducting volume fractions as noted. Note that significant changes occur in the (h0l) reflection zone, but none are observable in the (hk0) c-axis projection (from Ref. [1]).

have indicated a quite narrow region of full-volume fraction superconductivity [112], most evident in the case of $CaFe_2As_2$ where hydrostatic (He gas) pressure conditions have revealed the absence of superconductivity over any sizable range of pressure [41], in contrast to that originally reported [113, 111]. Given the likelihood of strain induced superconductivity in $SrFe_2As_2$, I suspect that a similar mechanism may be at play in all of these materials, especially in the case of $SrFe_2As_2$, where $T_c \sim 21$ K is also reported in the pressure range of peak volume fraction [112].

3.5 Enhanced Magnetic Susceptibility

A systematic study of the magnetic susceptibility of numerous samples provides striking evidence that stacking faults also have dramatic consequences for the magnetic properties of $SrFe_2As_2$. Figure 3.9 presents a representative data set taken using one large single crystal of $SrFe_2As_2$ before (circles) and after (squares) a 300 °C 2-hour annealing treatment, measured in low (a) and high (b) magnetic fields.

Here I emphasize two striking features present in the as-grown, unannealed sample: a dramatic enhancement of χ(T) and a large concomitant irreversibility in low-field χ(T) that persists up to ∼250 K. After heat treatment of the same sample, these features are both strongly suppressed, yielding a high-field χ(T) curve (Fig. 3.9(b), postanneal data) consistent with previously published results [109] and a low-field curve (Fig. 3.9(a), postanneal data) with strongly reduced magnitude of irreversibility. This dramatic change in χ(T) is unlikely to be caused by impurities, whose concentration and magnetic behavior are surely unaffected by such modest

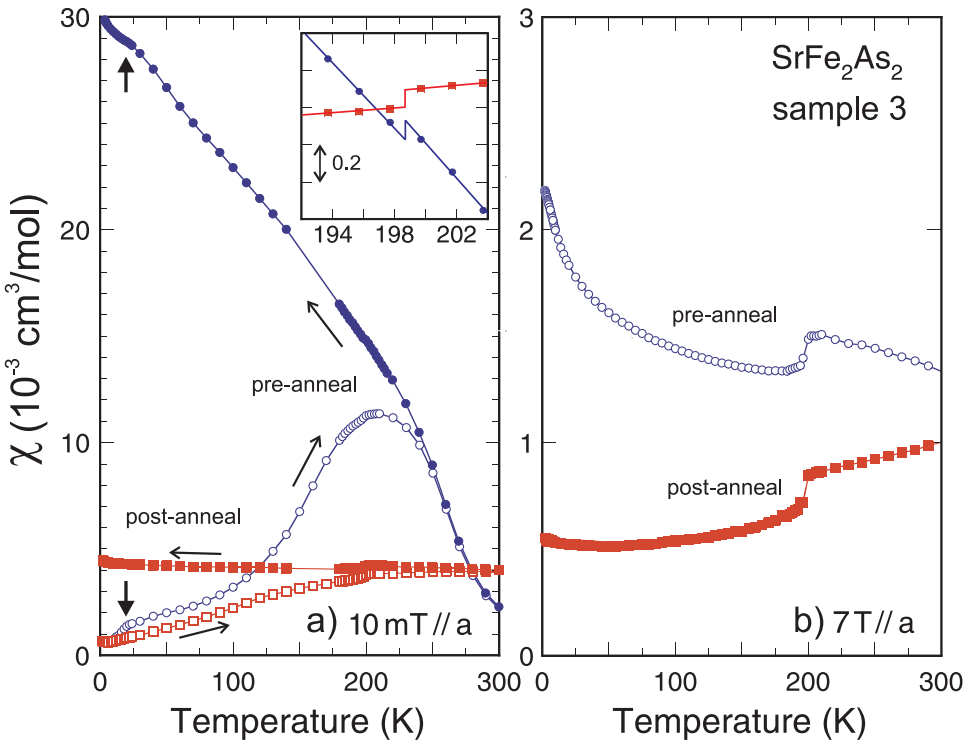

Figure 3.9: Magnetic susceptibility of one single crystal specimen of $SrFe_2As_2$ in (a) 10 mT and (b) 7 T fields applied parallel to the basal plane measured before (blue circles) and after (red squares) 300 °C annealing [open and closed symbols denote zero-field-cooled (ZFC) and field-cooled (FC) conditions, respectively]. The superconducting transition is shown by the arrows. Note the difference in scales of the left and right panels. The inset shows a zoom of χ(T) at a structural or magnetic transition before and after annealing (offset for clarity) (from Ref. [1]).

annealing temperatures. Moreover, as discussed previously, the heat treatment also wiped out any trace of superconductivity, suggesting that the magnetic properties are also tied to the presence of lattice distortion.

Intriguingly, the magnetic enhancement of χ(T) in superconducting samples is ferromagnetic in nature: as shown in the inset in Fig. 3.10, magnetization M isotherms for several samples at 1.8 K clearly indicate the hysteretic behavior of M(H) that saturate to a linear field dependence near 3 T. Because the high-field

slope of the superconducting samples matches the slope of the nonsuperconducting sample, it is clear that the bulk magnetic response of $SrFe_2As_2$ is maintained in all samples. This is also evident from the fact that the magnetostructural transition at $T_0 \sim 200$ K appears to be impervious to either magnetic history, field strength, or heat treatments. This can be seen fron the inset in Fig. 3.9(a), where the abrupt step in χ(T) is unchanges in magnitude ($\sim 2\times10^4$ cm^3/mol) after annealing.

In stark contrast, the apparent ordered moment M_0 extracted from fits to M(H) strongly varies with sample. In fact, as shown in the main panel in Fig. 3.10, M_0 scales with the superconducting volume fraction, providing direct evidence that the cause of the enhanced susceptibility and irreversibility in χ(T) is not only related to the existence of lattice distortions but is altered in direct proportion to the volume fraction of these distortions. Interestingly, if this linear correlation is extrapolated to 100% superconducting volume fraction, the corresponding ordered moment would be $\sim 0.5\mu_B$ (formula unit), comparable to the size of the AFM staggered moment [11]. In $SrFe_2As_2$, where intrinsic disorder could affect the orthorhombic AFM domain structure expected to form below T_0, it is possible that a ferromagnetic moment proportional to the staggered moment arises at these domain boundaries; the presence of planar crystallographic dislocations, as evidenced by my x-ray analysis, could certainly give rise to such a scenario.

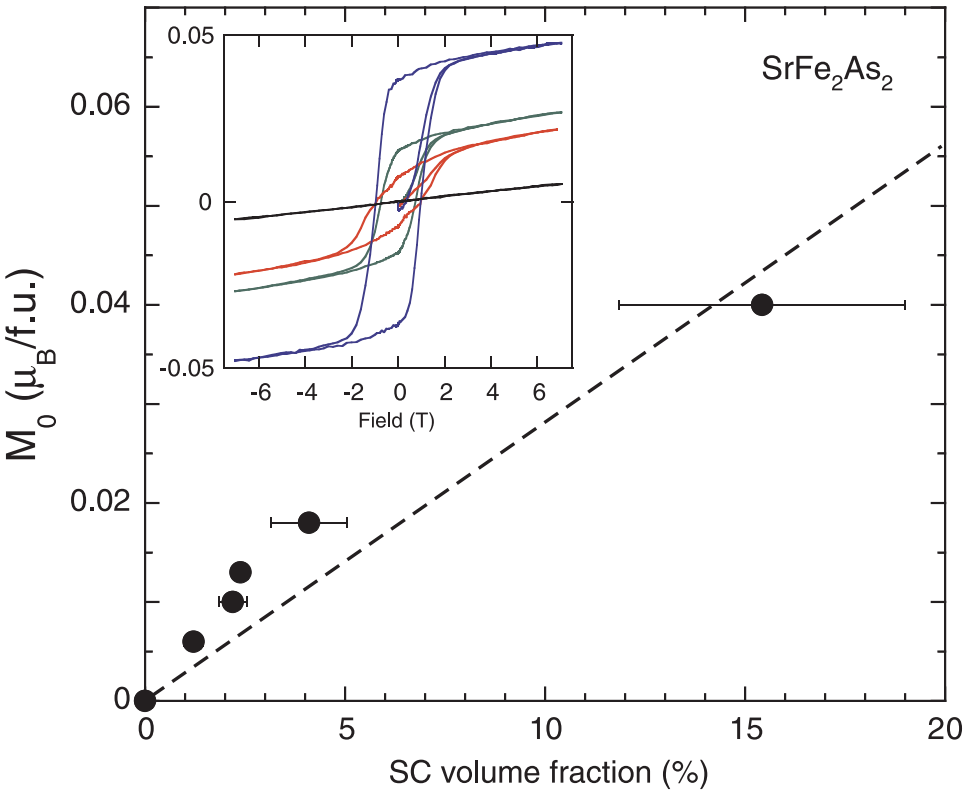

Figure 3.10: Ferromagnetic moment and superconducting volume fraction at 1.8 K for several samples of $SrFe_2As_2$ exhibiting a proportional relationship. The data presented here (in order of increasing volume fraction starting with zero) is for samples R1, b1 m9, b2 m2, b1 a, and b1 m12. Inset: Magnetization hysteresis loops at 1.8 K. The non-superconducting sample exhibits linear paramagnetic field dependence. The ordered moment in superconducting samples was estimated by linear extrapolation from high fields, while the superconducting volume fraction was deduced from the slope of the virgin curve in the Meissner state (from Ref. [1]).

3.6 Conclusions

I studied the ambient pressure superconducting phase that appears in a majority of single-crystal samples of $SrFe_2As_2$ synthesized using the self-flux method. I performed resistivity and magnetization measurements of samples subject to heat treatment and mechanical stress tests. The partial volume fraction superconductivity was shown to be suppressed by modest heat treatments, and can be reinstated by applying (and subsequently releasing) quasihydrostatic pressure or subjecting the material to severe mechanical stress.

The cause of this superconductivity appears to be related to the lattice strain which is corrobrated by x-ray diffraction measurements of single crystals. Studies of pressure-induced superconductivity in the 122 parent compounds have indicated a quite narrow region of full-volume fraction superconductivity [112], most evident in the case of $CaFe_2As_2$ where hydrostatic (He gas) pressure conditions have revealed the absence of superconductivity over any sizable range of pressure [41], in contrast to that originally reported [113, 111]. Given that the superconducting phase described in this chapter is likely strain induced, I suspect that superconductivity in all of these materials may share a similar mechanism, especially in the case of $SrFe_2As_2$, where a similar T_c of 21 K is also reported [112]. It would be interesting in the future to check for a ferromagnetic moment associated with superconductivity in pressure-induced superconducting systems. If the superconductivity comes from nonhydrostatic pressure conditions as it seems to in $CaFe_2As_2$ then we might expect to see nonhydrostatic pressure induce a ferromagnetic moment that would

not be present under hydrostatic pressure conditions. Finally, I was unable to determine the change in superconducting volume fraction in the mechanical deformation study. Further studies should attept to determine whether physical deformation also induces a ferromagnetic moment.

Chapter 4

Isovalent Elemental Substitution in the [Ca,Sr,Ba]Fe_2As_2 Series

Portions of this chapter have been summarized or paraphrased from my published works, references [3] and [4].

A key question in the quest to understand the mechanism behind high-temperature superconductivity in iron-pnictide and iron-chalcogenide based materials involves understanding the roles of structure and magnetism, and the interplay between them [36, 118, 101]. For magnetism, there is an ongoing debate in classifying the nature of spin interactions. While a local moment Heisenberg exchange interaction can be used to describe high-energy spin waves [119, 120], unphysical anisotropic interactions, as well as a small magnetic moment size [121, 122], point to a more complicated scenario involving itinerant magnetism, frustration [123, 124, 125], orbital order [126], or an even more complex scenario [119, 127, 128]. The nature and role of bonding between iron and arsenic is widely thought to hold the key to understanding the intriguing physical properties of iron-based superconductors. Strong covalency [121] and sensitivity to the degree of As-Fe hybridization [129] are

associated with the strong lattice collapse observed in $CaFe_2As_2$ under pressure [14] and chemical substitution [50].

The internal $FeAs_4$ structure, in particular, the specific shape of the iron-pnictide tetrahedron, is believed to play a key role in driving structural and magnetic transitions in the iron-pnictide materials[130, 131], and continues to appear important to superconducting properties. In particular, the correlation between an ideal tetrahedral bond angle and an optimal superconducting critical temperature of the ferropnicitides [14, 131, 132, 133] remains as an elusive property of obvious importance.

The parent compounds Ba-, Sr-, and $CaFe_2As_2$ have been studied extensively [10, 12, 13, 110, 134, 80] and were all found to be antiferromagnetic at low temperatures with Neél ordering temperatures of approximately 135, 200, and 165 K, respectively. Here I demonstrate that an intimate relationship exists in the (Ba,Sr,Ca)Fe_2As_2 series of compounds between the tetrahedral substructure and the stabilization of long-range magnetic order, with an intriguing evolution of the magnetic ordering temperature as a function of alkaline earth substitution that is dictated by the tetrahedral structure. Resistivity, magnetic susceptibility, neutron scattering, and x-ray crystallography measurements were used to study the evolution of magnetic order and crystallographic structure in single-crystal samples of the $Ba_{1-x}Sr_xFe_2As_2$ and $Sr_{1-y}Ca_yFe_2As_2$ series. A nonmonotonic dependence of the magnetic ordering temperature, T_0 on chemical pressure is found. I then compare this to the progression of the antiferromagnetic staggered moment, characteristics of the ordering transition. Structural parameters reveal a distinct relationship be-

tween the magnetic energy scale and the tetrahedral bond angle, even far above T_0. In $Sr_{1-y}Ca_yFe_2As_2$, an abrupt drop in T_0 occurs precisely at the Ca concentration where the tetrahedral structure approaches the ideal geometry. This suggests a strong coupling between the orbital bonding structure and the stabilization of magnetic order. It also suggests a direct relationship between structural tuning and the magnetic energy scale of the iron-based superconducting materials.

4.1 Experimental Details

Single-crystal samples of $Ba_{1-x}Sr_xFe_2As_2$ and $Sr_{1-y}Ca_yFe_2As_2$ were grown using the FeAs self-flux method described in ref. [1] and in section 2.1.1. Crystals were synthesized by first reacting Fe (99.999 % purity) and As (99.99 %) to form FeAs, then mixing with Sr (99.95 %) and heating the mixture, following a growth schedule similar to that described in section 2.1.1. Crystal structures were refined (SHELXL-97 package) using the I4/mmm space group against 113 and 106 independent reflections measured at 250 K with a Bruker Smart Apex2 diffractometer and corrected for absorption using the integration method based on face indexing (SADABS software). Substitution concentrations x and y were refined to within ± 0.01 of the values quoted below, with final R factors in the range 1-2%. See Appendix A for complete crystallographic x-ray refinement data for $Ba_{1-x}Sr_xFe_2As_2$ and $Sr_{1-y}Ca_yFe_2As_2$ crystals.

A chemical analysis was obtained via both energy-dispersive and wavelength-dispersive x-ray spectroscopy, showing 1:2:2 stoichiometry and Ca concentration

values reported herein. Resistivity ρ was measured with the standard four-probe ac method and magnetic susceptibility, χ was measured in the MPMS system. Neutron scattering experiments were performed on single-crystal samples using the BT9 triple axis spectrometer at the NIST Center for Neutron Research in Gaithersburg, MD. The neutron diffraction measurements were made using the (002) reflection from a pyrolitic graphite monochromator, which yielded a fixed incident wavelength of 2.359 Å. For measurements of the structural transition, the diffracted beam was analyzed using the (002) reflection of a pyrolitic graphite crystal, and tight collimations of 10'-M-10.7'-S-10'-A-10' were used, where M, S, and A are the monochromator, sample, and analyzer, respectively. Magnetic moments and order parameter temperature dependence were determined using a two-axis mode with 40'-M-47'-S-42' collimation.

4.2 Characterization of Transition Temperatures

To invstigate the effects of chemical pressure on the magnetic and structural transitions in 122 materials I synthesized solid solutions of $Ba_{1-x}Sr_xFe_2As_2$ and $Sr_{1-y}Ca_yFe_2As_2$. In figure 4.1 I present the results from the elemental analysis and sample characterization (see also refs. [135] and [136] for additional studies providing similar results). Panel (a) presents the results of WDS measured at 8 points on a characteristic crystal. This plot allowed me to to compare the nominal stoichiometry of the growth to the actual concentration of the single crystals. I find close agreements with the dashed line ($x_{nominal} = x_{measured}$) and thus use the nominal

concentration to report the results of transport and susceptibility measurements.

Figs. 4.1(b) and 4.1(c) present the crystallographic data on these samples. Indeed, alkaline earth substitution does appear to be acting as chemical pressure; as we move from Ba to Sr to Ca (decreasing atomic radii) both the c-axis and a-axis lattice constants decrease linearly, following Vegard's law, as do the volume and the c/a ratio. Furthermore, each of these decrease continuously as a function of substitution and at the same rate for both series, showing that the choice of alkaline earth substitution provides a tunable and uniform chemical pressure effect. Interestingly, as will be shown in the following section, the antiferromagnetic transition T_0 does not follow a monotonic evolution with unit cell volume. Rather, I found a maximum in $SrFe_2As_2$ near 200 K with lower values of 135 and 160 K in $BaFe_2As_2$ and $CaFe_2As_2$, respectively. With magnetic order in these materials likely being at least partly itinerant in nature [137], the value of T_0 will depend on details of the electronic structure [e.g., the antiferromagnetic (AFM) nesting condition for a spin-density wave model] and hence may indirectly depend on unit cell parameters. In such a scenario, abrupt changes in T_0 with alkaline substitution are not expected as long as the change in chemical pressure is uniform and monotonic.

As shown in Fig. 4.2, the substitution of Sr into $Ba_{1-x}Sr_xFe_2As_2$ and Ca into $Sr_{1-y}Ca_yFe_2As_2$ appears to induce very little qualitative change in either ρ(T) or χ(T) as a function of substitution; the material always remains metallic with a RRR$\sim$2. An abrupt feature appears in both ρ(T) and χ(T) at the magnetostructural transition T_0, which climbs to 200 K in the $Ba_{1-x}Sr_xFe_2As_2$ series and then remains ominously fixed until very high Ca concentrations in the $Sr_{1-y}Ca_yFe_2As_2$ series,

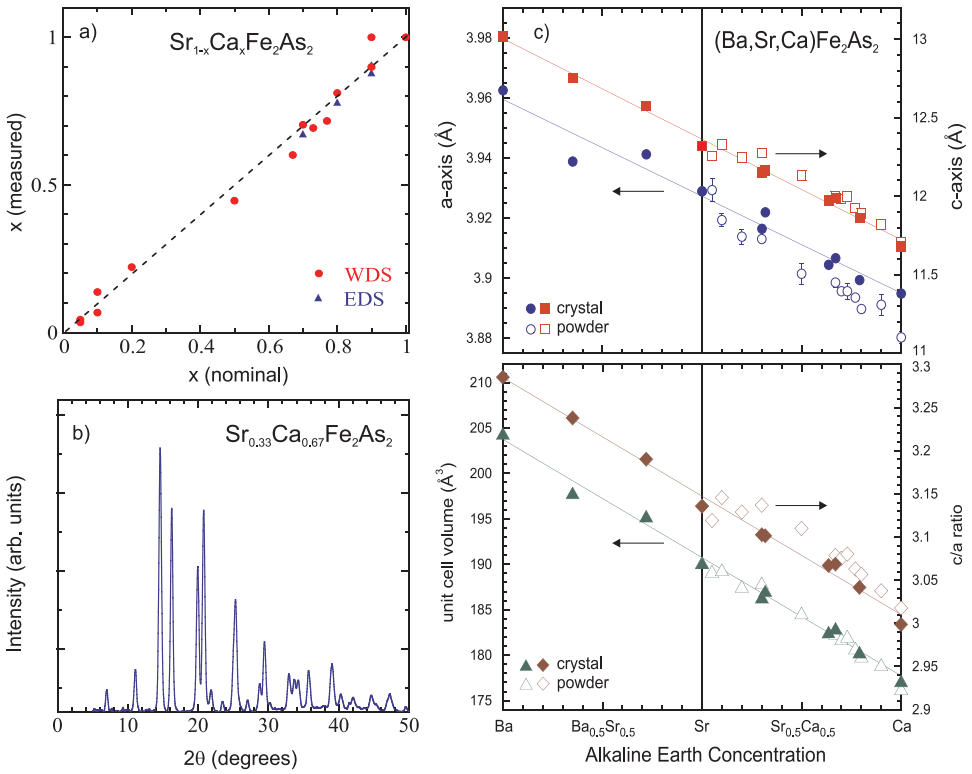

Figure 4.1: (a) Measured Ca concentration of $Sr_{1-x}Ca_xFe_2As_2$ single-crystal samples as a function of nominal concentration x, as determined by wavelength dispersive x-ray spectroscopy (data points represent an average value of 8 scanned points for each concentration). Some of the specimens are also confirmed by energy dispersive X-ray spectroscopy (EDS). The dotted line is a guide to eye which traces x(measured) = x(nominal). (b) Typical x-ray powder diffraction pattern, shown for sample $Sr_{0.33}Ca_{0.67}Fe_2As_2$, obtained by using Mo-$K_\alpha$ radiation. The main peaks can be indexed with a tetragonal structure and there are no impurity phases detected within experimental accuracy. (c) Upper panel: Variation of the a- and c-axis lattice constants as a function of alkaline earth substitution in the series $Ba_{1-x}Sr_xFe_2As_2$ (left half) and $Sr_{1-x}Ca_xFe_2As_2$ (right half) as determined from single crystal x-ray diffraction measurements at 250 K of single-crystal samples. Corresponding c/a ratio and the unit cell volume are plotted in the lower panel. In both panels, solid symbols indicate data acquired using single-crystal specimens and open symbols represent data determined by powder x-ray diffraction, (from Ref. [4]).

where it begins to decrease in temperature toward 165 K in $CaFe_2As_2$.

No obvious change is observed in the qualitative shape of the T_0 transition in χ(T) data. Fig. 4.2(b) shows a steplike feature through the entire range of substitutions that remains almost identical in width and height. In contrast, the transport feature associated with T_0 (Fig. 4.2(a)) displays a continuous evolution from a simple but sharp shoulder in $Ba_{1-x}Sr_xFe_2As_2$ toward a pronounced steplike feature in $CaFe_2As_2$. It is unknown exactly why this change in character is seen in the transport measurements, but is likely due do the competition between an increase in scattering off of magnetic centers and a decrease in magnetic fluctuations.

First order transitions are associated with a latent heat and a hysteresis in the transition temperature whereas second order transitions do not have hysteresis or a latent heat. The steplike transition in ρ(T) that grows with increasing Ca concentration shows an increasing hysteresis and is consistent with the evolution of the transition from "weakly" to "strongly" first order in character. This feature is discussed in greater detail in section 4.3. This hysteresis is not seen at all in the $Ba_{1-x}Sr_xFe_2As_2$ series. *Ab initio* calculations suggest that this is due to a change in Fermi surface nesting features with lattice density [138]. Interestingly, both continuous and abrupt features associated with this evolution are shown by the progression of features in $\rho(T_0)$. As shown in Fig. 4.3, the emergence of the step feature at T_0 appears for even small concentrations of Ca substitution, and this feature continuously grows in size toward the pure Ca end. In contrast, a pronounced hysteresis between warming and cooling curves appears only at 70% Ca, increasing in temperature width very rapidly toward 100% Ca. This abrupt appearance of a strong

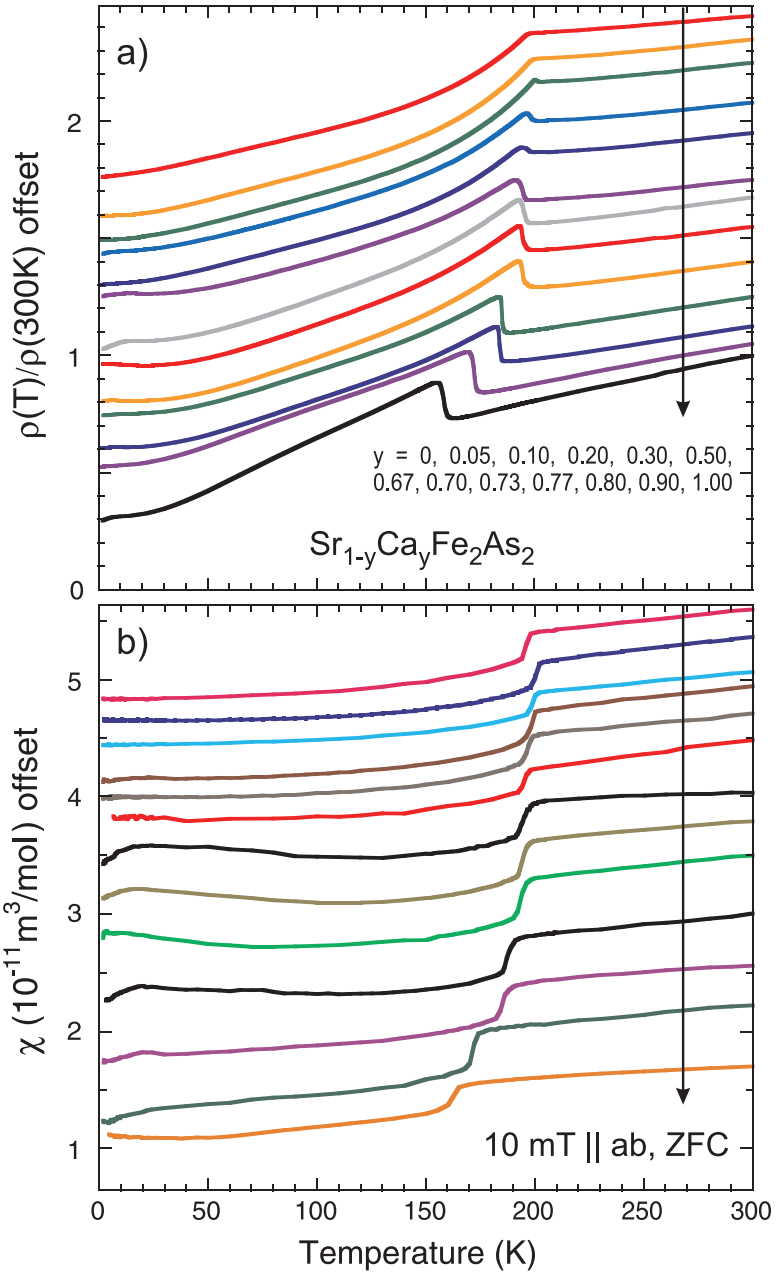

Figure 4.2: (a) Evolution of electrical resistivity of single-crystal samples of $Ba_{1-x}Sr_xFe_2As_2$ and $Sr_{1-y}Ca_yFe_2As_2$ with alkaline earth substitution, normalized to 300 K, and offset from y = 1 for clarity. (b) Magnetic susceptibility of $Ba_{1-x}Sr_xFe_2As_2$ and $Sr_{1-y}Ca_yFe_2As_2$ crystals measured in a 10 mT field oriented along the basal plane direction, and offset from y = 1 for clarity, (from Ref. [3]).

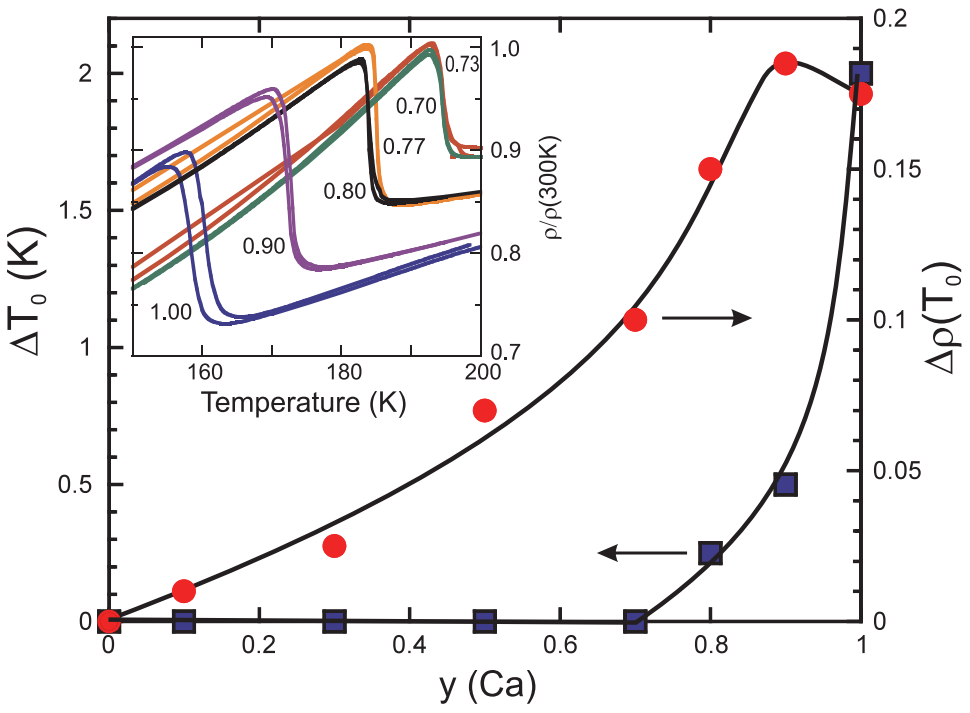

Figure 4.3: Characterization of the first-order antiferromagnetic transition observed in electrical resistivity measurements of $Sr_{1-y}Ca_yFe_2As_2$, showing the temperature width of thermal hysteresis ΔT_0 (squares) observed in resistivity data (inset), as well as the relative magnitude of the jump in resistivity $\Delta\rho(T_0)$ (circles) relative to $\rho(300\ K)$, (from Ref. [3]).

first-order character is coincident with a sudden decrease in T_0 with increasing Ca content near a critical concentration $y_c = 0.70$.

It is important to note here, however, that while I refer to this as chemical pressure there must be some additional factor that can account for the superconductivity seen in this system. In a similar study by Rotter *et al.* [136], the lattice volume of $Ba_{1-x}Sr_xFe_2As_2$, $BaFe_2As_{2-x}P_x$, and $BaFe_2As_2$ under pressure were compared. It was shown that for a volume between approximately 192 and 200 Å^3, $BaFe_2As_{2-x}P_x$ and $BaFe_2As_2$ under pressure were found to superconduct. In that same volume range, however, $Ba_{1-x}Sr_xFe_2As_2$ ($0.4 \leq x \leq 0.9$) does not exhibit

superconductivity. Indeed, it seems that chemical pressure is not enough to fully describe the properties of this system. Rotter *et al.* pointed out that even very small changes to the crystal structure must be investigated to truly understand the effect that substitution has on magnetism and superconductivity in these systems. I agree with their assessment and use this as motivation to study the As-Fe-As bond angle (see section 4.4)

4.3 Magnetic Order Parameter

Specific heat measurements of 122 materials show that the magnetic transition in the parent compounds is 2^{nd}-order in $BaFe_2As_2$ [139], 1^{st}-order in $CaFe_2As_2$[140], and something in-between in $SrFe_2As_2$ [109] as determined by the presence or absense of a latent heat at the transition. Theoretical calculations by Zhang *et al.* attribute this to the nesting features of the Fermi surface [138]. In order to probe the nature of the magnetic transition through the critical concentration in $Sr_{1-y}Ca_yFe_2As_2$ where the transition begins to show more first-order-like behavior, elastic neutron scattering experiments were performed on several single-crystal samples of $Sr_{1-y}Ca_yFe_2As_2$.

Figure 4.4(a) presents an image plot demonstrating the tetragonal to orthorhombic transition in $Sr_{0.3}Ca_{0.7}Fe_2As_2$. This image was generated from θ-2θ scans of the tetragonal phases (220) Bragg peak, which splits abruptly at T_0 into the (400) and (040) Bragg peaks of the orthorhombic phase. In Fig. 4.4(b), I show that the magnetic order parameter obtained from the (103) magnetic Bragg peak

remains surprisingly similar across the Sr-Ca series. It shows an abrupt onset at T_0, consistent with a first-order transition, as evidenced by a lack of critical scattering both above and below T_0 in both $SrFe_2As_2$ (Ref. [119]) and $CaFe_2As_2$ (Ref. [120]) end members.

From Figs. 4.4 and 4.5 The temperature dependence of the ordered moment does not visibly change through the entire range of Ca concentrations. Fitting to a mean-field or power law form (shown by solid lines) yields an exponent $\sim T^{0.20}$ (constant within error for all concentrations studied) that lies between those reported for $BaFe_2As_2$ ($\sim T^{0.10}$) and several doped systems with larger exponents ($\sim T^{0.25}$) [141], but is obviously strongly affected by the presence of a first-order jump in the order parameter.

Similar to transport and susceptibility data discussed above, the AFM ordering transition as measured by neutron diffraction is independent Ca concentration until it reaches high concentrations, where it begins to drop toward the $CaFe_2As_2$ end member value. Surprisingly, aside from the abrupt decrease in T_0 above $y_c = 0.70$, there is no change in behavior of the magnetic order parameter, either qualitatively or quantitatively, through this critical concentration. This includes the size of the ordered moment, which remains at $0.9\mu_B$ across the entire (Ba,Sr,Ca)Fe_2As_2 series to within experimental error [Fig. 4.5(b)], as well as the order parameter temperature dependence itself [Fig. 4.4(b)]. Together with the featureless evolution of the character of the transition in χ(T) data and the transformation observed in ρ(T), this suggests that the T_0 transition has more impact on the charge carriers than the magnetic response. This behavior is consistent with an itinerant (*i.e.*, spin-density

wave) form of the magnetic order.

4.4 Evolution of Structural and Magnetic Properties with Alkaline Earth Substitution

The lack of correspondence between T_0 and the size of the ordered moment puts strong constraints on the nature of the magnetic interaction. In a simple model of AFM, the Néel temperature is proportional to both the ordered (staggered) moment and the exchange coupling. In contrast to the direct proportionality between T_0 and the ordered moment observed in both Co- (Ref. [142]) and Ru-doped[143] $BaFe_2As_2$, as well as P-doped CeFeAsO[144], the absence of any correlation between the ordered moment size and T_0 in $Sr_{1-y}Ca_yFe_2As_2$ suggests that the variation of T_0 in the (Ba,Sr,Ca)Fe_2As_2 series results primarily from the tuning of exchange. Lacking any direct manipulation of electronic structure in this series (*e.g.,* from charge doping), structural tuning must play a direct role in setting the magnetic energy scale.

I used refinements of single-crystal x-ray data for the $Ba_{1-x}Sr_xFe_2As_2$ and $Sr_{1-y}Ca_yFe_2As_2$ series obtained at 250 K (see Appendix A). Fig. 4.5 shows the internal structure of the unit cell is plotted in the form of As-Fe-As tetrahedral bond angles α and β, together with the evolution of T_0 and the ordered moment. While showing a general procession that is indicative of a greater sensitivity to a-axis reduction than the c-axis decrease across the series [4], a nonmonotonic inflection in both angles appears to coincide precisely with the critical concentration y_c. This is

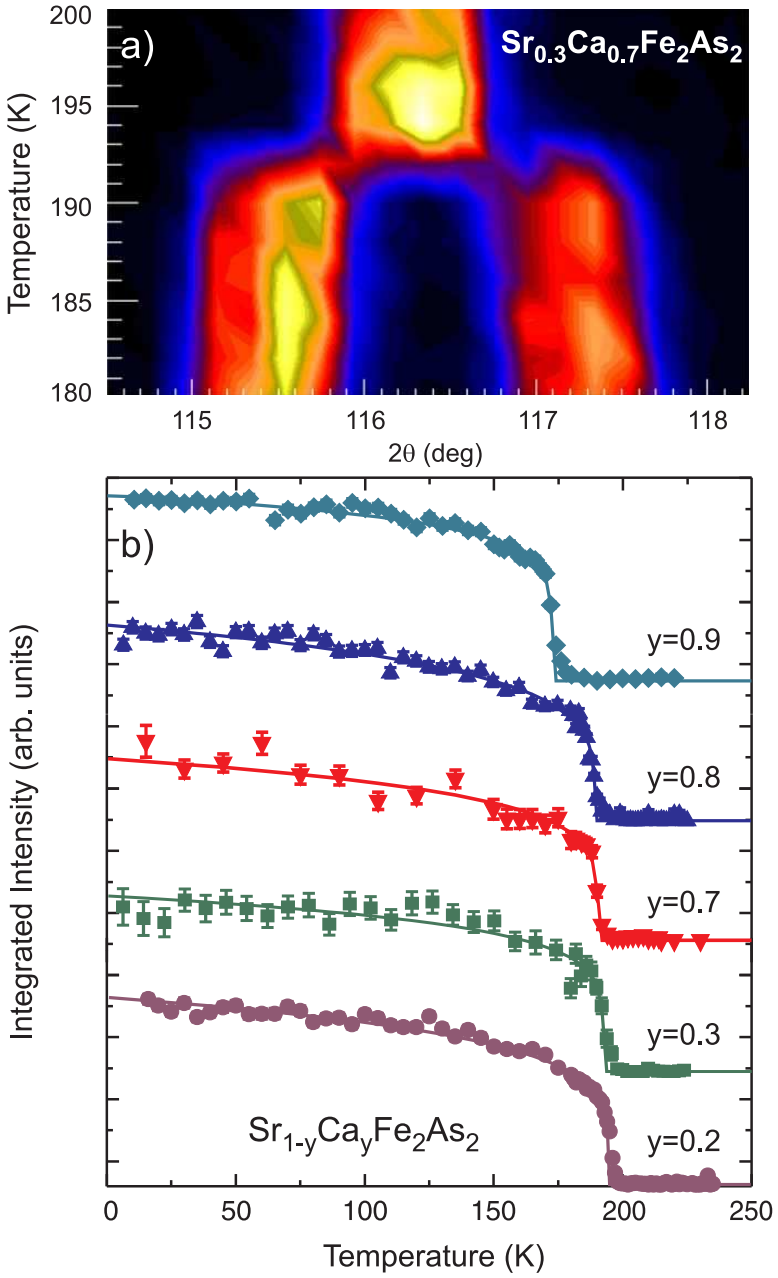

Figure 4.4: (a) Evolution of the (220) structural peak through the magnetic/structural transition in $Sr_{0.3}Ca_{0.7}Fe_2As_2$, demonstrating the abrupt onset of orthorhombic splitting at $T_0 = 193$ K. (b) Magnetic order parameter of $Sr_{1-y}Ca_yFe_2As_2$ single crystal samples (errors represent one standard deviation) obtained from the (103) magnetic peak. Lines are fits as discussed in the text, (from Ref. [3]).

clear evidence for a direct correlation between the magnetic energy scale and details of the internal crystal structure involving the FeAs layer. Moreover, with signatures of the mechanism that controls the energy scale for magnetic ordering occurring well above T_0 (i.e., at 250 K), it appears that the crystal structure plays a precursor role in determining the magnetic energy scale.

The sensitivity of the magnetic order to fine tuning of the lattice structure is surprising in light of (a) the strong first-order nature of the magnetic transition, and (b) the widely held view that the structural transition that accompanies T_0 is driven by magnetic interactions (and not vice versa) [36, 118, 101]. However, with critical scattering persisting up to temperatures high above T_0 [145], it is possible that magnetic interactions do play a primary role. But because there is no clear indication of a local-moment type order (e.g., no direct relationship between ordering and any structural bond length that would tune J), it is tempting to assign the observed coupling between magnetic ordering and structure to details involving the electronic structure. In particular, the nesting condition that is thought to favor magnetic ordering in the parent compounds and to play a vital role in optimizing superconductivity [146]. Measurements probing this idea, such as photoemission and quantum oscillation experiments, are thus a promising route to elucidating the tie between magnetic and structural features of the iron pnictides.

Finally, I note that while the tetrahedral bond angle never drops below 110° through the (Ba,Sr,Ca)Fe_2As_2 series, it comes very close to the value of 109.47° expected for an ideal tetrahedral geometry at the critical concentration y_c. In particular, an extrapolation of α to $x = 1$ yields a value very close to 109.47°, suggesting

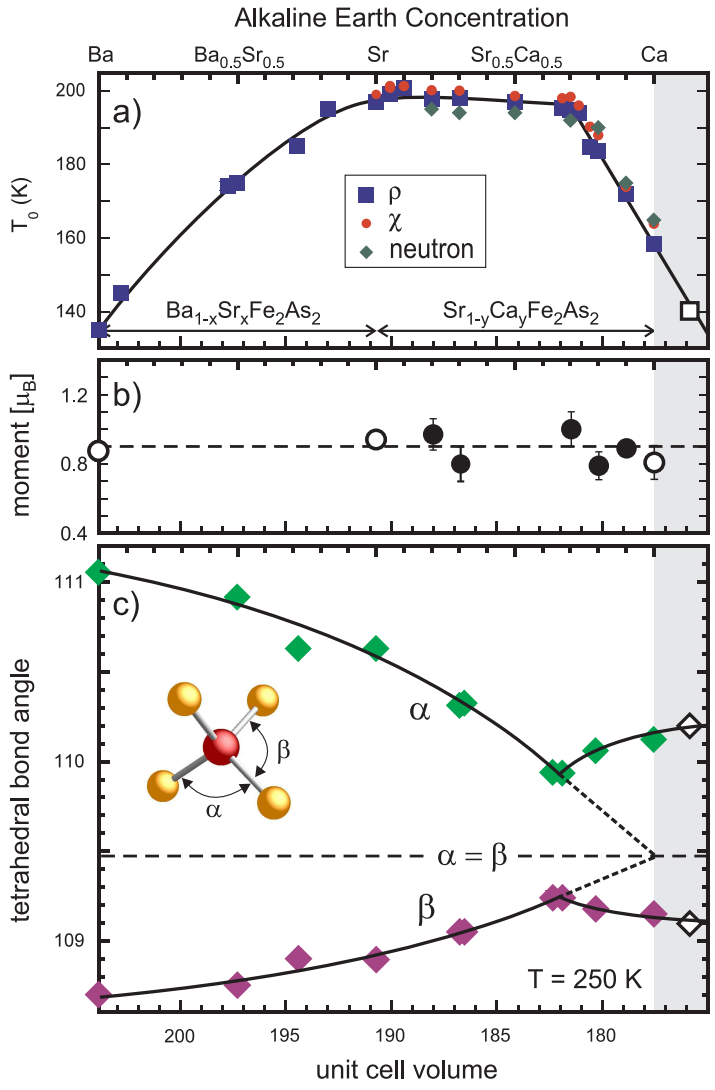

Figure 4.5: Evolution of structural and magnetic properties of $Ba_{1-x}Sr_xFe_2As_2$ and $Sr_{1-y}Ca_yFe_2As_2$ as a function of solution concentration (top axis) or experimental unit cell volume (bottom axis). (a) Magnetic transition T_0 identified by resistivity (squares), susceptibility (circles), and neutron scattering (diamonds); (b) staggered moment of the antiferromagnetic phase [data for $BaFe_2As_2$, $SrFe_2As_2$, and $CaFe_2As_2$ (open circles) obtained from Refs. [10, 11, 12], respectively], with the dashed line indicating a moment size of 0.9 μ_B; (c) tetrahedral bond angles α and β as identified in the graphic (See online supplemental material for reference [3] or appendix A). The dashed line indicates the ideal tetrahedron geometry where $\alpha = \beta = 109.47°$. The shaded regions indicate transition (Ref. [13]) and bond angle (Ref. [14]) data for $CaFe_2As_2$ at 0.23 GPa, (from Ref. [3]).

that the application of pressure may drive a sample with y = y_c closer to this value. This particular concentration is ideal for further study of the relationship between structure and superconductivity that has been previously highlighted. I have collaborated with Jason Jeffries at Lawrence Livermore National Laboratory to do exactly this: we studied the transport and crystallographic properties of $Ca_{0.67}Sr_{0.33}Fe_2As_2$ under pressure and found that the properties of the system under pressure the system are between $CaFe_2As_2$ and $SrFe_2As_2$. We find that pressure drives the system further from the ideal bond angle, and that the system exhibits superconductivity up to 22 K between 1 and 4 GPa. There does not appear to be any correlation between and structural parameter and T_c. however it is interesting to note here that the rate of suppression of magnetism is faster for $Ca_{0.67}Sr_{0.33}Fe_2As_2$ and $CaFe_2As_2$ than $SrFe_2As_2$. In any case, these results suggest that both the evolution of the internal crystal structure and the onset of the collapsed tetragonal phase may play a role in the development of pressure induced superconductivity [147].

4.5 Conclusions

We grew single crystals of $Ba_{1-x}Sr_xFe_2As_2$ and $Sr_{1-x}Ca_yFe_2As_2$ and measured structural and transport properties. The unit cell volume, as well as the a- and c-axis paramters decrease monotonically in both series, however the magnetic/structural transition temperature first increases from $BaFe_2As_2$ to $SrFe_2As_2$, then decreases from $SrFe_2As_2$ to $CaFe_2As_2$. Although isovalent substitution that changes the unit cell volume is often called "chemical pressure", this term may not be entirely ac-

curate given that under pressure these materials exhibit superconductivity. We investigated the internal crystal structure, in particular the $FeAs_4$ structure and the the specific shape of the iron-pnictide tetrahedron and found that thought the unit cell volume seems to have no impact on T_0 the tetrahedral bond angle does, and when the bond angle changes rapidly at y_c so does T_0. Finally, the fact that the temperature dependence and magnitude of the ordered moment does not change with AE substitution suggests that it is the structural transition that has more impact on the charge carriers than the magnetic ordering which is consistent with itinerant magnetism.

Future studies on the pressure dependence of the magnetic moment could be useful in determining how superconductivity in these systems is induced. Despite the fact that isovalent substitution produces a volume change comparable to that seen in superconducting samples under pressure or charge doping it does not induce superconductivity, which implies that either charge doping or some other effect of pressure is necessary to stabilize superconductivity. In the future it would be interesting to study the effect of pressure on the carrier concentration in these systems.

Chapter 5

Comparison of Ni- and Pt- substitution in $SrFe_2As_2$

Portions of this chapter have been summarized or paraphrased from several of my publications, Refs. [5, 6, 7, 8].

Suppression of magnetic and structural phase transitions, either by charge doping or high pressure, plays a key role in stabilizing superconductivity in iron-based superconductors. In the 122 family of materials, transition temperatures as high as 25 K have been induced by partial substitution of transition metal elements on the Fe site. Most of the combinations of transition-metal substituted $AEFe_2As_2$ (AE = Ca, Sr, Ba) systems have been reported including $BaFe_{2-x}Co_xAs_2$ [110, 44, 42], $SrFe_{2-x}Co_xAs_2$ [15, 148], $BaFe_{2-x}Ni_xAs_2$ [24, 82], $SrFe_{2-x}M_xAs_2$ (M= Rh, Ir, and Pd) [16]. Interestingly, in $BaFe_{2-x}Co_xAs_2$, the maximum T_c is found at x $\sim$0.17, whereas in $BaFe_{2-x}Ni_xAs_2$, the maximum T_c occurs at approximately x =0.10, this suggests that Ni substitution may indeed contribute twice as many d-electrons to the system as Co. As implied by the enhanced negative thermoelectric power value in the normal state [7, 24] Co and Ni substitution appear to donate negative charge carriers that are thought to lead to superconductivity. This picture is also supported

by the rigid band shift seen in angle resolved photoemission spectroscopy (ARPES) measurements [149, 150].

This model in which we treat Co- and Ni- substitution for Fe as adding one and two excess electrons has been challenged by several groups. In this model Co is expected to ionize as Co^{3+} and Ni as Ni^{4+}, but several studies have shown that this may not be the case. X-ray absorption studies sensitive to the oxidation state (called x-ray absorption near-edge spectroscopy, or XANES) have shown that the Co atoms are indeed oxidized in the Co^{2+} state [151, 152], a conclusion that has also been confirmed by Mössbauer studies [153]. Theoretical calculations by several groups have shown that the excess electrons in transition-metal stubstituted materials are localized around the impurity sites [154, 155, 156], which contadicts the charge doping model.

If transition metal substitution can be seen purely as charge doping then hole doping on the Fe site and electron doping on the alkaline earth site should both induce superconductivity. Recent reports of superconductivity in lanthanide substitution on the alkaline earth site in 122s has been published (see ref. [50] for one such example), however older studies found that Cr- and Mn substitution (nominally hole doping) do not induce superconductivity in $BaFe_2As_2$ [157, 158], once again in disagreement with the charge doping picture.

Finally, this charge doping model does not explain the difference in T_c observed between systems. The group at AMES Lab showed that the onset and offset of the superconducting dome, as well as the optimal concentration where T_c is highest, scales very well with the electron density in transition metal substituted $BaFe_2As_2$

(see also Fig. 6.2) [19]. However there is as yet no explanation for why the transition temperature is lower in the Ni- and Pd- substituted systems as compared to the Co- and Rh- substituted ones. One goal of my study is to create a phase diagram for TM substitution in the $SrFe_2As_2$ system to determine whether the charge doping model can account for the superconducting phase as well as it does in the $BaFe_2As_2$ system.

In this chapter I present transport and magnetic susceptibility data on single crystals of Ni and Pt substituted $SrFe_2As_2$. I use this data to discuss what effects transition metal substitution has in the 122 system and will compare our results to other previously reported systems. I show that, like the studies performed on transition metal substituted $BaFe_2As_2$ [19], Ni and Pt substitution cause a shift in the Hall coefficient consistent with electron doping. I find that the optimal concentration where T_c is the highest and the magnetic transition is suppressed ($T_N = 0$) is the same for Ni and Pt substitution, however the superconducting dome is larger in the Pt case: the optimal T_c is higher and the range of doping over which superconductivity is observed is wider. I use these results to motivate the final discussion in Chapter 6.

5.1 $SrFe_{2-x}Ni_xAs_2$

Despite their lower values of superconducting transition temperature T_c relative to the 1111 materials, the 122 compounds can be prepared as large single crystals and are well-suited for experimental study. One particularly interesting

aspect of the superconductivity in 122 materials is the similarity of maximal T_c (20-25 K) for the different transition metal substituents. This trend is known to be broken in just a few systems: $SrFe_{2-x}Pd_xAs_2$ [16], Co/Cu substituted $BaFe_2As_2$ [159], and Ni- and Pt- substituted $SrFe_2As_2$ as I will show in this chapter. To investigate the effects of Ni substitution in an as yet unexplored series of the FeAs-based 122 compounds, I performed a study of the evolution of superconductivity in single crystalline $SrFe_{2-x}Ni_xAs_2$. Here I discuss superconductivity induced by Ni substitution in the series $SrFe_{2-x}Ni_xAs_2$ with maximum T_c (onset) of 9.8 K. By studying a wide range (x=0-0.30) of single-crystal samples, I established a new member of the 122 series with superconductivity induced by transition metal substitution for Fe. Contrary to prior studies of similar compounds, I observed a relatively low $T_{c,max} \leq 10$ K in this series, centered at a Ni concentration approximately half that of the optimal Co concentration in $SrFe_{2-x}Ni_xAs_2$ [44, 148]. Below, we discuss the evolution of electrical transport, magnetic and thermodynamic quantities as a function of Ni concentration as well as other characteristics of the doping-induced superconductivity in this system.

5.1.1 Growth and Characterization

Single crystals of $SrFe_{2-x}Ni_xAs_2$ were grown and characterized using the techniques described in previous chapters (see section 2.1.1). Figure 5.1(a) presents crystallographic a- and c-axis lattice constants determined from fits to x-ray diffraction patterns of powdered samples of $SrFe_{2-x}Ni_xAs_2$ as a function of Ni concentration

x. The resultant tetragonal ratio c/a is shown in Fig. 5.1(b). With increasing x, the c-axis lattice constant decreases and the a-axis lattice constant increases, while the c/a ratio decreases linearly, without any significant change in unit cell volume to within experimental accuracy. Fig. 5.1(c) shows the Ni concentration determination in $SrFe_{2-x}Ni_xAs_2$ crystals measured by WDS analysis, using an average value determined from 10 different spots on each specimen, plotted as a function of nominal concentration x. Because a linear fit (dotted line) results in a slope of unity to within scatter, the nominal value of x will be used hereafter as an adequate representation of the actual concentration.

5.1.2 Effect of Annealing

One method of investigating the effect of crystalline quality is by high temperature heat treatment. Interestingly, we found that annealing single crystals of $SrFe_{2-x}Ni_xAs_2$ in certain ways can produce a rather dramatic enhancement in the value of T_c. We found that holding samples at 700°C for 24 hours in an Ar atmosphere increased T_c on average by approximately 1 K, however some crystals showed an enhancement of T_c as large as 50%. As shown in Fig. 5.2, the effect of annealing on the superconducting transition in $SrFe_{1.85}Ni_{0.15}As_2$ crystals is evident in both ρ(T) and χ(T), indicating that this enhancement is reflected in the full diamagnetic screening and is therefore a bulk phenomenon. Such an enhancement of T_c could be an indication of improved crystallinity due to release of residual strain, and/or improved microscopic chemical homogeneity of Ni content inside the

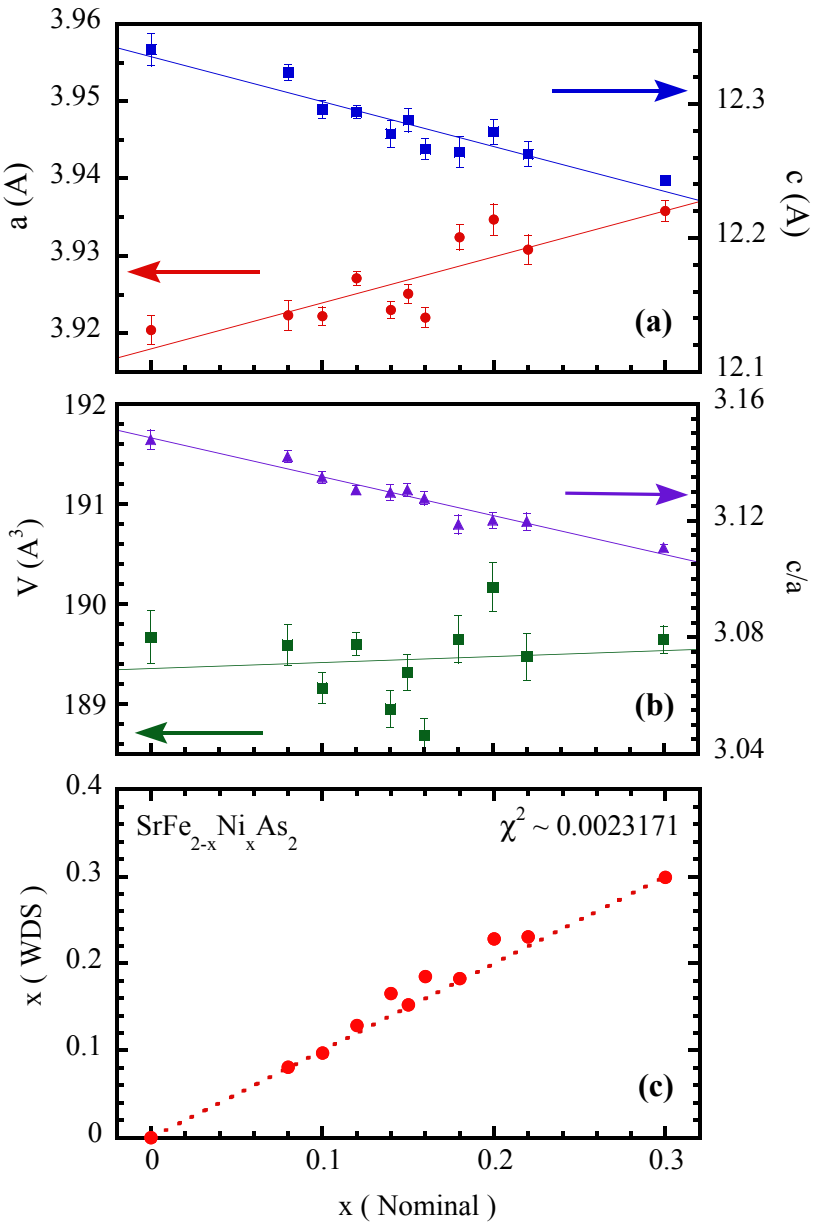

Figure 5.1: (a) Variation of the a- and c-axis lattice constants of $SrFe_{2-x}Ni_xAs_2$ with Ni content x, as determined from Rietfeld refinement of x-ray powder diffraction spectra; (b) Corresponding change of tetragonal c/a ratio and unit cell volume V; (c) Actual Ni concentration of $SrFe_{2-x}Ni_xAs_2$ single crystal samples as a function of nominal concentration x, as determined by wavelength dispersive x-ray spectroscopy (data points represent average value of 10 scanned points for each concentration, the dotted line is a linear fit with a slope of 1). From Ref. [5].

specimens, thereby optimizing the stability of superconductivity. A similar annealing effect was reported in LnFeOP (Ln=La, Pr, Nd) single crystals, where a heat treatment in flowing oxygen was also found to improve superconducting properties [160].

It is also noteworthy that as-grown crystals of $SrFe_{2-x}Ni_xAs_2$ for x $<$ 0.16 show what looks to be a partial superconducting transition near 20 K that is completely removed by heat treatment, as demonstrated in Fig. 5.2(a) for x = 0.15. Although it is tempting to posit that 20 K is a possible value for optimal T_c in this series of Ni-substituted compounds, note that aside from the enhancement of T_c as mentioned above, the removal of this feature is the only change I observed in measured quantities imposed by annealing: neither the resistivity nor the magnetic susceptibility in the normal state showed any change after annealing. Furthermore, susceptibility did not show any indication of diamagnetic screening above bulk T_c values in the as-grown samples. Because the 20 K kink is removed with heat treatment, and, moreover, is always found to be positioned near the same temperature, we believe this feature may be connected to the strain-induced superconductivity found in undoped $SrFe_2As_2$ (see Chapter 3). However, note that whereas only a mild 5-minute heat treatment of 300°C removes the partial volume superconductivity in $SrFe_2As_2$, a substantially higher-temperature 700°C treatment is required to remove this feature in $SrFe_{2-x}Ni_xAs_2$. If the two phenomena are related, it is possible that internal strain is stabilized by the chemical inhomogeneity associated with transition metal substitution in $SrFe_{2-x}Ni_xAs_2$ thus requiring higher temperatures to be removed.

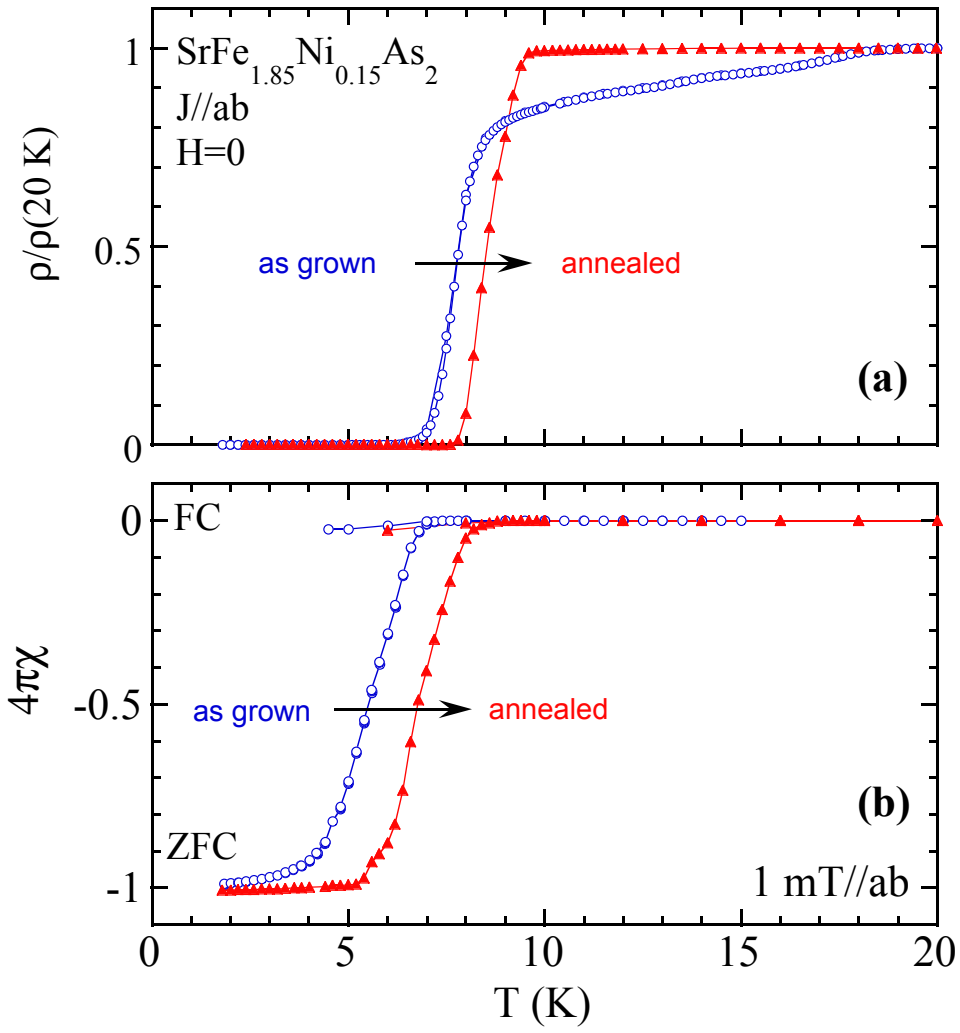

Figure 5.2: Effect of high-temperature annealing on an optimally doped x = 0.15 sample of $SrFe_{2-x}Ni_xAs_2$, demonstrating typical results from before and after a 24 hour, 700°C heat treatment performed on a sample sealed in a quartz tube with a pure argon environment. (a) Resistivity data of a x = 0.15 sample measured before (blue circles) and after (red triangles) heat treatment. (b) Volume magnetic susceptibility of a x = 0.15 sample at low fields measured before (blue circles) and after (red triangles) annealing. Arrows emphasize enhancement of T_c by annealing, with good agreement in T_c values for both cases. From Ref. [5].

I also performed a more systematic study on the effect of annealing on $SrFe_{2-x}Ni_xAs_2$ to determine the optimal annealing conditions. Figure 5.3 presents my results of different heat treatments on the superconducting transition detected in χ(T). A single crystal of $SrFe_{1.85}Ni_{0.15}As_2$ was annealed at 700°C after wrapping with Ta foil and sealing in a quartz tube under partial atmospheric pressure of Ar. Annealing for 7 and 14 days enhanced the T_c (onset) from $\sim$ 6.2 in the as-grown sample to $\sim$ 8.9 K and $\sim$ 9.2 K, respectively, with a sharpening of the transition. Annealing for 21 and 28 days did not enhance the T_c further, while it gradually reduced the superconducting volume fraction, indicating 14 days as the optimal annealing time. The inset shows the annealing time dependence of T_c. Such an enhancement of T_c could be an indication of improved crystallinity due to release of residual strain, and/or improved microscopic chemical homogeneity of Ni content inside the specimens, thereby optimizing the stability of superconductivity.

It is important to note that most of the resistivity and susceptibility measurements were performed before these optimization measurements. As such, all of the samples in this study were annealed at 700°C for 24 hours under an inert Ar atmosphere, rather than the 14 days that seems to provide the sharpest transitions.

5.1.3 Resistivity and Magnetization Measurements

Fig. 5.4(a) presents the comparison of the in-plane resistivity ρ(T) of single crystals of $SrFe_{2-x}Ni_xAs_2$ (data are presented after normalizing to room temperature and offsetting for clarity). As shown, ρ(T) data for $SrFe_2As_2$ exhibit metallic

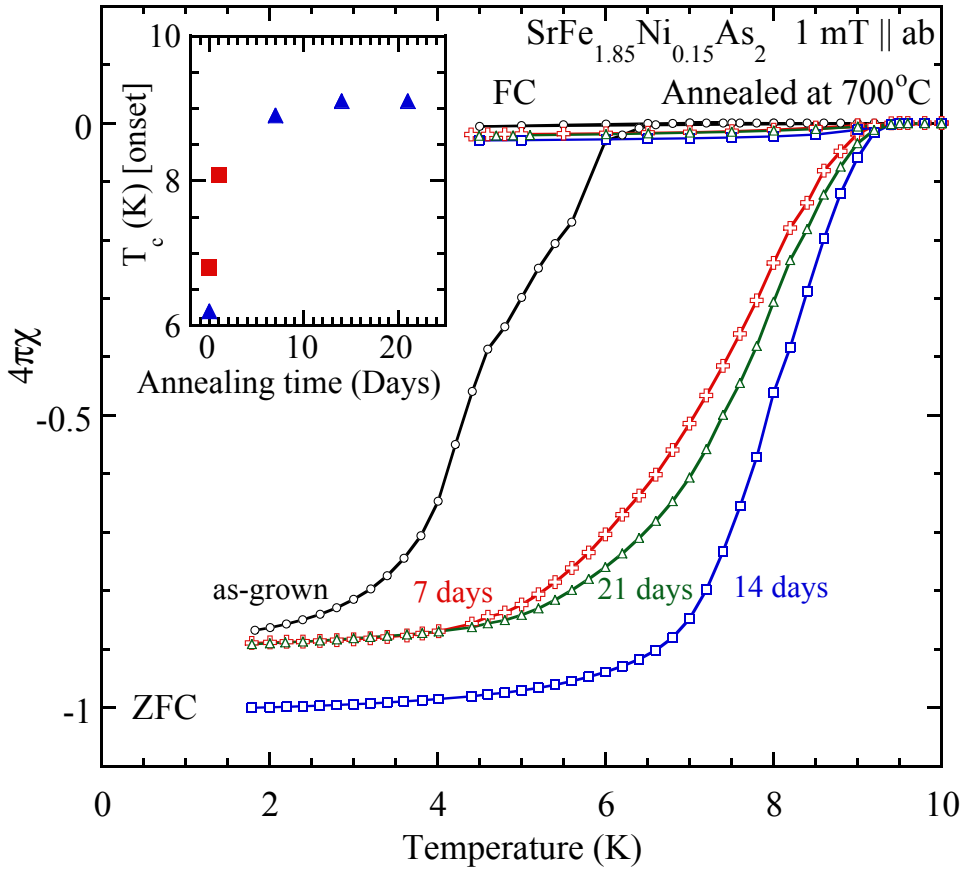

Figure 5.3: Volume magnetic susceptibility in a $SrFe_{1.85}Ni_{0.15}As_2$ sample measured before (circles) and after annealing a sample at 700°C for 7 days (pluses), 14 days (squares), 21 days (triangles), and 28 days (diamonds). The lines are guides through the data points. The inset shows the annealing time dependence of T_c for this sample (filled triangles). The enhancement of T_c in a second piece of sample annealed for 1 day is also plotted (filled squares). From Ref. [6].

behavior, decreasing with temperature from 300 K before exhibiting a sharp kink at $T_0 = 198$ K, where a structural phase transition (from tetragonal to orthorhombic upon cooling) is known to coincide with the onset of antiferromagnetic (AFM) order[109]. With increasing Ni substitution the anomaly associated with T_0 becomes less distinct and is defined by a smooth minimum in ρ(T), which shifts to lower temperature as indicated by the position of short arrows in Fig. 5.4(a), finally disappearing for $x > 0.15$ where no minimum is evident. We define the value of T_0 as the position of the kink in $x = 0$ data and the position of the minima in ρ(T) data for $0.08 \leq x \leq 0.15$, and present its evolution with Ni concentration in Fig. 5.5.

The sharp decrease in ρ(T) associated with T_0 in the undoped material is observed to change character with increased Ni substitution, as it is shifted to lower temperatures. This switch from a drop to a gradual rise in ρ(T) at T_0 with TM substitution has also been observed in other doped 122 materials [82, 19, 159, 24] and likely arises due to a shift in the balance between the loss of inelastic scattering due to the onset of magnetic order and the change in carrier concentration associated with the transition at T_0. Interestingly, the substitution of Ni for Fe appears to have minimal effect on inelastic scattering in the paramagnetic state, as indicated by the identical slope and curvature of all ρ(T) curves above T_0 in Fig. 5.4(a). This can be considered as a confirmation of the dominant role of phonon scattering in determining the temperature dependence of resistivity.

For $x = 0$, ρ continues to decrease below T_0 without any trace of superconductivity down to 1.8 K. The appearance of strain-induced superconductivity with $T_c =$

21 K wass found to appear in undoped and undoped (x = 0) samples (see refs. [1, 2], however the data presented here has had all traces of superconductivity removed by heat treatment. This is also the case for x =0.08, with no evidence of superconductivity down to 1.8 K. However, x =0.1 begins to show traces of superconductivity as evidenced by a partial drop in ρ(T) below ∼10 K as shown in Fig. 5.4(b). For x =0.12, there is a sharp drop below 8.4 K that does reach zero resistance at lower temperatures. This partial transition turns into a full transition for x ≥0.14 with higher T_c. In the range of samples studied, the highest T_c is obtained for x =0.18 with a ∼9.8 K onset and ∼9.6 K midpoint. For x ≥ 0.2, superconductivity becomes partial again with incomplete superconducting transitions shown in the x = 0.20 and x = 0.22 samples and the complete absence of any superconducting transition down to 1.8 K for x = 0.30.

Figure 5.5 presents the phase diagram representing the variation of T_0 (determined as noted above) and T_c (determined by the 50% drop of ρ) as a function of Ni content x. The superconducting window spans the range x =0.1-0.22 (see also Fig. 5.7(d) below for a detailed view) and forms a dome-like superconducting phase that appears qualitatively similar to other Co- and Ni-doped 122 compounds. The optimal concentration for Ni substitution (x = ∼ 0.15) is approximately half that for $SrFe_{2-x}Co_xAs_x$ (x ∼ 0.25), however the values are different enough to cast aspersions on the charge doping picture. The maximum T_c is also lower, differing from the case of TM subsitution in the $BaFe_2As_2$ case (see Fig. 6.2).

Figure 5.6(a) presents the temperature dependence of magnetic susceptibility χ of $SrFe_{2-x}Ni_xAs_2$ crystals, measured under zero-field-cooled (ZFC) conditions by

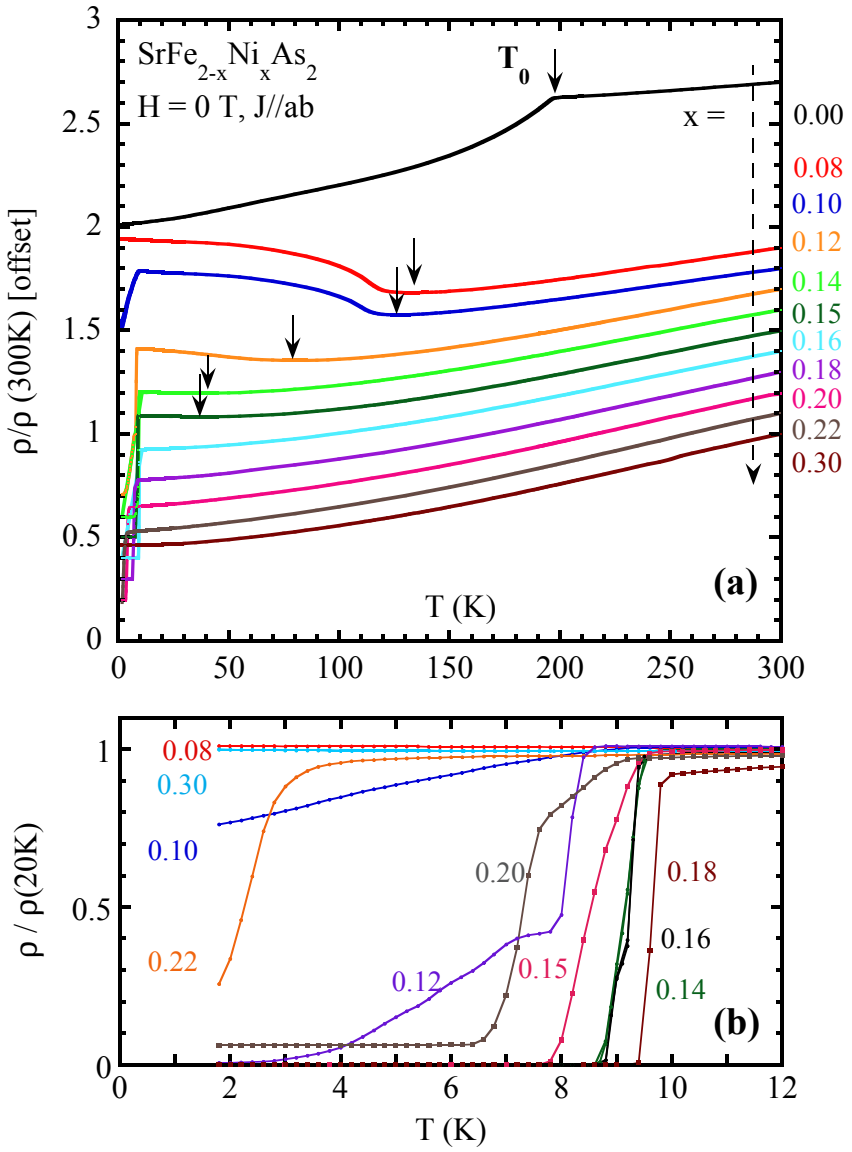

Figure 5.4: (a) Temperature dependence of in-plane electrical resistivity of specimens of $SrFe_{2-x}Ni_xAs_2$, normalized to 300 K and offset for clarity (data sets placed above x=0.30 are successively offset vertically by 0.1, except for x=0 data, which are offset by 1.7). The direction of the broken arrow indicates the order of the resistivity curves with ascending x as noted to the right. Short arrows indicate the position of the magnetic transition T_0, defined by the kink in x = 0 data and the minima in ρ(T) data for $0.08 \leq x \leq 0.15$. (b) Expanded lowtemperature view of resistivity normalized to 20 K for clarity, showing the evolution of superconducting transitions with Ni concentration. From Ref. [5].

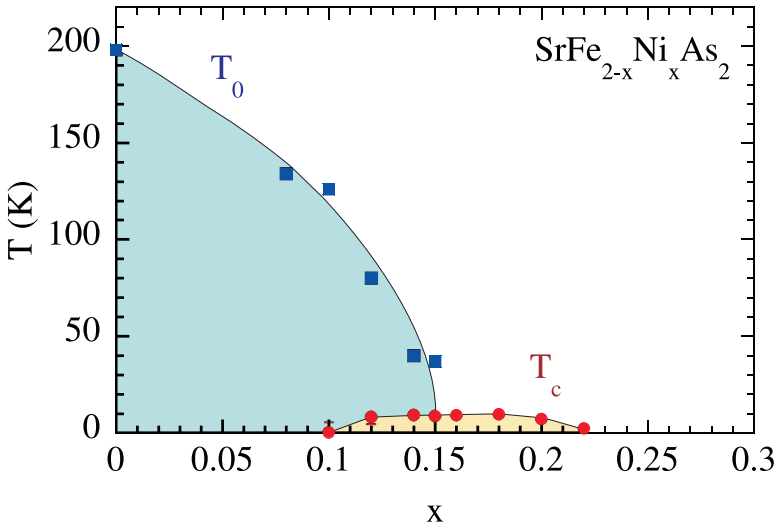

Figure 5.5: Ni substitution phase diagram of $SrFe_{2-x}Ni_xAs_2$ obtained from electrical resistivity data, showing the suppression of the magnetic/structural phase transition T_0 (blue squares) with increasing Ni concentration, and the appearance of a superconducting transition (red circles) with maximum T_c of $\sim$10 K centered around x = 0.15. From Ref. [5].

applying 10 mT along the ab-plane. The data are presented with a y-axis offset for clarity purposes (x=0 data have been shifted by +0.0015 cm^3/mol, and successive data sets for x > 0 have been staggered downward), however note that absolute values at room temperature for all Ni concentrations are all approximately χ(300 K) $\sim$ 0.001 cm^3/mol to within experimental error. As shown, the overall behavior of low-field susceptibility for x = 0 is similar to that reported previously [109] for high-field conditions, showing a modest temperature dependence interrupted by a sharp drop at T_0 due to the magnetic/structural transition. The overall temperature dependence and magnitude of χ remains more or less constant with Ni doping, indicating minimal impact of Ni substitution on the paramagnetic susceptibility of $SrFe_{2-x}Ni_xAs_2$. With increasing Ni concentration, the large step-like feature at T_0 is suppressed to lower temperatures and dramatically reduced in magnitude, as indicated by a small kink at T_0 for x = 0.08 and no discernible feature for higher x. This behavior is comparable to the effect of Co doping in the $BaFe_{2-x}Co_xAs_2$ series [42], which shows a similar trend in magnetization data taken at 1 T.

Note that the low-field χ(T) data presented here do not show any significant increase at low temperatures, indicating both good sample quality (i.e., minimal magnetic impurity content) and no indication of strain-induced superconductivity [1, 2]. A very small upturn in χ(T) does appears to onset at low temperatures in all Ni-doped samples. Although its magnitude is quite small, the systematic presence of this upturn along with its slight enhancement in higher Ni-doped samples (i.e., x=0.22 and 0.30 data sets) suggests the presence of either a small magnetic impurity content or a small local-moment contribution, possibly due to the presence of Ni.

Because a Curie-like tail was reported in $SrFe_2As_2$ samples even at high (5 T) fields, albeit with a much more pronounced increase at low temperatures [109], impurity contributions are less likely. In any case, more work is required to discern the origin of this feature.

Shown in Fig. 5.6(b) are the low temperature susceptibility data for $SrFe_{2-x}Ni_xAs_2$ samples measured with a smaller applied field of 1 mT along the ab-plane under both ZFC and field-cooled (FC) conditions, plotted as the volume susceptibility $4\pi\chi$ to compare the level of diamagnetic screening due to superconductivity. As shown, the superconducting volume fraction, as estimated by the fraction of full diamagnetic screening ($4\pi\chi$ = -1), varies with Ni concentration, being absent for x < 0.12, partial for x =0.12, 0.14, and 0.20, and complete for x =0.15, 16 and 0.18. This suggests that there is indeed a full superconducting volume fraction observed for a range of Ni concentrations with maximized T_c values, but also that partial volume fractions are evident at the fringes of the superconducting dome. For instance, note that a drop in χ(T) is visible below 7 K in the x = 0.08 data shown in Fig. 5.6(a), but also that the volume fraction associated with this diamagnetic screening is very small, being less than $\sim$ 1% as evident from Fig. 5.6(b). Likewise, data for x = 0.12 show a somewhat larger response but still remain at much less than 100%. This is quantified in Fig. 5.7 in comparison to other quantities of interest, as discussed below.

Fig. 5.7 summarizes the evolution of the superconducting state parameters in more detail as a function of Ni concentration. The evolution of ρ_0 with Ni doping is plotted in Fig. 5.7(a), including both the absolute value of ρ_0 (left y-axis) and that

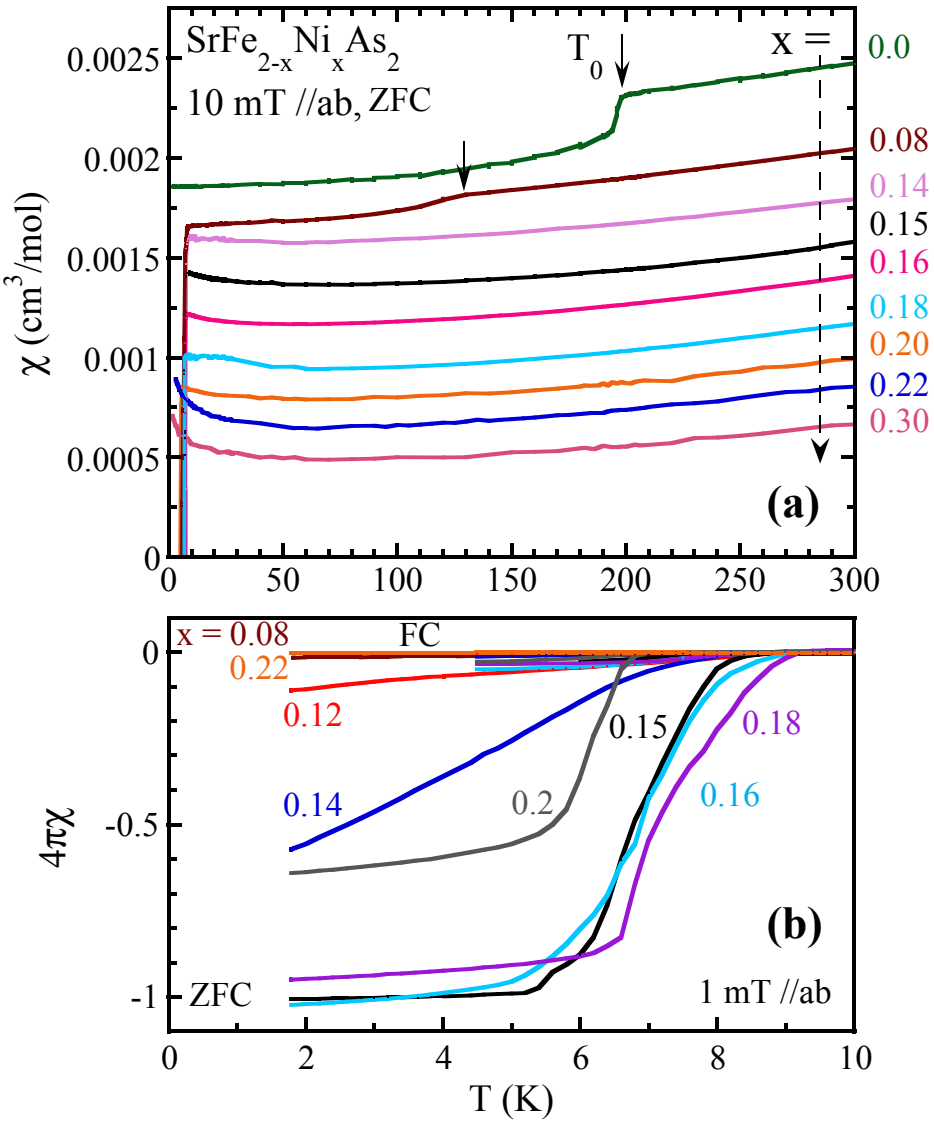

Figure 5.6: Temperature dependence of magnetic susceptibility χ of $SrFe_{2-x}Ni_xAs_2$, measured with 10 mT field applied parallel to the crystallographic basal plane from zero-field-cooled (ZFC) conditions, offset for clarity (x=0 data are vertically offset by +0.0015 cm^3/mol, with other sets offset successively downward by 0.0002 cm^3/mol). (b) Low-temperature zoom of the volume magnetic susceptibility in $SrFe_{2-x}Ni_xAs_2$ crystals under 1 mT ZFC and field-cooled (FC) conditions after a 24 hour / 700°C annealing treatment (see text for details). From Ref. [5].

normalized by $\rho(300\ \mathrm{K})$ (right y-axis) to remove uncertainty in geometric factors. As a function of x, both absolute and normalized values of $\rho_0(\mathrm{x})$ follow a similar pattern, suggesting that geometric factor errors are not large, as might have been expected.

Interestingly, aside from this enhancement, the impurity scattering level (as measured by the value of $\rho_0(\mathrm{x})$) does not show any significant change with Ni concentration, with values of ρ_0 in high Ni content samples approaching that of $\rho(\mathrm{x} = 0)$. In a minimal model where residual resistivity is dominated by impurity/disorder scattering, this trend would suggest that Ni substitution for Fe introduces minimal disorder into the system, even up to x = 0.30 levels. These are, however, 4 wire measurements and thus include the error in thickness measurements (see section 2.1.3, so calculations of the transport scattering rate as described in introductory chapters will have large errors. I cover the calculation of the scattering rate in more detail in chapter 6.

A detailed plot of T_c vs. x is presented in Fig. 5.7(d), showing good agreement between T_c values determined by transitions in $\rho(\mathrm{T})$ and $\chi(\mathrm{T})$. As is evident from the comparison of $\rho_0(\mathrm{x})$ to $\mathrm{T}_c(\mathrm{x})$ in Fig. 5.7, the rather abrupt decrease in residual scattering occurs very close to the appearance of bulk superconductivity in $SrFe_{2-x}Ni_xAs_2$. The Ni concentration of x = 0.14 is where ρ_0 drops to its low value and a sizeable volume fraction of superconductivity first appears, as shown in Fig. 5.7(b). Both the width $\Delta\mathrm{T}_c$ of the transition and the superconducting volume fraction change dramatically in this concentration range. As shown, there is an interesting inverse correlation between $\Delta\mathrm{T}_c$ and this volume fraction within the range

of superconducting samples, illustrating that the sharpest superconducting transitions are associated with bulk superconductivity, while the broader transitions are associated with only partial volume superconductivity. its low value and a sizeable volume fraction of superconductivity first appears, as shown in Fig. 5.7(b). Both the width ΔT_c of the transition and the superconducting volume fraction change dramatically in this concentration range. As shown, there is an interesting inverse correlation between ΔT_c and this volume fraction within the range of superconducting samples, illustrating that the sharpest superconducting transitions are associated with bulk superconductivity, while the broader transitions are associated with only partial volume superconductivity.

5.1.4 Upper Crifical Field

The suppression with applied magnetic field H of the resistive superconducting transition of $SrFe_{2-x}Ni_xAs_2$ is presented in Fig. 5.8 for under- (x = 0.12), optimally- (x = 0.16), and over-doped (x = 0.20) concentrations. The data are normalized to the normal-state resistance for clarity. As noted previously, the transition width is narrowest near optimal Ni concentrations and broader for under- and overdoped samples.

The superconducting upper critical field H_{c2}, with H applied parallel to the c-axis, is shown in Fig. 5.9 for concentrations across the superconducting range. Here, H_{c2} is defined where the R(T) data have half the normal state value (0.5 in Fig. 5.8). With the exception of some curvature at low field, which is also seen

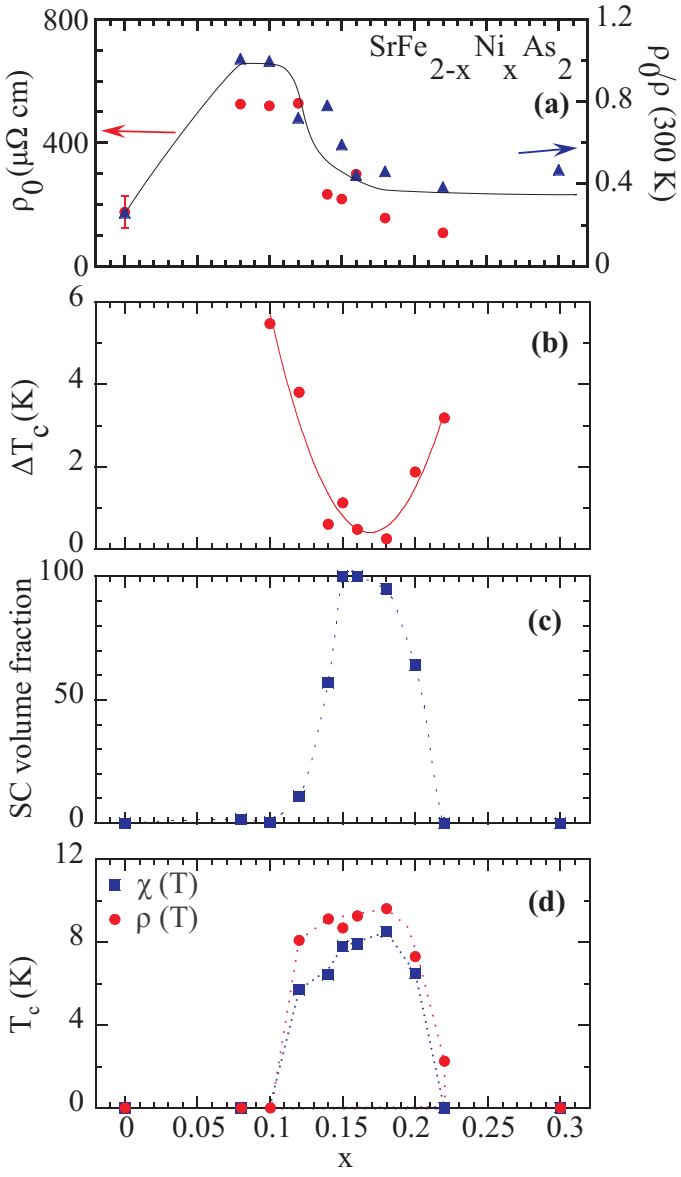

Figure 5.7: Evolution of normal and superconducting state parameters in $SrFe_{2-x}Ni_xAs_2$ with Ni concentration x: (a) absolute (circles-left scale) and normalized (triangles-right scale) residual resistivity; (b) variation of the width in temperature of the resistive superconducting transition ΔT_c . (c) superconducting volume fraction determined from the magnetic susceptibility data. (d) expanded view of the superconducting phase determined by transition temperatures defined by 50% resistivity drop (circles) and 10% value of total diamagnetic screening (blue squares). All lines are guides. From Ref. [5].

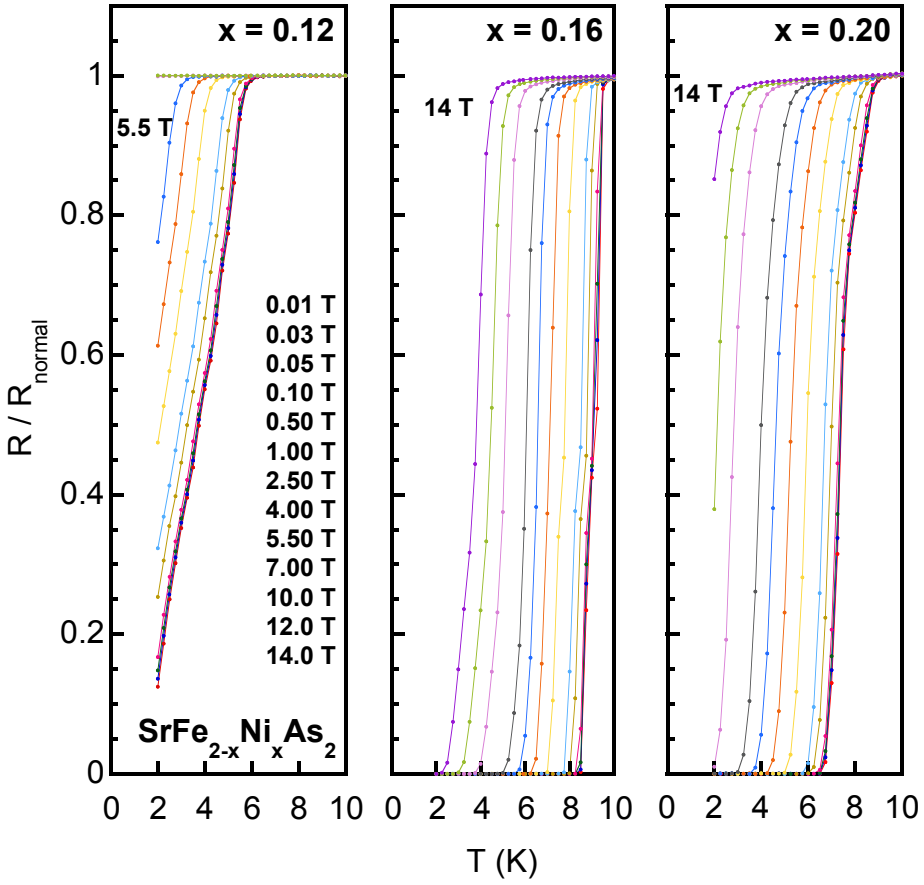

Figure 5.8: Electrical resistivity of $SrFe_{2-x}Ni_xAs_2$ vs temperature, showing the suppression of the superconducting transition by increasing magnetic field, applied parallel to the c-axis. The resistivity is normalized to the normal state value just above the transition. For x = 0.12, 7 T data are not shown. From Ref. [7].

in resistively determined values for other 122 superconductors [161, 42], the H_{c2}(T) curves are strikingly linear. The slope $\frac{\partial H_{c2}(T)}{\partial T}$ ranges from -1.8 T/K for x = 0.12 to a maximum value of -2.9 T/K for x = 0.16 at optimal doping, to -1.1 T/K for x = 0.22. These slopes are comparable to those reported for many other transition metal substituted systems (See Fig. 6 in Ref. [7].

The inset of Fig. 5.9 shows the H_{c2}(T) curves scaled with respect to T_{c0}, the value of T_c at H = 0, and the reduced field H* = -$\frac{H_{c2}}{T_{c0}}$ / $\frac{\partial H_{c2}}{\partial T}$, which is defined such that the slope $\frac{\partial H^*}{\partial T_c/T_{c0}}$ = -1 As shown in the inset of Fig. 5.9, the scaling procedure collapses all H_{c2}(T) data onto one curve, underscoring the already-noted similarity in H-dependence for all superconducting concentrations of $SrFe_{2-x}Ni_xAs_2$. However, this plot also makes it clear that the Werthamer-Helfland-Hohenberg (WHH) estimate that H*(T = 0) $\approx$ 0.7 is too low, because in $SrFe_{2-x}Ni_xAs_2$, T_c/T_{c0} = 0.3 at H^* = 0.7, where the WHH model predicts T_c should be 0 [162]. At this low reduced temperature, the scaled upper critical curve is still linear, and shows no signs of saturation. There are a few explanations for a superconductor exceeding the orbital (WHH) limit, as well as an ever increasing number of superconductors that exceed it, including two materials recently studied by our group: YPtBi [163] and Bi_2Se_3 under pressure (manuscript in progress). In addition, the weak-coupling estimate of the paramagnetic critical field (or the Pauli limiting field, $H_P = 1.84T_c$) yields values comparable to those determined by the WHH formula. In other words, both conventional estimates of the paramagnetic and orbital limiting fields underestimate the actual $H_{c2}(0)$. This characteristic has been noted in other iron pnictide superconductors and is discussed in a 2010 review article [164].

An extrapolation of the linear $H_{c2}(T)$ slope to T = 0 K yields a nominal limiting value of 25 T for x = 0.16. Actually, this extrapolation may be quite accurate, as an almost linear $H_{c2}(T)$ is observed for H ∥ c in Co- substituted $SrFe_2As_2$ thin films [165]. Superconducting coherence lengths $\xi = (\Phi_0/2\pi H_{c2})^{1/2}$, where Φ_0 is the flux quantum, range from about 10 nm to 3.5 nm for the range of $H_{c2}(0)$ values observed in $SrFe_{2-x}Ni_xAs_2$. For comparison, the value of ξ = 3 nm was determined for $BaFe_{1.8}Co_{0.2}As_2$ via scanning tunneling microscopy [166].

The $H_{c2}(T)$ curves were also studied with H applied perpendicular to the c-axis. In Fig. 5.10, a field-direction comparison is made for x = 0.12 and 0.16. As with all iron-based 122 superconductors, H applied perpendicular to the c-axis suppresses T_c less quickly in $SrFe_{2-x}Ni_xAs_2$. This is especially visible for x = 0.16, where there is increased curvature in $H_{c2}(T)$ relative to the H ∥ c case, which is again consistent with measurements on Co-substituted $SrFe_2As_2$ thin films[165], although due to the limited field and temperature range of the current measurements, it is unclear whether the $H_{c2}(T)$ curves extrapolate to the same value of H. The anisotropy, H_{c2}^{ab}/H_{c2}^{c} is plotted in the inset of Fig. 5.10. The anisotropy in x = 0.12 is roughly constant at a value of about 2.2, whereas the anisotropy in x = 0.16 varies from approximately 2.5 near T_c to 1.5 at 0.5 T_c. This range of anisotropy values is consistent with both electron- [42, 167] and hole-doped 122 materials [45, 168, 169]. Considering the range of values of T_c exhibited by these superconductors, the similarity is again noteworthy.

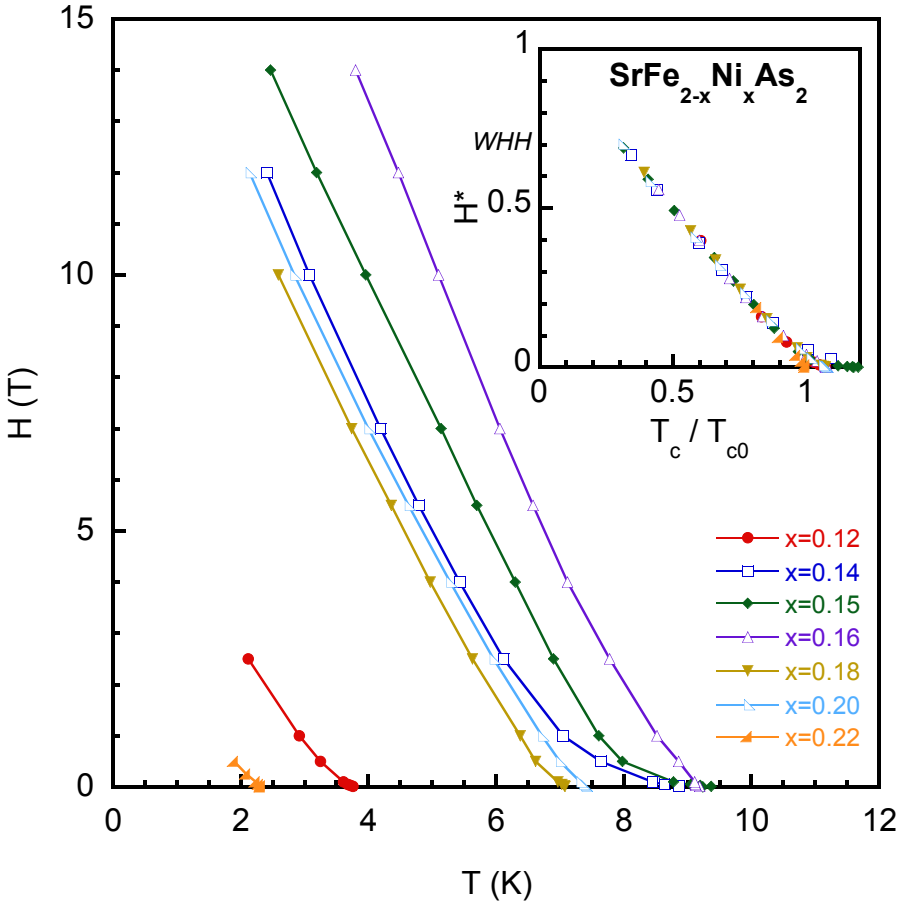

Figure 5.9: Upper critical field H_{c2} of $SrFe_{2-x}Ni_xAs_2$, for H // c, vs temperature. The points here denote the 50% point in the resistive transition. Inset: H_{c2} curves scaled to the zero field transition temperature T_{c0} and a slope of -1. The value of H_{c2} at T = 0 K exceeds the WHH estimate. From Ref. [7].

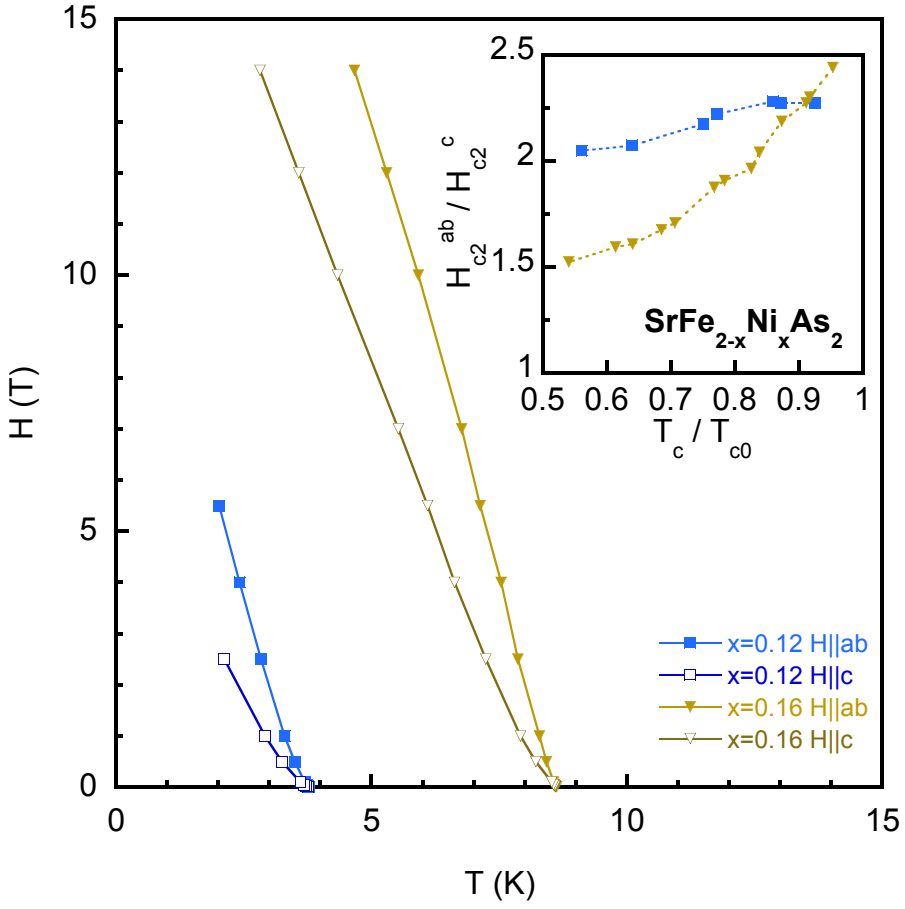

Figure 5.10: Upper critical field H_{c2} of $SrFe_{2-x}Ni_xAs_2$, determined via resistivity, for different field orientations. Inset: Anisotropy of H_{c2}, which shows stronger temperature dependence at optimal doping. From Ref. [7].

5.1.5 Hall Effect and Carrier Concentration

We now consider the effect that transition metal substitution has on the carrier concentration in 122 systems. We expect that Ni substitution should act as electron doping, and that the effect should be twice that of Co doping as it does in the case of Co- and Ni-subsitution in $BaFe_2As_2$[82]. A comparison of the temperature T dependence of the Hall constant R_H for $SrFe_{2-x}Ni_xAs_2$ is shown in Fig. 5.11. R_H has measured as described in chapter 2 using the 4 wire transverse contact configuration. As shown in the inset of Fig. 5.11, the ρ_{xy}(H) data are linear with a negative slope in H $<$ 5 T, indicating the existence of a dominant electron-like signal, so to calculate the carrier concentration we can use the one-band (Drude) approximation $R_H = (ne)^{-1}$. I discuss the validity of this assumption in more detail in the following chapter. For all Ni concentrations, these values of R_H at room temperature correspond to a density of carriers of about 10^{22} cm^{-3} in a one-band model. For x = 0 and x = 0.08, a change in carrier concentration coincides with the magneto-stuctural transition, yielding a low-T carrier concentration of 10^{21} cm^{-3}. For higher x, R_H is remarkably T -independent, although the superconducting transition is readily discernable. A clear trend towards lower or higher carrier number with Ni substitution can not be identified in these data. The uncertainty in the measurements is estimated at $\pm 0.2 \times 10^{-9}$ m^3/C (owing to measurements of the sample thickness), potentially masking any real x-dependence in the data. In contrast, in the case of $BaFe_{2-x}Co_xAs_2$, such a trend is evident, with the variation in $R_H \geq 1 \times 10^{-9}$ m^3/C as a function of Co concentration [22, 170]. While more precise Hall

measurements are required to reach a conclusion about the actual variation in R_H for $SrFe_{2-x}Ni_xAs_2$, it seems clear that the magnitude is significantly smaller than that observed for the $BaFe_{2-x}Co_xAs_2$ system. This may be related to the lower scattering rate observed in $BaFe_{2-x}Co_xAs_2$ (see chapter 6 and ref. [9] for further discussion of the scattering rate). For $SrFe_2As_2$, the low-T value of R_H determined in this study is slightly greater than half of a previously published value, -13 $\times$ 10^{-9} m^3/C [109], and significantly less than -25 10^{-9} m^3/C found for $BaFe_2As_2$ [22, 170, 21] although the complex Fermi surface of these materials makes it difficult to make any direct comparisons of carrier density between Ba and Sr materials, and the multiband nature of the undoped materials makes such an analysis suspect. These results are also consistent with ARPES results showing that there is a dominant electron Fermi surface in Co-substituted $BaFe_2As_2$ [171, 172].

5.2 $SrFe_{2-x}Pt_xAs2$ and Comparison to $SrFe_{2-x}Ni_xAs2$

Following the Ni substitution study, single crystals of Pt substituted $SrFe_2As_2$ were grown using a similar method to the one described above for Ni substitution with two exceptions. First, it was found that annealing crystals did not seem to have a large effect on the transition temperature, so the data reported here is for unannealed crystals. Second, while the Pt content within each single crystal specimen was found to be uniform, a dispersion of Pt content was found within some of the batches. Because of this, for each sample used for measurements presented in this work the platinum content of single-crystal samples was measured using WDS,

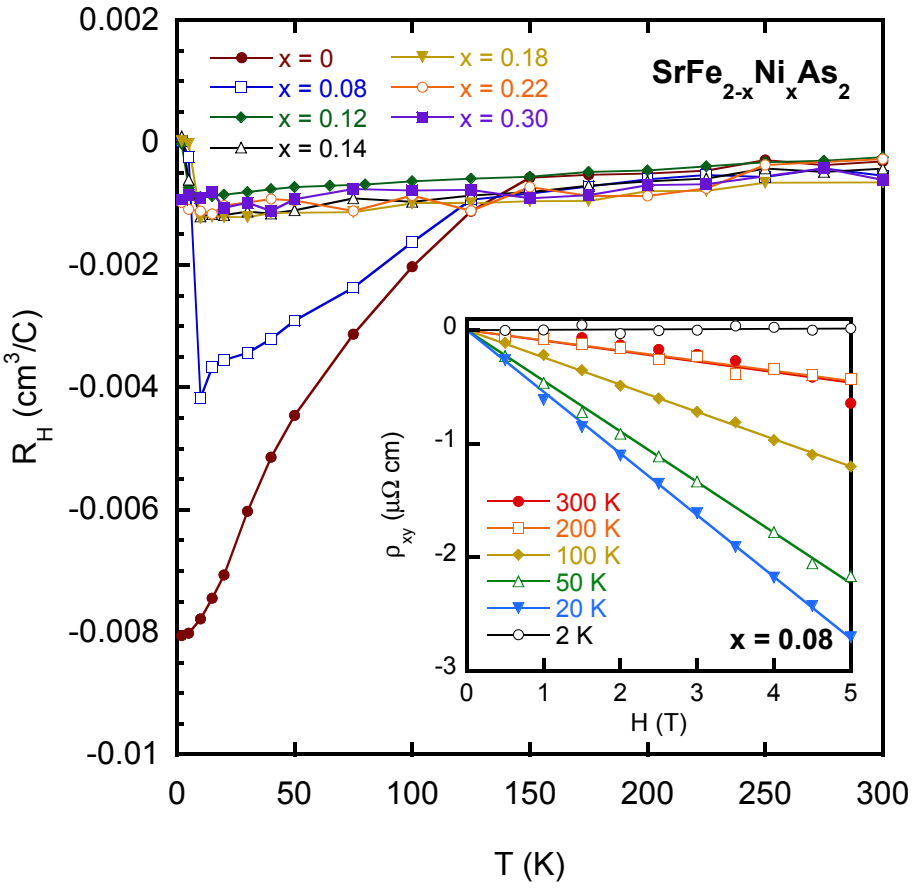

Figure 5.11: Hall coefficient of $SrFe_{2-x}Ni_xAs_2$ as a function of temperature. The magnetic transitions in x = 0 and x = 0.08 are evident as a drop in R_H. Superconducting transitions are evident for $0.08 \leq x \leq 0.22$ at low temperatures. All measurements are consistent with a dominant contribution from negative charge carriers. The error bar on the right illustrates the window of uncertainty of about $\pm 0.210^{-9}$ m^3/C. Inset: Field dependence of the transverse resistivity is linear to at least 5 T. From Ref. [7].

with analysis performed at several points along each crystal with spot sizes ~ 1 μm^2 to determine the chemical composition, rather than the more common practice that was used in the Ni substitution study of analyzing a few crystals from each nominal stoichiometry and using the representative value for all samples from the batch. The results of the WDS analysis reveal a slight gap in the range of Pt concentrations, approximately between $0.18 \leq x \leq 0.26$, despite repeated attempts at crystal growth targeted for this range.

Single crystal x-ray diffraction was used to obtain the c-axis lattice parameters for crystalline samples across the series. As shown in Fig. 5.12, the unit cell contracts in the c-axis direction in this system as it does for other transition metal substitutions in the $SrFe_2As_2$ system[5, 16, 173, 15]. Notably, the progression of the c-axis lattice parameter follows almost exactly that of the Ni-doped series $SrFe_{2-x}Ni_xAs_2$ within error. Since Pt and Ni have different covalent radii (1.36 Å for Pt and 1.24 Å for Ni) its surprising that within the experimental accuracy the absolute values of lattice size in the Pt system approximate those seen in the Ni system, decreasing to 12.25 Å for $x = 0.28$ (see Fig. 5.12). This is suggestive of the minimal effect of the nature of substituent atoms on the unit cell evolution, likely dominated by modifications to the electronic structure of the FeAs layers at these lower concentration levels.

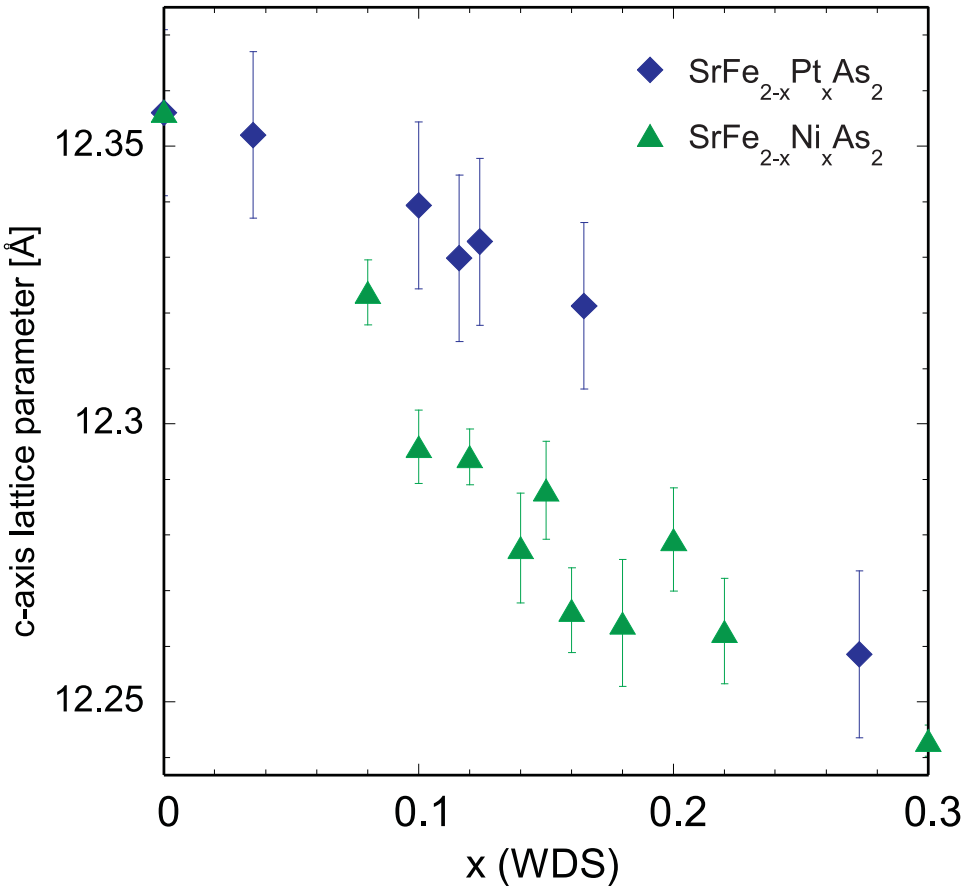

Figure 5.12: Variation of the c-axis lattice parameters with Pt concentration in single-crystal samples of $SrFe_{2-x}Pt_xAs_2$ compared with that from powder data of $SrFe_{2-x}Ni_xAs_2$. The c-axis length contracts with increasing Pt content, consistent with previous chemical substitution studies. Error bars were obtained by finding the lattice constant at the positions of the half maximum points on the x-ray diffraction peaks for each sample. From Ref. [8].

5.2.1 Resistivity and Magnetic Susceptibility

Fig. 5.13 presents the temperature dependence of electrical resistivity, ρ(T), in $SrFe_{2-x}Pt_xAs_2$ normalized to the room temperature value in the upper panel of the figure as well as the derivative of this normalized resistivity, -d(ρ(T)/ρ(300 K))/dT, in the lower panel. This choice of normalization is done to remove the error contribution coming from the geometric factor due to unobservable internal cracks or exfoliation, with data in Fig. 5.13 shifted vertically for clarity. At high temperatures, the resistivity is fairly linear in temperature and with the same slope for all concentrations of Pt, indicating that the scattering at high temperatures has very little electronic dependence and is likely dominated by phonons or some other mechanism that is independent of Pt substitution. Note that this is very similar to the case of Ni substitution as seen above.

In the parent compound $SrFe_2As_2$, an onset of antiferromagnetic order at T_N as well as a change from tetragonal to orthorhombic crystal structure at T_0 both occur at a characteristic temperature of 200 K, which manifests itself as a sharp drop in the resistivity upon decreasing temperature. With substitution of as little as 2.0% Pt in place of Fe, this drop through the transition transforms into an upturn below T_0 as in the case of Ni substitution. The evolution of the character of the transition in resistivity, from downturn to upturn, can be explained in terms of a shift in the balance between the loss of inelastic (magnetic) scattering due to the onset of magnetic order and the change in carrier concentration associated with the transition at T_0, as observed in several other FeAs-based systems [5]. Upon further

Pt substitution, the transition then appears as a broader minimum in the resistivity which becomes less discernible as a sharp feature[19].

The position of T_0, marked by arrows in part (a) of Fig. 5.13, is identified with the onset of the sharp drop for $x \leq 0.035$, and the position of the minimum in resistivity for $x \geq 0.09$. In the related system $BaFe_{2-x}Co_xAs_2$, the magnetic and structural transitions that occur simultaneously at 200 K in the parent compound has been shown to split into two separate transition temperatures upon Co doping[44]. As was done in refs. [44] and [148], we examine the derivative of resistivity, $d\rho/dT$, in order to identify the splitting of the structural (T_0) and magnetic (T_N) transitions upon Pt substitution. Shown in Fig. 5.13(b), $-d\rho/dT$ indeed exhibits a peak whose transition temperature value differs from the minimum in $\rho(T)$ used to identify T_0 for $x \geq 0.09$. Given the resolution of our data, we are unable to resolve two distinct features in the derivative plot as done in the study by Chu et al. [44], and therefore define T_N at the position of the maximum in $-d\rho/dT$ as indicated by arrows in Fig. 5.13(b). A similar technique was used in references [19] and [82] to define the magnetic and structural transition temperatures for Rh and Pd substituted $BaFe_2As_2$. Note also that this is in contrast with the $SrFe_{2-x}Ni_xAs_2$ study in which this splitting is not observed.

The peak widths are used to define the uncertainty in T_N values associated with this assignment (see phase diagram in Fig. 6 of reference [8] or Fig. 5.15 below). At $x = 0.09$, superconductivity becomes visible in the resistivity, where it coexists with the magnetically ordered phase. With further substitution the magnetism is gradually suppressed and vanishes near $x = 0.16$ (hereafter called optimal doping),

where the maximum T_c of 16 K is observed. Here we see another similarity with the Ni substituted system: optimal T_c for both systems occurs at approximately x = 0.16. For x = 0.36 both magnetic order and superconductivity are suppressed and normal metallic behavior appears to be recovered.

The bulk nature of the superconducting transition is indicated through the observation of Meissner screening in low-field magnetic susceptibility measurements. Because of the small size of available samples, normalized data is presented in order to provide for a more useful comparison. Fig. 5.14 presents the temperature dependence of the change in susceptibility from the normal state at 20 K normalized to the value at 2 K, $\Delta\chi(T)/\chi(2\text{ K})$ where $\Delta\chi = \chi(20\text{ K})\text{-}\chi(T)$. Data were measured in a magnetic field of 1 mT applied parallel to the ab-plane both in zero field cooled (ZFC) and field cooled (FC) conditions. In the ZFC measurement the samples were initially cooled down to 1.8 K in zero magnetic field and then 1 mT DC magnetic field was applied. The saturation of magnetic susceptibility indicates full Meissner screening and hence a nearly full superconducting volume fraction. The difference between FC and ZFC curves is due to trapped flux remaining in the sample as it is cooled through the superconducting transition in field.

As shown, the optimal doped sample x = 0.16 shows the sharpest and highest T_c, consistent with the specific heat and resistivity data, while the major drop in $\Delta\chi$ is suppressed in temperature for lower Pt concentrations. It is apparent that the x = 0.09 data shows two transitions, including a mild drop in $\Delta\chi$ at 15.5 K and a much sharper drop at 8 K, indicating a sample with mixed phase. This is likely due to the inclusion of a crystallite with higher Pt concentration in the

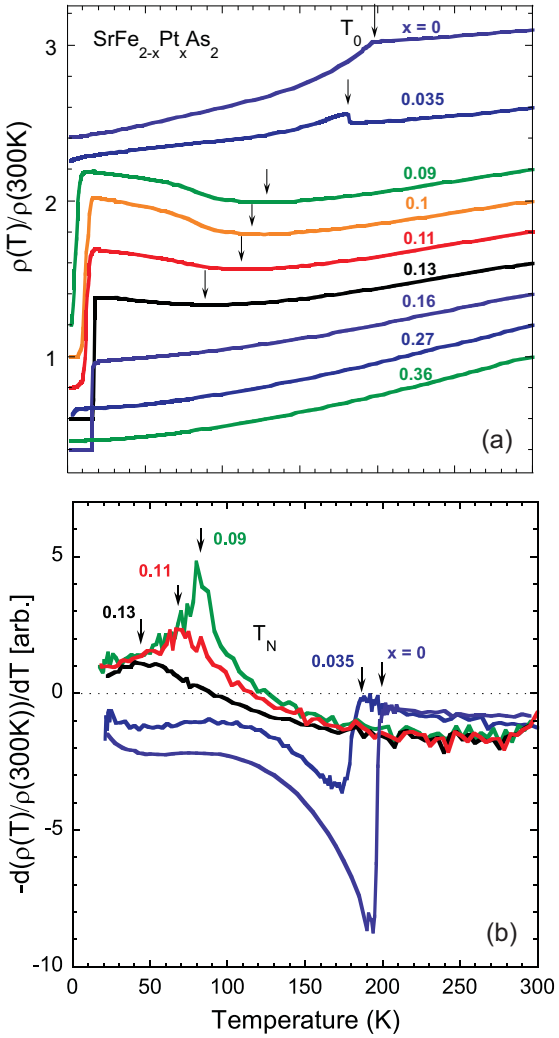

Figure 5.13: (a): electrical resistivity of single-crystal samples of $SrFe_{2-x}Pt_xAs_2$ normalized to 300 K (data are shifted vertically for clarity for all concentrations except x = 0.36). The structural transition T_0, identified by the local mimina in ρ(T), is suppressed with increasing Pt substitution, as indicated by the arrows. (b): negative of the temperature derivative of the normalized resistivity data for characteristic samples from part (a). The antiferromagnetic transition T_N is identified at the local maxima, while the dashed line indicates the zero crossing of -dρ/dT corresponding to local minima in ρ(T). At optimal doping, x = 0.16, T_0 and T_N are no longer discernible and the maximum T_c for the system is found to be 16 K. Neither magnetic order nor superconductivity is observable at x = 0.36, the highest concentration sample measured in this study. From Ref. [8].

collection of several small pieces required to increase signal to noise to a measurable level. No magnetic transition was observed in $SrFe_{1.84}Pt_{0.16}As_2$ in the normal state above T_c (not shown), consistent with the absence of a signature of the transition in resistivity data. The full volume fraction observed is similar to that seen in the Ni substituted system above, with superconductivity first appearing at a slightly lower concentration in the Pt system.

Using the results of the resistivity measurements we directly compare the phase diagrams of the $SrFe_{2-x}Ni_xAs_2$ and $SrFe_{2-x}Pt_xAs_2$ systems in Fig. 5.15. As shown, the antiferromagnetic order transition T_N follows an almost identical decline as a function of either Pt or Ni substitution, with minimal difference between the two systems. The similar positioning of the superconducting dome for each system at an optimal concentration of x $\sim$ 0.16 follows that expected for the nominally equivalent addition of two d-electrons from both Pt and Ni substituents, as compared to that of $SrFe_{2-x}Co_xAs_2$ with only one d-electron contribution and a significantly larger optimal doping of x $\sim$ 0.24 [174]. Though generally referred to as a superconducting "dome", the shape of the superconducting region of the phase diagrams for $SrFe_{2-x}Pt_xAs_2$ and $SrFe_{2-x}Ni_xAs_2$ are more step-like on the underdoped side than they are dome-like. In the case of $SrFe_{2-x}Pt_xAs_2$, T_c is already close to the maximum value of 16 K at the lowest Pt concentration where superconductivity is observed (x = 0.08). There is, however, a significant difference in the values of T_c(max), with T_c almost double in the Pt substituted system. Additionally, the superconducting dome is wider, i.e., the concentration at which superconductivity is first observed is lower in the Pt substituted system than in the Ni system, and

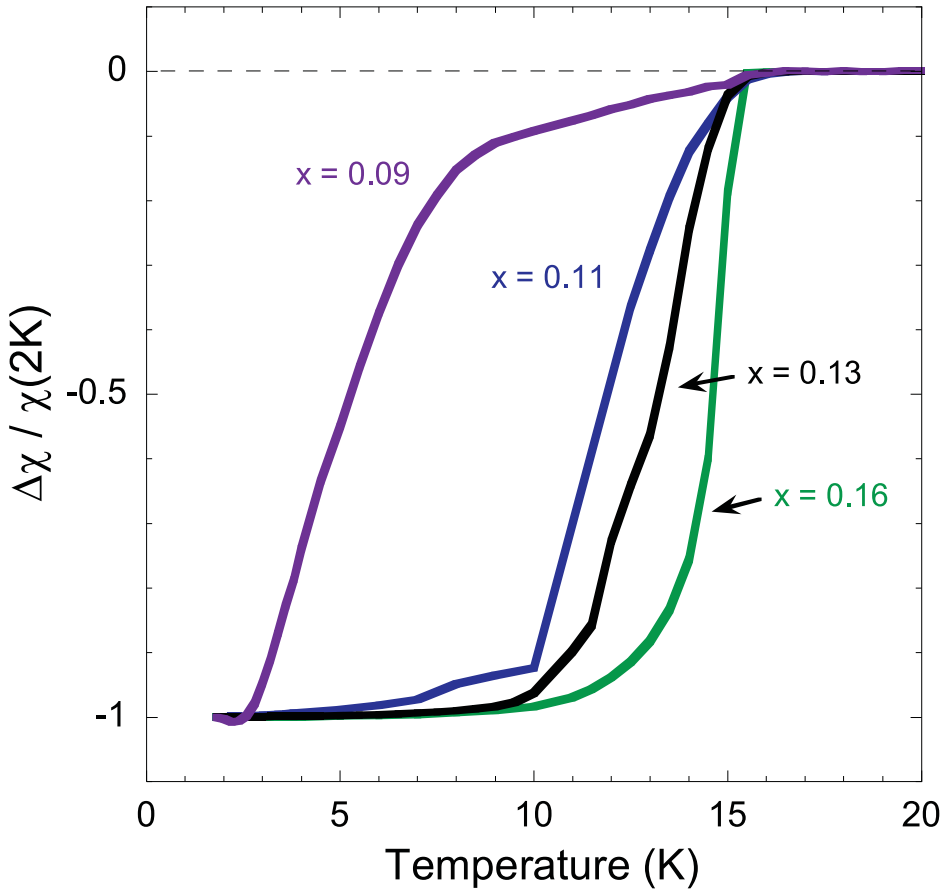

Figure 5.14: Change in magnetic susceptibility ($\Delta\chi \equiv \chi(20\text{ K}) - \chi(\text{T})$) of $SrFe_{2-x}Pt_xAs_2$ normalized to the susceptibility value at 2 K. Samples were measured in 1 mT field applied parallel to the crystallographic basal plane for zero-field-cooled (ZFC) conditions. From Ref. [8].

the concentration at which superconductivity disappears is higher, presenting an intriguing contrast in two systems with nominally identical suppression of magnetic order.

5.2.2 Upper Critical Field

Fig. 5.16 presents the evolution of the superconducting transition in resistivity for the optimal doping x = 0.16 in a magnetic field H. With the increase of H there is a slight broadening of the transition, with the narrowest transition width of $\sim$ 0.5 K for H=0 increasing to the broadest width of $\sim$ 2.5 K at H=14 T. The inset of Fig. 5.16 shows the temperature dependence of the superconducting upper critical field H_{c2}, along with data for optimally doped $SrFe_{2-x}Ni_xAs_2$ for comparison. (The value of H_{c2} is defined by the field where resistivity drops to 50% of the normal state resistivity.) Using the Werthamer-Helfand-Hohenberg (WHH) formula [162], $H_{c2}(0)$ is calculated to be 34 T for $SrFe_{1.84}Pt_{0.16}As_2$. While this is much higher than that found in the Ni system, the value of the slope dH_{c2}/dT near T_c for Pt of -3.16 T/K, is comparable to that of several other transition metals substitutions in the 122 systems[7], indicating a similar nature of the $H_{c2}(T)$ transition in all of these systems. If these curves are scaled by T_c as well as the slope dH_{c2}/dT near T_c (H^*, see section 5.1.4) we can see that they would lie on top of one another.

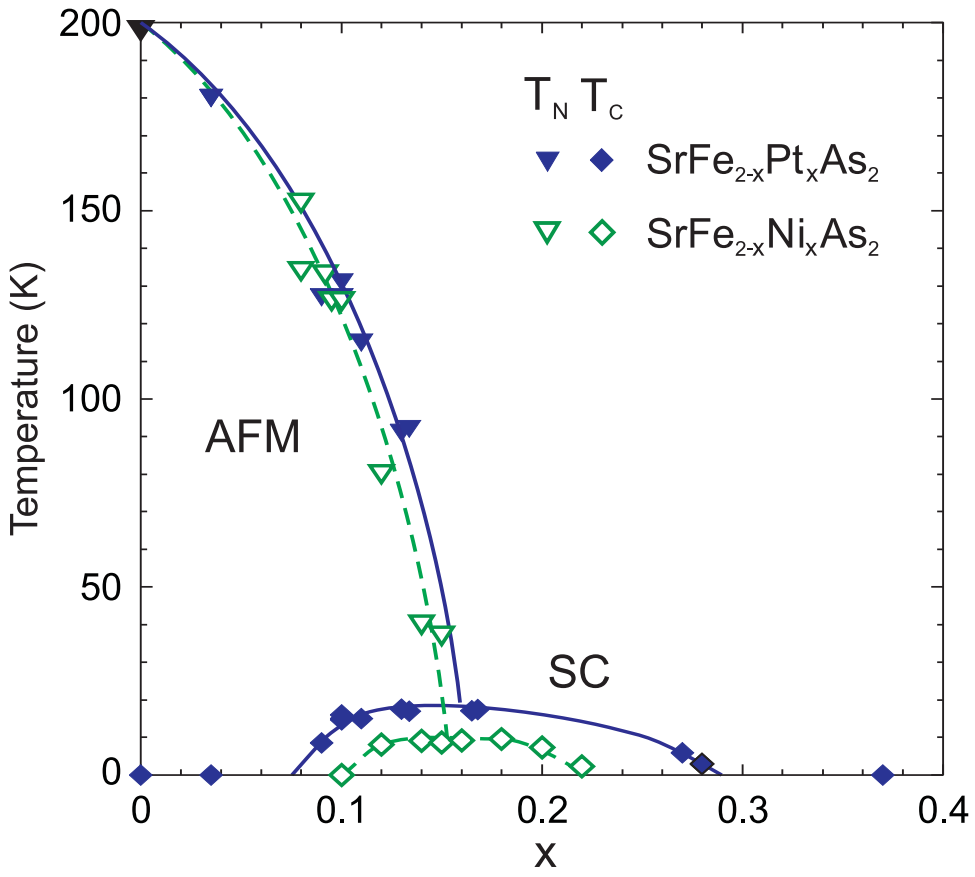

Figure 5.15: Phase diagrams of the $SrFe_{2-x}Ni_xAs_2$ and $SrFe_{2-x}Pt_xAs_2$ systems. Antiferromagnetic (triangles) and superconducting (diamonds) transition temperatures are plotted for Ni- (open symbols) and Pt-doped (closed symbols) systems. The similar rate of suppression of the magnetic phases and the position of the superconducting domes, with optimal doping at x $\simeq$ 0.16 for both cases, is to be contrasted with the considerably different T_c(max) values of 9 K and 16 K for Ni- and Pt-doped series, respectively. From Ref. [9].

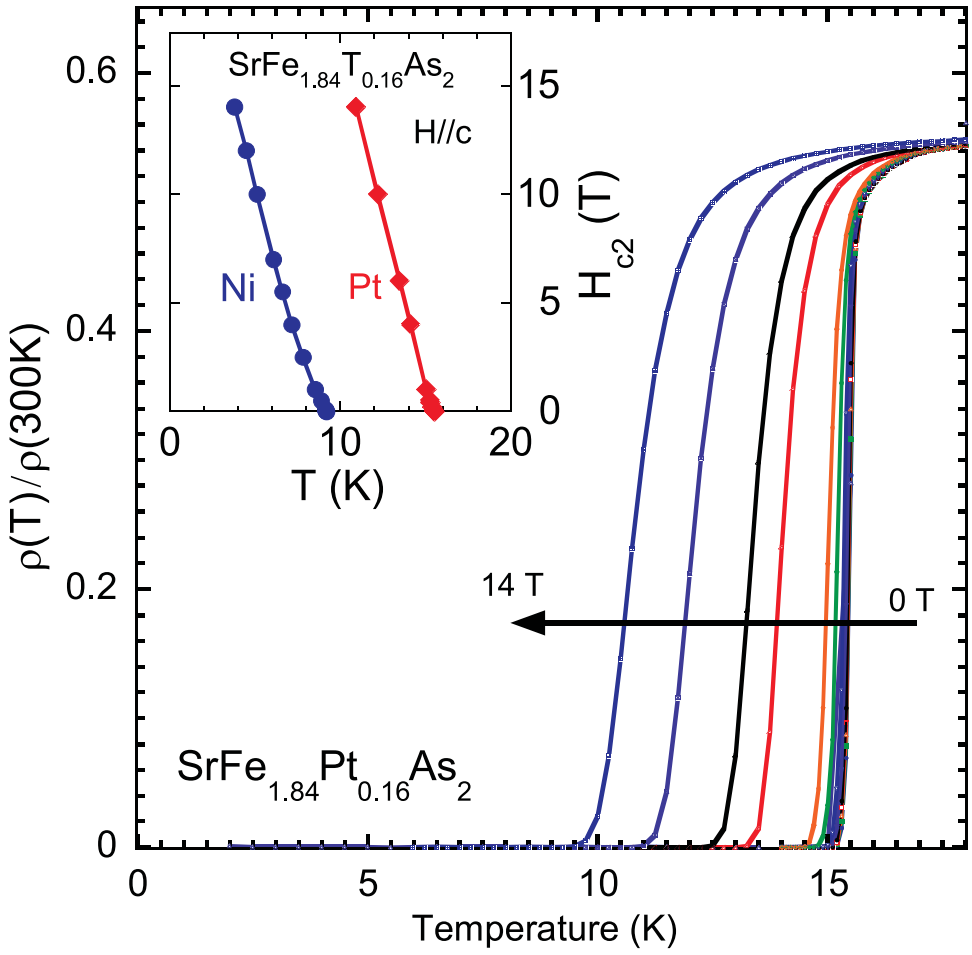

Figure 5.16: Magnetic field suppression of the resistive superconducting transition in optimally doped $SrFe_{1.84}Pt_{0.16}As_2$ for fields up to 14 T applied parallel to the c-axis. The resistivity is normalized to the room temperature value. Inset: superconducting upper critical field H_{c2}(T), defined at the 50% point of the normal state resistivity for each field in the main panel, plotted with that in $SrFe_{2-x}Ni_xAs_2$. From Ref. [8].

5.3 Comparison and Conclusions

In this chapter we measured the transport and magnetic properties of single crystals of Ni and Pt substituted $SrFe_2As_2$. Ni and Pt belong to the same periodic group, and so were expected to act similarly upon substitution as Ni and Pd do. We found that this is generally correct: the crystal structures of the two systems are similar, with approximately the same change in lattice structure with substitution. This would imply that any changes to the phase diagram would be due to electronic rather than structural changes. Additionally, both Ni- and Pt substituted systems have very similar resistivity curves that are linear at high temperature and do not change with substitution. The nature of the magnetic/structural transition is also similar with the downturn at T_0 in the parent compound becoming a peak and eventually a broad upturn with substitution. From this we can conclude that transition metal substitution has very little effect on the phonon contribution to the resistivity. Finally, some aspects of the superconducting phase are similar. The rate of suppression of magnetic ordering is approximately the same in both systems, with optimal concentration at $x \simeq 0.16$, as it is in $SrFe_{2-x}Pd_xAs_2$, and a little more than half that seen in Co- or Rh- substitution which show optimal concentration between 0.25 and 0.30 [16, 15] (see figures 6.1 and 6.2 for direct comparison of the superconducting phase in these systems). The upper critical field, when normalized to T_c and the slope of H_{c2} at T_c shows remarkably similar features to all transition metal substituted systems, indicating that the superconducting state is the same for all of these.

There are a few differences, however, that cannot be explained away simply. First, the crystal growth conditions between the two materials is quite different. It is more difficult to grow crystals in the Pt substituted system and it seems to have an imiscibility region in the slightly overdoped region of the phase diagram. The Ni substituted system seems to have more inherent disorder; crystals need to be annealed before the optimal T_c can be observed. This may be a function of substituent disorder, however I will show in the next chapter that the Ni system has a shigher scattering rate, a measure of disorder in a system. Additionally, the superconducting dome in the Pt-subsituted system is higher and wider than in the Ni doped system. If Ni and Pt were simply adding two electrons then this is completely unexpected. These differences are seen in the TM substituted $BaFe_2As_2$ system as well, though the effects are far more drastic in the $SrFe_2As_2$ based compounds. The dome in Pt-substituted $BaFe_2As_2$ is wider than the Ni- and Pd-substituted systems with a higher optimal T_c [17, 18, 19].

Future studies can help determine what precisely are the microscopic effects of chemical substitution on these systems. Crystals in Pt-substituted systems should be systematically annealed to determine more accurately whether there is any effect of annealing on the crystal structure. As in Chapter 3, single crystal x-ray diffractometry can be used to determine mosaicity of single crystals. As we will see in the next chapter, disorder may be a contributing factor to the superconducting transition temperature, and x-ray diffractometry can be one measure of the disorder.

With similar crystal structures, it now appears clear that there is a difference between Ni and Pt substitution which may arise from differences in electronic

scattering between these two systems. The Ni system appears to be more sensitive to disorder which may account for the lower transition temperature. In the next chapter I will continue to compare transition metal substituted 122s and attempt to explain the varying superconducting transition temperatures.

Chapter 6

Pair Breaking in Transition Metal Substituted 122s

Portions of this chapter have been summarized or paraphrased from the following published works:

Kevin Kirshenbaum, Shanta R. Saha, Steven Ziemak, Tyler Drye, and Johnpierre Paglione **Universal pair-breaking in transition metal-substituted iron-pnictide superconductors**. Physical Review B **86**, 140505 (2012) (Ref. [9])

As was explained in the introductory chapters, determining the symmetry of the superconducting order parameter is an ongoing problem in iron-based superconductor research [37, 36, 40]. The structure of the Fermi surface has been measured accurately and is given by two or three hole pockets centered around the Γ point ($k_x = 0$, $k_y = 0$) and two electron pockets centered around the M-point ($k_x = \pi$, $k_y = \pi$). The pairing symmetry, however, has been difficult to determine precisely. The leading model is a multiband s-wave order parameter that changes sign across the bands, called $s_\pm$ [54, 55, 57], although there are other models that have not been ruled out including d-wave [55] and a multiband s-wave structure that does

not change sign [65, 60]. These two s-wave models would be very difficult to distinguish by most measurements; both models can have fully gapped Fermi surfaces or "accidental" nodes that follow the same symmetry as the underlying crystal. Typically one needs to use a phase-sensisitive measurement, however these have proven to be experimentally challenging and as such there have not yet been any conclusive results from a phase sensitive experiment.

Another way to determine which of these models is correct would be to examine what happens to the transition temperature as a function of disorder. As explained in section 2.6, measurements of the scattering rate can be used to determine if there is substantial pair breaking which can then be used to infer information about the pairing symmetry. There have been previous studies of pair breaking in iron-based superconductors that have used extrinsic methods to increase scattering. Irradiation with heavy ions [175, 27], protons [176], or neutrons [26] can be used to induce point defects in crystals and increase scattering. The problem with this method is that the defects may be anywhere in the crystal, and so can be disrupting the superconducting Fe-As layer or the alkaline earth layer, and the effects from these may be drastically different. A more controlled way to induce defects is to substitute another element in place of iron [96], often with zinc, which is considered to be a nonmagnetic inpurity [177], although that assumption is often questioned as the magnetic suscptibility seems to increase with Zn substitution [178, 179]. Some of these studies have shown a rapid suppression of T_c with scattering while others have shown little change. With superconductivity induced by substuting almost any of the TM elements in the Fe, Co, and Ni columns, the robustness of these

superconductors to disorder - in particular, disorder focused directly in the Fe-As layer which is believed to be the active pairing layer - provides a striking constrast to the sensitivity found in other unconventional superconductors like the cuprates. Furthermore, this robustness initiated one of the early challenges to the proposed $s_{\pm}$ sign-changing gap symmetry , and has been touted as evidence for a non-sign-changing s-wave pairing symmetry [65, 60]. The rate of suppression of T_c with scattering can be used not only to distinguish between s_{++}, $s_{\pm}$, and d-wave pairing symmetries [100], but can potentially be used to determine more nuanced information about the inter- and intraband coupling in 122s [99].

The motivation for this study was to determine why TM substituted 122s have different transition temperatures. This began with my comparison of Ni and Pt substitution in $SrFe_2As_2$, however I soon realized that these differences are more common than was previously reported. The maximum or "optimal" transition temperature $T_{c(max)}$ for different TM-substituted versions of the $SrFe_2As_2$ system exhibits a wide variation of values, reaching approx. 20 K for Co, Rh and Ir [15, 16], 16 K for Pt [8], 9 K for Ni [5] and 8 K for Pd substitution [16]. This is seen to a lesser degree in the $BaFe_2As_2$ family as well, with Pt, Co, and Rh substitution having slightly higher transition temperatures than the Ni and Pd system [17, 18, 19]. I directly compare the phase diagrams of the TM substituted $SrFe_2As_2$ and $BaFe_2As_2$ systems in figures 6.1 and 6.2.

If we look closely at the comparison of Ni- and Pt- substitution (Fig. 5.15, we see that the antiferromagnetic order transition temperature T_N follows an almost identical decline as a function of either Pt or Ni substitution, with minimal difference

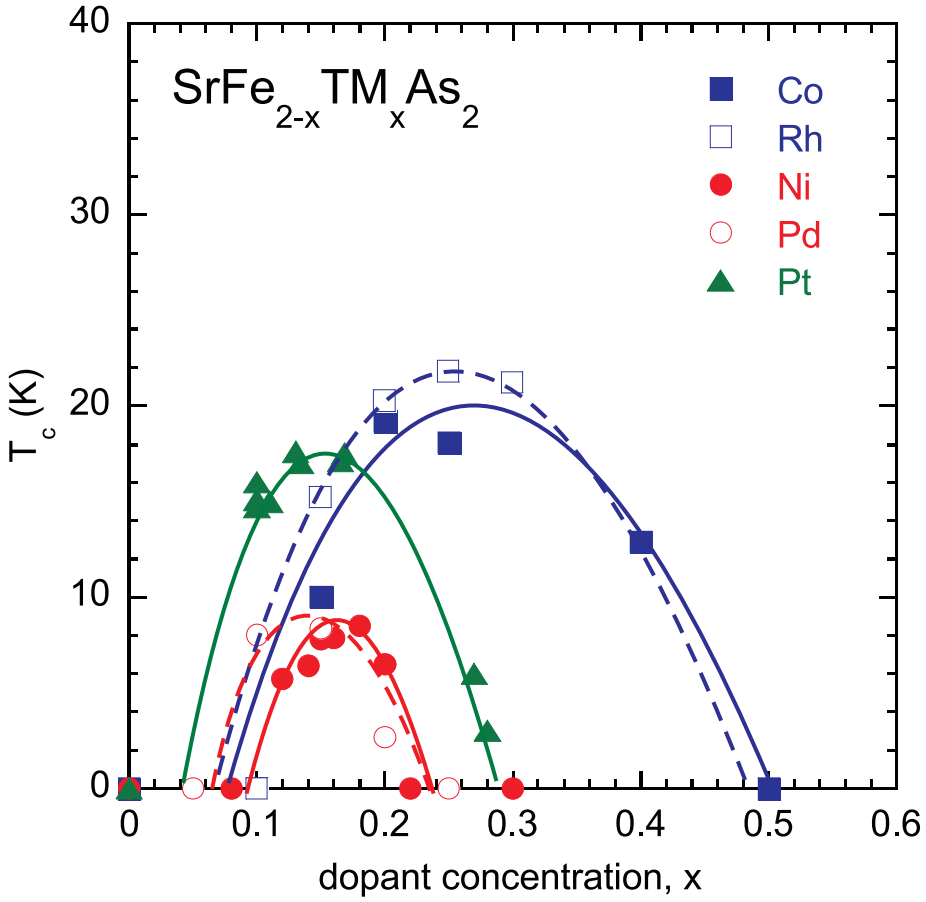

Figure 6.1: Comparison of the evolution of superconductivity as a function of transition metal substitution in $SrFe_{2-x}TM_xAs_2$ (TM = Co [15], Ni [5], Rh [16], Pd [16], and Pt [8]). Solid blue and red symbols denote T_c values for 3d-electron substituents Co (blue square) and Ni (red circle), and open blue and red symbols denote those of 4d substituents Rh (blue square) and Pd (red circle). Pt (a 5d substituent) is shown as solid green triangles. The position of optimal doping is comparable for elements in the same group, with approximately half as much Ni, Pd, or Pt needed to reach optimal doping as Co or Rh. This is consistent with an electron doping picture. The optimal transition temperature, however, varies between systems.

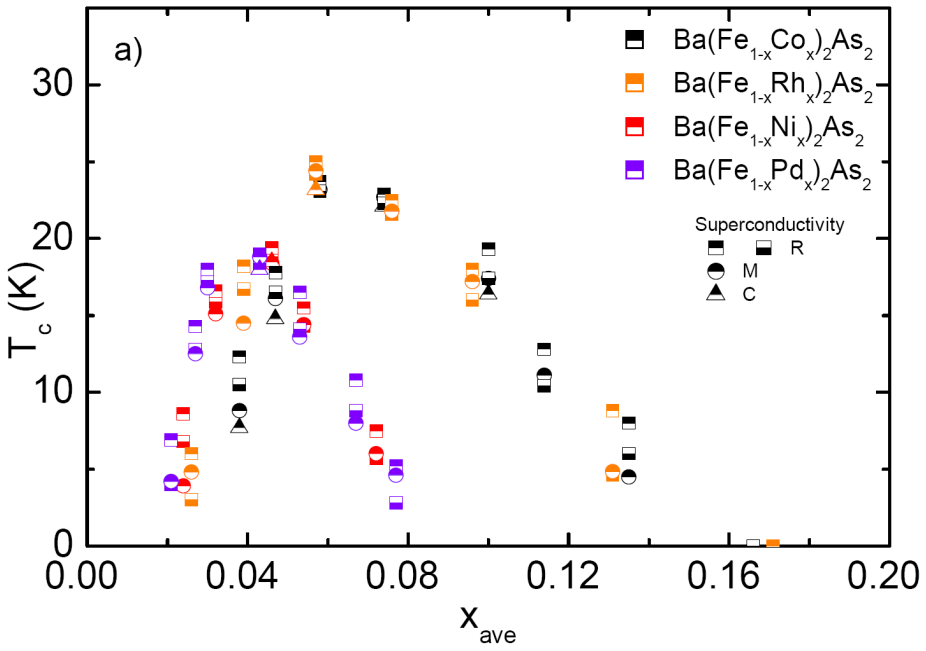

Figure 6.2: Comparison of the evolution of superconductivity as a function of transition metal substitution in $Ba(Fe_{1-x}TM_x)_2As_2$ (TM = Co, Rh, Ni, Pd). As in the case of transition metal substituted $SrFe_2As_2$ (Fig. 6.1), the optimal concentration scales with the electron counding picture, however T_c does not seem to follow any trend. Not pictured here is data for Pt substituted $BaFe_2As_2$ which, similar to the the $SrFe_2As_2$ system, shows an optimal concentration the same as the Ni and Pd systems but with a higher maximum T_c [17, 18]. From Ref. [19].

between the two systems. The similar positioning of the superconducting dome for each system at an optimal concentration of x $\sim$ 0.16 follows that expected for the nominally equivalent addition of two d-electrons from both Pt and Ni substituents, as compared to that of $SrFe_{2-x}Co_xAs_2$ with only one d-electron contribution and a significantly larger optimal doping of x $\sim$ 0.25 [174]. However, a significant factor of two difference is apparent in $T_{c(max)}$ values, presenting an intriguing contrast in two systems with nominally identical phase diagrams. With similar modification of unit cell parameters, nominally identical oxidation states and nearly identical phase diagrams in both substitution series, I consider intrinsic variations in pair-breaking scattering rates as the primary origin of this contrast.

In this chapter I show how the transport scattering rate affects the transition temperature in electron-doped transition metal substituted materials (i.e., an alio-valent transition metal substituted for iron such as Co or Ni, as opposed to, say, Ru substitution which is nominally isovalent). Here I observe a universal trend in iron-based superconductors with the $ThCr_2Si_2$ crystal structure wherein the transition temperature decreases with an increase in the transport scatterin rate, consistent with pair breaking. I then discuss how my reults relate to current models of the pairing symmetry in iron-based superconductors and show that this rate of suppression is consistent with an $s_\pm$ superconductor that has both inter- and intraband coupling.

6.1 Experimental Details

As I have shown in the last chapter, the role of TM substitution in both promoting a superconducting state and shaping the phase diagrams of the 122 systems is an important topic of ongoing debate. While transition metals substitution clearly induces superconductivity in all of these systems, it is unclear precisely what it is the substituent atoms are doing. In the 122 systems, the substitution-induced positioning of the superconducting phase scales reasonably well with d-electron count (with the exception of Cu substitution) [38], and ample evidence of modifications to band structure [149, 150], carrier concentrations [24, 7] and magnetic interactions support a rigid band shift doping model. However, theoretical models predicting the localization of added d-electrons and the importance of impurities raise questions about this approach [154, 155, 156, 180]. Moreover, the similarity of the phase diagram produced by nominally isovalent Ru substitution [173, 181] to that of its aliovalent counterparts necessitates a better understanding of the true nature of TM substitution. Based on these predictions, I treat all optimally doped-transition metal substituted systems as being similar, ignoring which specific TM substituent is used, and thus show that it is the increase in scattering that controls the optimal T_c.

As described in sections 2.4.4 and 2.1.3, for a one-band system the transport scattering rate is given by:

$$\Gamma = \frac{e\rho_{xx}}{m^* R_H} \tag{6.1}$$

To use this equation I must first justify using the one band model. This is not a new technique: several other groups have used this one-band model to calculate carrier densities and scattering rates [22, 95, 26]. Iron-based superconductors are clearly multiband materials, with both hole- and eletron-like bands [38, 36, 37], however previous transport studies have observed an asymmetry in the transport properties of the bands [170, 90]. Indeed, with transition metal substitution the number of electron carriers increases while the carrier concentration of the hole bands decrease. In addition to the decrease in number of hole carriers, the mobility of the hold bands is greatly diminished with transition metal substitution leading to electron-dominated transport properties [171, 172, 90, 47, 170, 182]. Specifically, the study by Olariu *et al.* [90] show that the hole contribution to the transport properties in $BaFe_{2-x}Co_xAs_2$ is, in their words, "barely visible" in the transport properties and that it is greatly decreased in $BaFe_{2-x}Ni_xAs_2$. There have also been optical conductivity measurements of the scattering rate by Barisic *et al.* [183] and Nakajima *et al.* [184] that are well modeled by a single-band Drude formulation with a spectral weight in Co- doped $BaFe_2As_2$ that increases with electron doping, consistent with electron-dominated conduction. Finally, measurements of the transverse resistance in magnetic fields can be used to show multiple conducting band behavior. In a one-band model the transverse resistance should be linear in field, with deviations coming from multiple bands. my own studies of the Hall effect in Ni-, Pd- and Pt- doped systems (see references [7, 8]) as well as any of the studies previously published in the literature (see any references in this chapter) yield the same conclusion, that there is no indication of multiple carriers up to at least 9 T.

Next, I must obtain a value for the effective mass, m^*. I used the effective mass values extracted from quantum oscillations measurements of each of the Sr- [79], Ca- [80] and Ba- [61] based parent compounds as the base value. I use $m^* = 2m_e$ for all systems and assume that any change in effective mass as a function of chemical substitution is relatively small and uniform across the three families. Quantum oscillation measurements are not possible on doped compounds, however there is at least one optical study [185] that indeed confirms my approximation with a measured $m^*(\omega \to 0) \approx 2\ m_e$ in optimally doped $Ba(Fe,Co)_2As_2$, providing further evidence of the validity of my assumption.

Finally, to calculate the zero-temperature scattering rate (the scattering due to impurities), resistivity and Hall coefficents were measured as a function of temperature and the low temperature data was extrapolated to zero temperature, what may be referred to as $\rho_0 = \rho(T = 0)$ and $R_{H0} = R_H(T = 0)$. Resistivity and Hall effect data were obtained using the six-wire technique to minimize the error due to deometric factor (see chapter 2). Shown in Fig. 6.3 are four different optimally-doped TM-substituted samples with T_c values exhibiting a wide range; Pd-, Ni-, Co- and Pt- substituted systems show T_c values of 7 K, 9 K, 17 K, and 20 K, respectively. The first thing to notice is that the systems exhibit an observable difference in absolute resistivity values dominated by a rigid shift in the zero-temperature elastic contribution ρ_0, as evident from the comparable inelastic contributions (i.e., slope of $\rho(T)$). The resulting contrast in T_c values follows this trend, with a systematic reduction of T_c with increasing ρ_0. There is also a slight shift in a power law fit ($\rho = \rho_0 + BT^\alpha$), where the exponent tends toward 1 for higher transition temperatures

similar to that seen in $Sr_{1-x}K_xFe_2As_2$ [89]. The Hall coefficient changes slightly for all systems, indicative that the charge doping picture cannot fully explain the features seen in these systems.

To truly determine if there is a trend in scattering rate across all systems I performed a literature review and obtained data from previously published transport studies on most combinations of $AEFe_{2-x}TM_xAs_2$ with AE = Ca, Sr, or Ba and TM = Ru, Co, Ni, Rh, Pd, and Pt and is presented in table B.1. Most of the data corresponds to systems with electron-dominated transport (nominally aliovalent transition metal substitution) with the exception of Ru substitution, for which I utilize the electron component of ρ_{xx} extracted with a two-band analysis and n_e from ARPES measurements [186] to obtain a value of Γ that can be compared with the other data. In table B.1 I also show data from a few other systems (alkali substituted 122s and 1111s). One can see that in all but TM substituted 122s either the scattering rate or the transition temperature is too high to fit in line with the transition metal substituted 122s, as such all of these systems have been left out of Fig. 6.5. See Appendix B for a comparison of these systems.

6.2 Results and Discussion

I compare the resultant $T_c(\Gamma)$ values with those calculated for all optimally doped TM-substituted 122 samples with ρ_{xx} and R_H values available in the literature, as shown in Fig. 6.5. Closed symbols represent data that has been obtained using the 6-wire technique and should be considered more accurate than the open

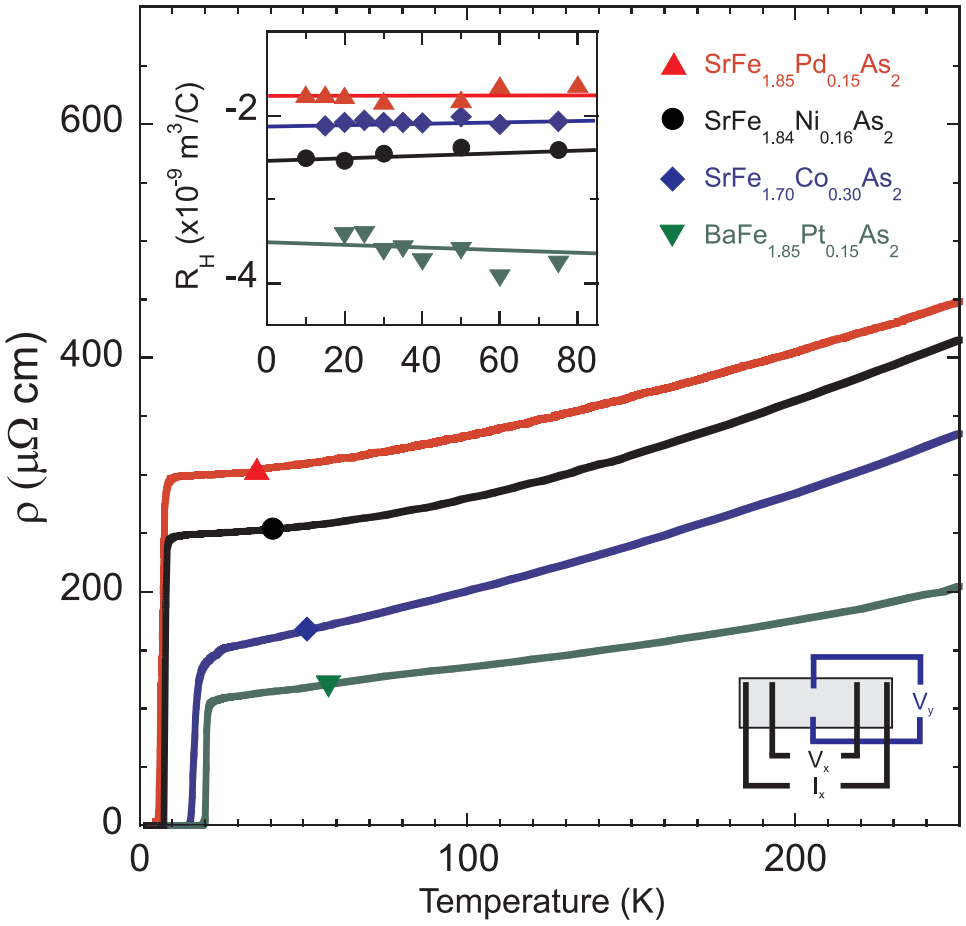

Figure 6.3: Six-wire measurements of resistivity (main panel) and Hall coefficient (inset) of optimally-doped $SrFe_{2-x}Pd_xAs_2$, $SrFe_{2-x}Ni_xAs_2$, $SrFe_{2-x}Co_xAs_2$ and $BaFe_{2-x}Pt_xAs_2$, with T_c values of 7, 9, 17 and 20 K, respectively. The schematic depicts the configuration of the six-wire measurement. From Ref. [9].

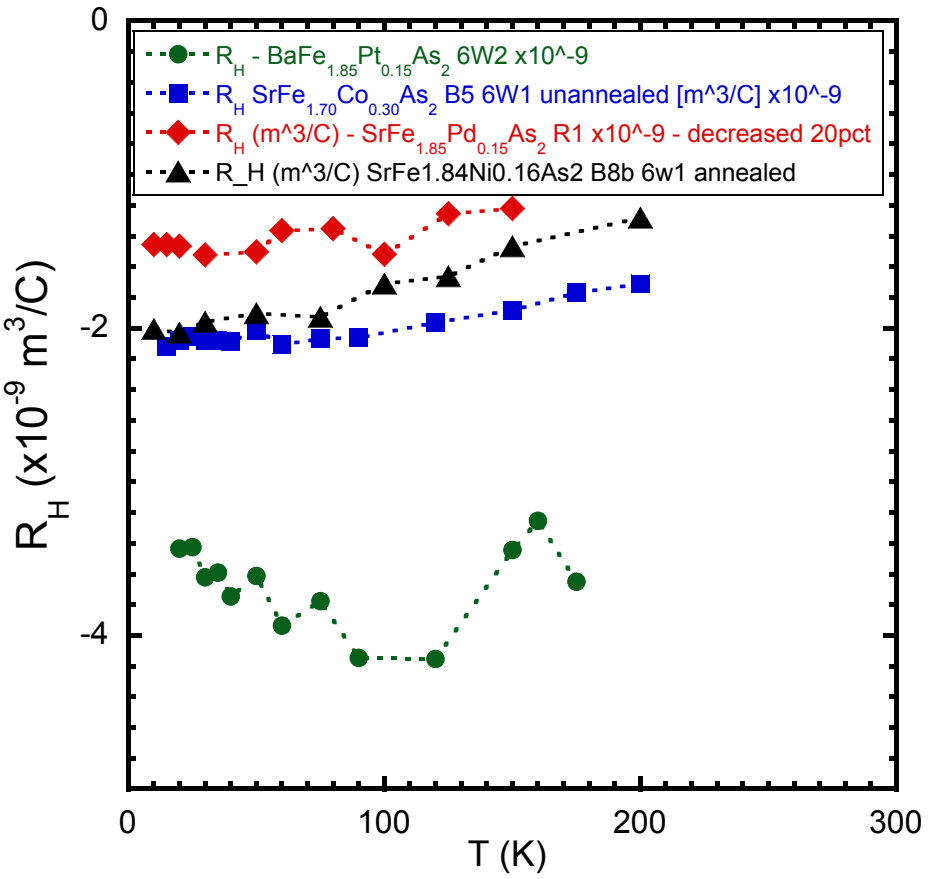

Figure 6.4: Hall coefficient of optimally-doped $SrFe_{2-x}Pd_xAs_2$, $SrFe_{2-x}Ni_xAs_2$, $SrFe_{2-x}Co_xAs_2$ and $BaFe_{2-x}Pt_xAs_2$, with T_c values of 7, 9, 17 and 20 K, respectively. This is the inset of Fig. 6.3 up to 200 K. The Hall coefficient shows very little dependence on temperature.

symbols that correspond to data obtained from the literature using 4-wire measurements of resistivity and Hall coefficient. Remarkably, the T_c values follow the same trend of suppression with increasing Γ, as expected in the AG formalism for a superconductor with increasing levels of pair-breaking impurities [26, 91, 96, 97], surprising in light of the variety of systems presented. In particular, there is no clear trend associated with species of alkaline earth cation or transition metal substituent except for an average reduced scattering rate for Ba-based systems. Instead, it is more likely that the lower substitution concentrations required to reach optimal doping in $BaFe_2As_2$ as compared to $SrFe_2As_2$ is correlated with the as well as the lower magnetic ordering temperature, T_N, having Neél temperatures of 140 and 200 K, respectively. Note that the transport scattering rate values for $BaFe_{2-x}Co_xAs_2$ and $BaFe_{2-x}Ni_xAs_2$ nearly identical to those obtained in optical conductivity measurements [183] if we assume the same effective mass values, providing a confirmation of my analysis.

As discussed above, the rate of suppression of T_c, defined by the critical scattering rate Γ_c where T_c is completely suppressed, is in general dependent on the type of scatterers and the order parameter symmetry. Assuming predominant non-magnetic scattering as evidenced by a paramagnetic normal state and no obvious indication of enhanced magnetism due to TM substitution (e.g., absence of any enhanced susceptibility) [5, 8], the presence of non-magnetic pair-breaking points to a sign-changing order parameter. However, several substitution [96, 187] and irradiation [26, 27, 176] studies report a much weaker rate of suppression than that expected for a sign-changing order parameter; calculations for an ideal $s_\pm$ supercon-

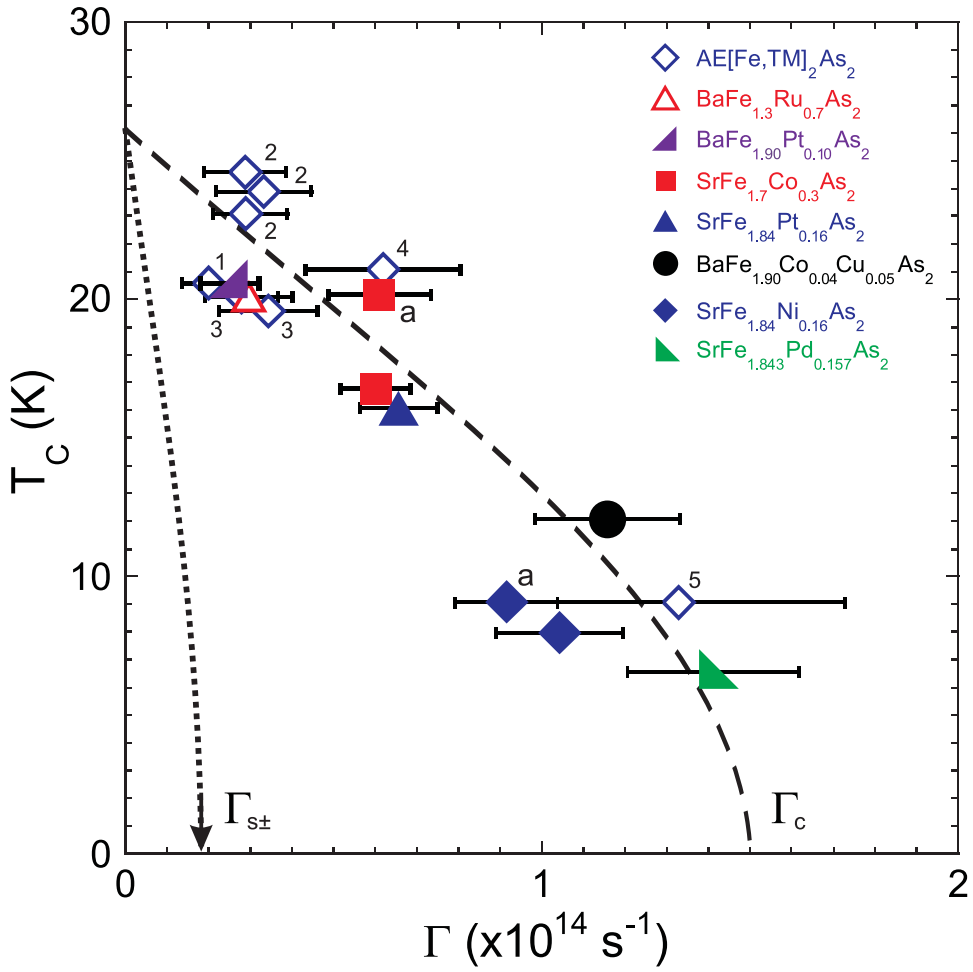

Figure 6.5: Effect of transition metal substitution on T_c values of a wide variety of 122 superconductors at optimal doping concentrations, plotted as a function of the experimental transport scattering rate $\Gamma = e\rho/R_H m^*$ (see text). Closed symbols indicate six-wire measurements (see text), and open symbols indicate values obtained from literature data for (1) $CaFe_{1.92}Co_{0.08}As_2$ [20], (2) $BaFe_{2-x}Co_xAs_2$ [21, 22], (3) $BaFe_{2-x}Ni_xAs_2$ [23, 24], (4) $SrFe_{1.74}Co_{0.26}As_2$ [25] and (5) $SrFe_{1.84}Ni_{0.16}As_2$ (ρ_0 = 212 $\mu\Omega$cm, $R_H(0\ K)=1.4\times10^{-9}$ m^3/C) [7]. Samples of $SrFe_{2-x}Co_xAs_2$ and $SrFe_{2-x}Ni_xAs_2$ denoted with an "a" are annealed (see text.) Although annealing $SrFe_{2-x}Co_xAs_2$ (see Fig. 3) increases T_c without a noticeable change in Γ, the effects of annealing on this system are not as well studied as that of $SrFe_{2-x}Ni_xAs_2$ [6] and are potentially more complex. All T_c values follow a universal rate of suppression with Γ well described by an Abrikosov-Gorkov fit (dashed line) that is much weaker than expected for a superconductor with $s_\pm$ symmetry and interband scattering (dotted line) [26, 27, 28]. From Ref. [9].

ductor with full gaps on both bands [97] and strong interband scattering yield $\Gamma_c(s_\pm)$ = 1.8×10^{13} s^{-1} [26, 27, 28], with similar values for the d-wave case [97]. Shown in Fig. 6.5, a fit to the typical AG functional form (eqn. 2.21) yields a value Γ_c = 1.5×10^{14} s^{-1} corresponding to a critical mean free path of $\sim$ 1.1 nm (using Fermi velocity $v_F = 1.7\times10^5$ m/s [79]), close to the expected superconducting coherence length ξ = 2.8 nm [166].

However, this value of Γ_c is also an order of magnitude larger than the expected $\Gamma_c(s_\pm)$, presenting a significant challenge to models considering a fully gapped $s_\pm$ pairing symmetry, particularly in the presence of strong interband scattering [60, 65]. The "perfect" $s_\pm$ order paramter with only interband scattering is what is most often cited as the model, however it was shown that in an $s_\pm$ order parameter with equal gaps on both bands and *only* interband scattering Γ_c would be the same as that seen in a d-wave superconductor (vertical arrow in Fig. 6.5) [97]. Therefore, the slow suppression of T_c as observed here has been used as evidence for an s_{++} order paramer. But calculations using the T-matrix approximation for an $s_\pm$ state emphasize that both inter- and intra-band scattering in the unitary limit can be decreased with appropriate parameters. They showed that with a larger intra-/interband ratio one can observe a four-fold increase of Γ_c [99]. Unfortunately, there are a large number of parameters included in this model including relative carrier density between the bands, the average of the gap over the Fermi surface, whether the scattering is weak (Born approximation) or strong (unitary limit) and the ratio of intra- to inter-band scattering, so my data alone is not enough using this model to obtain any information without making too many assumptions about

the other parameters. Another recent preprint [100] discusses using disorder to distinguish between $s_{\pm}$ and s_{++} order paramers and points out that there must be a sign change in the order parameter to see T_c suppression and suggests that an increase in interaband scattering relative to interband scattering could cause this slow rate that I observed. Using their model I obtain an inter/intraband ratio between 0.2 and 0.5.

From my data I can also extract information about the optimum clean-limit (Γ=0) transition temperature T_{c0}, an important parameter since it is the value that should be utilized in considering the intrinsic pairing strength. My determination of $T_{c0} = 26$ K is consistent with the well-established maximum T_c value of approx. 25 K found among all TM-doped 122 systems [36], as well as with extrapolated estimations of pressure- and doping-optimized systems such as shown in the comparison of $BaFe_{2-x}Ru_xAs_2$ substitution and pressure dependence [188]. But this observation raises an intriguing question about why T_{c0} does not approach that found in higher T_c intermetallic systems including $Sr_{1-x}K_xFe_2As_2$, $Ba_{1-x}K_xFe_2As_2$ and $BaFe_2As_{2-x}P_x$ [36], which have calculated Γ values in the range shown in 6.5 but much higher transition temperatures. In contrast to the typical explanation of a reduced level of active-plane disorder as the reason for higher T_c values in the alkali metal-doped systems, the determination of T_{c0} and its failure to reach 40 K as in other 122 systems suggests a fundamental asymmetry in pairing strength between electron- and hole-doped systems that does not arise from scattering differences alone (although the effects of strong scattering in the hole bands [90, 170, 186, 22] cannot be discounted as a factor in the observed asymmetry).

A universal $T_c(\Gamma)$ relation suggests a similar pairing potential for all TM-doped 122 compounds that is disrupted by a common scattering mechanism. It is not clear why certain TM substitutions induce more scattering than others, but dramatic variations in seemingly similar elemental substitutions are not unprecedented. For instance, the $BaFe_{2-x}Ru_xAs_2$ system requires $\sim$ 30-40% Ru substitution to obtain optimal doping, which is almost four times higher concentration than Co substitution but results in a very similar value of T_c(max). Such a contrast has been argued to arise from the aliovalent versus isovalent nature of, respectively, Co and Ru substituents, but recent work has put this into question. Mossbauer studies of $BaFe_{2-x}Co_xAs_2$ and $BaFe_{2-x}Ni_xAs_2$ find no change in d-electron population with substitution [153] and similarly x-ray absorption studies reveal no change in the Fe valence with Co substitution in $BaFe_{2-x}Co_xAs_2$ [152, 151]. Furthermore, recent calculations suggest that substituted d-electrons can remain localized at the substituent sites [154], either still resulting in a rigid band shift [189] or generating a phase diagram strikingly similar to that expected from a rigid band shift [190].

Variations in impurity or disorder levels due to details of substitution chemistry likely play a key role in explaining the variation in Γ values observed in the 122 series of superconductors. This is corroborated by observations of enhancements in T_c values after annealing crystals of both low- and high-Γ systems, in particular $BaFe_{2-x}Co_xAs_2$ [191] and $SrFe_{2-x}Ni_xAs_2$ [6], respectively, and confirmed by my study of a $SrFe_{2-x}Ni_xAs_2$ crystal with six-wire measurements obtained before and after annealing: as shown in Fig. 6.5, the shift of data along the AG curve indicates an inverse relation between T_c and Γ. Note also that although annealing

$SrFe_{2-x}Co_xAs_2$ (see Fig. 6.5) increases T_c without a noticeable change in Γ, the effects of annealing on this system are not as well studied as that of $SrFe_{2-x}Ni_xAs_2$ and are potentially more complex (see, for instance, J. Gillett *et al.* [148]). In the case of $BaFe_{2-x}Co_xAs_2$ [191], annealing was shown to enhance T_c to a maximum value of 25 K, consistent with my determined T_{c0} value. The reason why the $BaFe_{2-x}Co_xAs_2$ system is closest to the clean limit is not known, however a lack of observable disorder in Fe-As bond lengths in $BaFe_{2-x}Co_xAs_2$ may have provided an important insight [192]; it would be interesting to perform the same study on high-Γ systems to confirm this scenario.

6.3 Conclusions

I have demonstrated the existence of a universal pair-breaking relation for a wide range of optimally transition metal-doped 122 systems, suggesting a common scattering mechanism and pairing potential across the series. The rate of suppression of T_c and the contrast between the optimum (zero-scattering) T_{c0} value of $\sim$26 K and the higher T_c values achieved in non-transition metal substitution series provides important constraints on the pairing symmetry and mechanism in the intermetallic iron-based superconductors. This data is consistent with the $s_\pm$ order parameter considered by many groups to the be most likely candidate for the pairing symmetry in iron-based superconductors. Early models dealt with only interband scattering which would lead to a response to scattering equal to that of a d-wave order parameter. This data, however, shows that this system has significant

intraband scattering which, according to the recent theoretical study by Wang *et al.* [100], could have a ratio of inter/intraband scattering between 0.2 and 0.5.

Future studies should first attempt to fit this data to a model to determine inter- and intraband coupling strengths. The study by Wang *et al.* would seem to be a good place, however this model takes into account many parameters including the presence of nodes on gaps and the relative carrier concentration between bands. As such, I would need to work with this group to determine experimentally verifiable values for these parameters.

Finally, I would like to study the microscopic differences between transition metal substituents and determine the origin of this higher scattering rate. If this higher scattering rate in Ni-substituted systems in fact comes from disorder, then there should be some way to measure this disorder. Annealing effects can be one way, however EXAFS measurements of Fe-As bond lengths in TM-substituted $AEFe_2As_2$ (Ref. [192]) may provide information about disorder in the superconducting Fe-As plane. Performing this experiments on high-Γ systems can be used to confirm this scenario. The washing-out of the Fermi surface as measured by ARPES can also be used to provide a qualitive comparison between systems.

Chapter 7

Conclusions

In this thesis I summarized several experimental studies on electronic transport in iron-based superconductors. Single crystals in the 122 family ($AEFe_2As_2$, AE = Ca, Sr, Ba) were synthesized using the self flux method method of crystal growth and measured using four-wire resistivity techniques at temperatures down to 2 K and in magnetic fields up to 14 T. In addition to studies of the parent compounds of Ca-, Sr-, and $BaFe_2As_2$, solid solutions of the $Ca_{1-y}Sr_yFe_2As_2$ and $Sr_{1-x}Ba_xFe_2As_2$ series were measured, as were transition metal substituted crystals with the chemical formula $AEFe_{2-x}TM_xAs_2$ (AE = Ca, Sr, Ba; TM = Co, Rh, Ni, Pd, Pt).

In order to investigate the unique superconducting properties of $SrFe_2As_2$ I performed transport, magnetic susceptibility, and crystallographic measurements on single crystals. In most cases superconductivity is stabilised only after the application of external pressure, chemical substitution, or charge doping. In $SrFe_2As_2$, however, I found that undoped, unpressurized crystals could exhibit superconductivity with a full resistive transition, large upper critical fields, and a volume fraction of up to 15% (but typically below 10%). Interestingly, I found that annealing could be used to remove the superconducting phase, with only very small heat treatments of 300 °C for less than 10 minutes needed to drive the system completely normal. I also found that cold-working the sample by either applying and removing pressure

or severely deforming the sample in a press can bring back superconductivity. Because of these observations I posited that the cause of the supercondcutivity was some sort of internal strain in the crystal and performed crystallographic studies to determine this. I found that the cause seems to be layer stacking faults, with shifting seen in the h0l directions but not in the kh0 plane. Finally, I observe an enhanced magnetic susceptibility and ferromagnetic moment associated with this superconducting phase.

To determine the effect that chemical pressure has on 122s, I studied magnetic and transport properties of the $Ca_{1-y}Sr_yFe_2As_2$ and $Sr_{1-x}Ba_xFe_2As_2$ series. I found that the a- and c-axes as well as the unit cell volume decrease monotonically leading to the term chemical pressure being applied, although this term may be misleading. Other studies have found that crystals with this unit cell volume under pressure exhibit superconductivity, so there must be something else that allows for pairing that is not seen in these. It may be related to the fact that the magnetic order in these systems is never suppressed, with the lowest T_N seen in $BaFe_2As_2$ around 140 K. There is very little change in the transport properties substituting from Ba to Sr, however from Sr to Ca at 70% Ca I see a hysteresis in the resistivity measurements associated with a change from 2^{nd} to 1^{st} order transition. At the same point, the Neél temperature begins to rapidly decrease. I find from neutron diffraction measurements that over this same region the ordered moment remains constant at 0.9 μ_B. The stability of the ordered moment and temperature dependence of magnetic susceptibility and resistivity suggest that it is the structural ordering that has more impact on the charge carriers, consistent with itinerant magnetism.

Transition metal substitution is known to induce superconductivity, so when iron-based superconductors were first discovered many groups were measuring transition metal substituted 122s in order to produce the phase diagrams. As such, ours was the first group to report on single crystals of both $SrFe_{2-x}Ni_xAs_2$ and $SrFe_{2-x}Pt_xAs_2$. I measured transport properties of these materials and found that both exhibit superconductivity over a limited range of substitution centered around x = 0.16. The optimal T_c for the Ni system was 9 K while in the Pt system it went up to 16 K. The differences between Ni and Pt substitution were noteworthy, with the Pt system having a wider and taller superconducting dome (in the phase diagram) and the Ni system responding to annealing. The effect of annealing on $SrFe_{2-x}Ni_xAs_2$ to raise T_c by 1-2 K is significant, as it seems that the Ni system has more inherent disorder that can be partially removed, either due to doping disorder or disorder in the crystal structure, neither of which have been proven conclusively.

Finally, in an attempt to answer why different transition metal substituents lead to different transition temperatures I measured the transport scattering rate, Γ, using the 6-wire technique to remove uncertainty in layer thickness. I found that T_c decreases with scattering rate, a trend that is described by pair breaking as was originally theoretically laid out by Abrikosov and Gor'kov. Using my results I determined, first, that the maximum transition temperature for transition metal substituted iron-based superconductors is approx. 26 K, and second, that the scattering rate at which T_c drops to zero (Γ_c) is approximately ten times higher than that expected for either a d-wave superconductor or a "perfect" $s_{\pm}$ superconductor with equal gaps and only interband scattering. I concluded that there must be

significant intraband scattering that is, according to one theoretical model, 2 to 5 times larger than the intraband scattering.

In general, this thesis brings to light several questions about assumptions that are often made when discussing iron-based superconductors. The exact nature of elemental substitution is not known, however my study on alkaline earth substitution shows that treating it only as chemical pressure is not completely accurate. If, however, it were only charge doping as some have suggested then Ni and Pt substitution should be expected to give the same results. Clearly this is not the case. Instead, it seems as though transition metal substitution acts as impurity centers with differing strength, suppressing magnetism at different rates and leading to higher or lower transition temperatures. This picture also leads to my final conclusion, that these materials most likely have an $s_{\pm}$ order parameter with a large intra/interband ratio based on the response to impurities in the superconducting plane. Future studies should be used to determine the microscopic effects of transition metal substitution on the 122 materials as well as attempt to address the cause of the increased scattering rate in some systems.

Appendix A

Lattice Constants for Select Concentrations in the [Ca, Sr, Ba]Fe_2As_2 Series

Table A.1: Crystallographic data for $Ba_{1-x}Sr_xFe_2As_2$ determined by single-crystal x-ray diffraction. The structure was solved and refined using the SHELXS-97 software, yielding lattice constants with residual factors as specified. Data for $BaFe_2As_2$ (x=0) taken from [M. Rotter *et al.* , Phys. Rev. B **78** 020503(R) (2008)].

$Ba_{1-x}Sr_xFe_2As_2$	x=0	x=0.35	x=0.72	x=1
Temperature	250 K	250 K	250 K	250 K
Structure	Tetragonal	Tetragonal	Tetragonal	Tetragonal
Space group	I4/mmm	I4/mmm	I4/mmm	I4/mmm
a(Å)	3.9625(1)	3.9388(7)	3.9412(4)	3.9289(3)
c(Å)	13.0168(3)	12.753(5)	12.573(3)	12.320(2)
V[3](Å^3	204.38(1)	197.85(9)	195.29(5)	190.17(2)
Z (formula unit/unit cell)	2	2	2	2
Density(g/cm^3)	—	6.403	6.174	6.098
Refl.collected	1427	1683	1275	1443
Independent refl.	106	113	119	112
R_{int}[1] (%)	5.22	2.89	3.21	2.79
wR_2[2], all refl. (%)	3.58	3.56	3.44	3.31
R_1[3], I$\geq 2\sigma$I (%)	1.43	1.61	1.44	1.36
Atomic parameters:				
Ba/Sr	2a(0,0,0)	2a(0,0,0)	2a(0,0,0)	2a(0,0,0)
Fe	4d(1/2,0,1/4)	4d(1/2,0,1/4)	4d(1/2,0,1/4)	4d(1/2,0,1/4)
As	4e(0,0,z)	4e(0,0,z)	4e(0,0,z)	4e(0,0,z)
z	0.3545(1)	0.35630(6)	0.35848(5)	0.36035(5)
Atomic displacement parameters U_{eq} (Å^2):				
Ba1/Sr1	0.0095(5)	0.0093(2)	0.0125(2)	0.0108(2)
Fe1	0.0057(6)	0.0078(2)	0.0119(2)	0.0096(2)
As1	0.0099(5)	0.0083(2)	0.01214(19)	0.00964(17)
Bond lengths (Å):				
Ba/Sr-As(Å)	3.382(1) × 8	3.3341(7) × 8	3.3064(5) × 8	3.2677(4) × 8
Fe-As(Å)	2.403(1) × 4	2.3908(6) × 4	2.3965(5) × 4	2.3890(4) × 4
Fe-Fe(Å)	2.802(1) × 4	2.3908(6) × 4	2.7869(5) × 4	2.7782(4) × 4
Bond angles (deg):				
As-Fe-As	111.1(1) × 2	110.92(4) × 2	110.63(3) × 2	110.63(3) × 2
As-Fe-As	108.7(1) × 4	108.752(19) × 4	108.896(15) × 4	108.895(14) × 4

Table A.2: Crystallographic data for $Sr_{1-y}Ca_yFe_2As_2$ determined by single-crystal x-ray diffraction. The structure was solved and refined using the SHELXS-97 software, yielding lattice constants with residual factors as specified.

$Sr_{1-y}Ca_yFe_2As_2$	y=0.30	y=0.32	y=0.64
Temperature	250 K	250 K	250 K
Structure	Tetragonal	Tetragonal	Tetragonal
Space group	I4/mmm	I4/mmm	I4/mmm
a(Å)	3.9164(6)	3.9219(12)	3.9044(6)
c(Å)	12.151(4)	12.163(8)	11.974(3)
V^3(Å^3	186.37(7)	187.08(14)	182.53(7)
Z (formula unit/u.c.)	2	2	2
Density(g/cm^3)	5.968	5.945	5.799
Refl.collected	1427	1272	1322
Independent refl.	106	108	104
R_{int}[1] (%)	6.68	4.53	5.66
wR_2[2], all refl. (%)	2.75	3.29	2.96
R_1[3], I$\geq 2\sigma$I (%)	1.2	1.7	1.4
Atomic parameters:			
Sr/Ca	2a(0,0,0)	2a(0,0,0)	2a(0,0,0)
Fe	4d(1/2,0,1/4)	4d(1/2,0,1/4)	4d(1/2,0,1/4)
As	4e(0,0,z)	4e(0,0,z)	4e(0,0,z)
z	0.36219(4)	0.36221(6)	0.36429(4)
Atomic displacement parameters U_{eq} (Å^2):			
Sr1/Ca1	0.0123(2)	0.0123(4)	0.0113(3)
Fe1	0.01162(16)	0.0113(2)	0.01041(19)
As1	0.01152(14)	0.01150(19)	0.01045(16)
Bond lengths (Å):			
Sr/Ca-As(Å)	3.2362(5) × 8	3.2403(10) × 8	3.2036(5) × 8
Fe-As(Å)	2.3859(4) × 4	2.3892(8) × 4	2.3841(4) × 4
Fe-Fe(Å)	2.7693(4) × 4	2.7732(8) × 4	2.7608(4) × 4
Bond angles (deg):			
As-Fe-As	110.32(3) × 2	110.32(5) × 2	109.94(3) × 2
As-Fe-As	109.050(13) × 4	109.05(2) × 4	109.237(13) × 4

Table A.3: Crystallographic data for $Sr_{1-y}Ca_yFe_2As_2$ determined by single-crystal x-ray diffraction. The structure was solved and refined using the SHELXS-97 software, yielding lattice constants with residual factors as specified. (Continued from previous table)

$Sr_{1-y}Ca_yFe_2As_2$	y=0.67	y=0.79	y=1
Temperature	250 K	250 K	250 K
Structure	Tetragonal	Tetragonal	Tetragonal
Space group	I4/mmm	I4/mmm	I4/mmm
a(Å)	3.9066(8)	3.8993(8)	3.8948(14)
c(Å)	11.988(5)	11.860(5)	11.679(8)
V^3(Å^3	182.95(9)	180.32(9)	177.16(15)
Z (formula unit/u.c.)	2	2	2
Density(g/cm^3)	6.045	5.730	5.654
Refl.collected	987	1258	994
Independent refl.	106	104	102
R_{int}[1] (%)	2.7	5.34	3.59
wR_2[2], all refl. (%)	4.52	2.56	5.72
R_1[3], I$\geq 2\sigma$I (%)	1.96	1.09	2.52
Atomic parameters:			
Sr/Ca	2a(0,0,0)	2a(0,0,0)	2a(0,0,0)
Fe	4d(1/2,0,1/4)	4d(1/2,0,1/4)	4d(1/2,0,1/4)
As	4e(0,0,z)	4e(0,0,z)	4e(0,0,z)
z	0.36423(7)	0.36498(3)	0.36649(10)
Atomic displacement parameters U_{eq} (Å^2):			
Sr1/Ca1	0.0116(5)	0.0123(3)	0.0135(6)
Fe1	0.0125(3)	0.01229(15)	0.0112(4)
As1	0.0119(2)	0.01246(13)	0.0107(3)
Bond lengths (Å):			
Sr/Ca-As(Å)	3.2062(7) × 8	3.1885(6) × 8	3.1648(12) × 8
Fe-As(Å)	2.3855(7) × 4	2.3792(5) × 4	2.3756(10) × 4
Fe-Fe(Å)	2.7624(6) × 4	2.7572(6) × 4	2.7540(10) × 4
Bond angles (deg):			
As-Fe-As	109.94(4) × 2	110.06(3) × 2	110.12(6) × 2
As-Fe-As	109.24(2) × 4	109.178(14) × 4	109.15(3) × 4

Appendix B

Additional Figures for Pair Breaking Chapter

Table B.1: Resistivity and Hall Coefficient data obtained from literature.

Sample	T_c (K)	ρ_0 ($\mu\Omega$.cm)	$R_H(0)$ ($\times 10^{-9}$ m^3/C)	Reference
$SrFe_{1.74}Co_{0.26}As_2$	21.0	156	2.21	Ref. [25]
$CaFe_{1.92}Co_{0.08}As_2$	20.5	55.4	2.40	Ref. [20]
$BaFe_{1.90}Ni_{0.10}As_2$	20.0	131	4.09	Ref. [23, 24]
$BaFe_{1.86}Co_{0.14}As_2$	23.0	87.1	2.62	Ref. [22]
$SrFe_{1.7}Co_{0.3}As_2$ unannealed	16.7	138	2.02	unpublished
$SrFe_{1.7}Co_{0.3}As_2$ annealed	20.1	145	2.07	unpublished
$SrFe_{1.84}Pt_{0.16}As_2$	16.0	285	3.80	Ref. [8]
$SrFe_{1.84}Ni_{0.16}As_2$	9.0	212	1.4	Ref. [7, 5]
$BaFe_{1.9062}Co_{0.0428}Cu_{0.0310}As_2$	12.0	4.01	530	[9]
$BaFe_{1.84}Co_{0.16}As_2$	23.8	106.7	2.8	Ref. [170, 21, 159]
$BaFe_{1.91}Ni_{0.09}As_2$	19.5	120	3.048	Ref. [90]
$BaFe_{1.86}Co_{0.14}As_2$	24.5	84.0	2.54	Ref. [90]
$BaFe_{1.90}Pt_{0.10}As_2$	23.0	106	3.50	[18]
$SrFe_{1.85}Pd_{0.15}As_2$	6.5	350.0	1.8	[9]
$BaFe_{1.30}Ru_{0.7}As_2$	20.0	45.0	0.3	Ref. [186]
$Sr_{0.6}K_{0.4}Fe_2As_2$	38.0	200.0	1.0	Ref. [46]
$Ba_{0.6}K_{0.4}Fe_2As_2$	37.0	120.0	4.0	Ref. [193, 169]
$BaFe_2As_{1.34}P_{0.66}$	31.0	30.0	3.1	Ref. [85]
$LaFe_{0.925}Co_{0.075}OAs$	12.5	130.0	10.0	Ref. [194]
$NdFeAsO_{0.82}F_{0.18}$	50.0	100.0	13.5	Ref. [195]

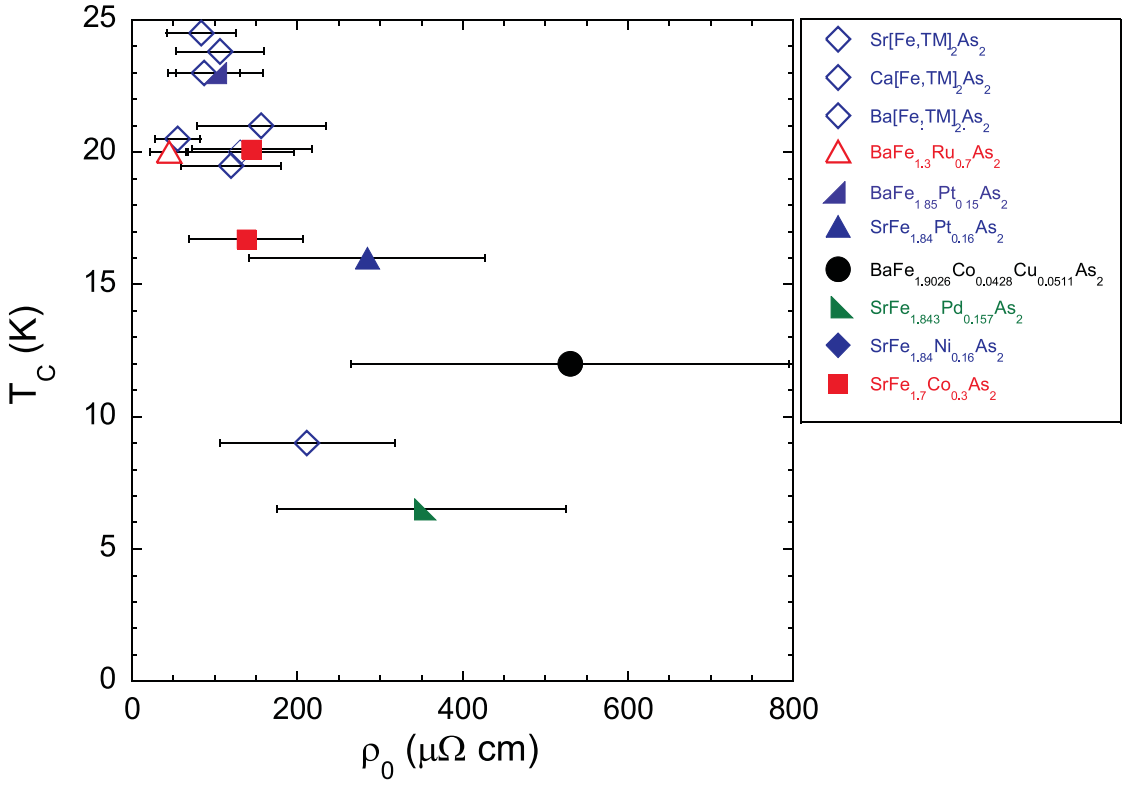

Figure B.1: Superconducting transition temperature as a function of residual resistivity for several 122 systems. As discussed in Chapters 2 and 6, the residual resistivity is a measure of disorder in a system. This figure is further confirmation that T_c decreases with increasing scattering in the 122 systems. This data, however, is taken only using 4-wire measurements, and thus the large error bars are included to account for layer decoupling and the large error in thickness measurements.

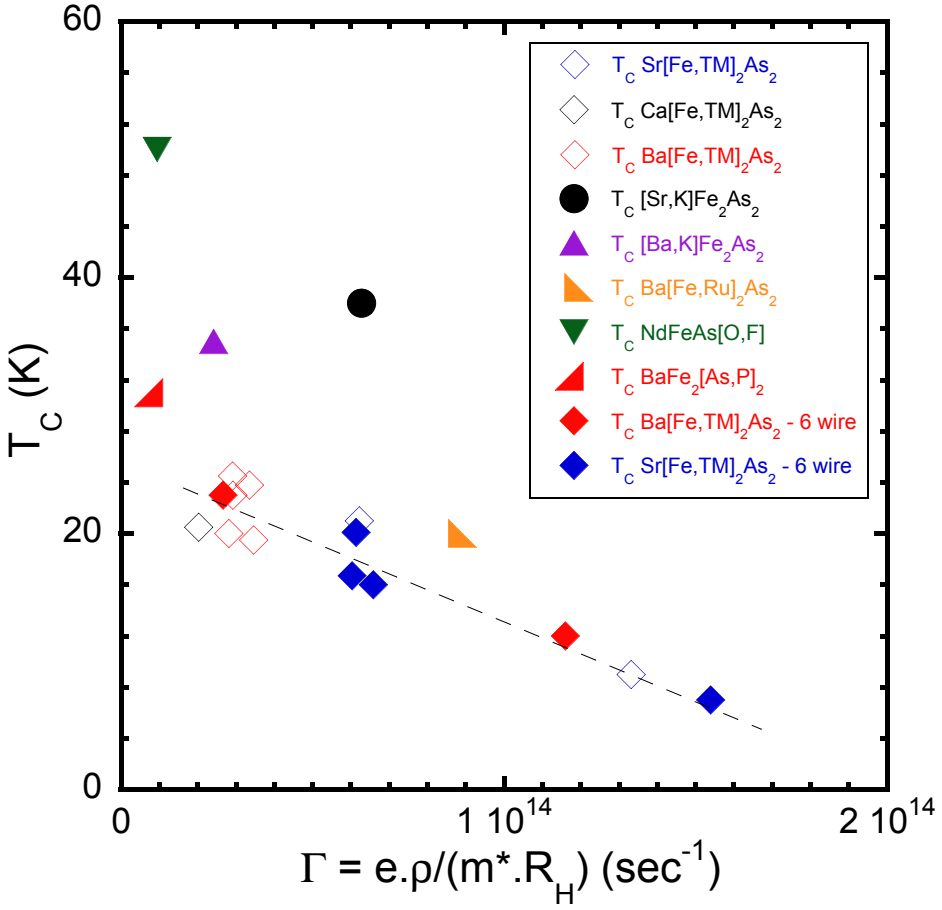

Figure B.2: Superconducting transition temperature as a function of transport scattering rate, Γ, for several iron-based superconductors. Solid diamonds represent data obtained using 6-wire measurements while open diamonds represent data obtained from the literature using 4-wire measurements. This figure is another version of fig. 6.5 that includes data from systems other than transition metal substited 122s and demonstrates that these do not fit with the trend seen in electron doped 122s. Finally, it is interesting to note that in general, TM substituted Ca- and $BaFe_2As_2$ have lower scattering rates than the Sr-based 122s. This may be related to the fact that it takes more TM substituent to induce superconductivity in the Sr systems.

Bibliography

[1] S. Saha, N. Butch, K. Kirshenbaum, and J. Paglione, "Superconducting and ferromagnetic phases induced by lattice distortions in $SrFe_2As_2$," *Physical Review Letters*, vol. 103, p. 037005, 2009.

[2] K. C. Kirshenbaum, S. R. Saha, N. P. Butch, J. D. Magill, and J. Paglione, "Superconductivity in the iron-pnictide parent compound $SrFe_2As_2$," *Science and Technology for Humanity (TIC-STH), 2009 IEEE Toronto International Conference*, p. 891, 2009.

[3] K. Kirshenbaum, N. P. Butch, S. R. Saha, P. Y. Zavalij, B. G. Ueland, J. W. Lynn, and J. Paglione, "Tuning magnetism in FeAs-based materials via a tetrahedral structure," *Physical Review B*, vol. 86, p. 060504(R), 2012.

[4] S. R. Saha, K. Kirshenbaum, N. P. Butch, J. Paglione, and P. Y. Zavalij, "Uniform chemical pressure effect in solid solutions $Ba_{1-x}Sr_xFe_2As_2$ and $Sr_{1x}Ca_xFe_2As_2$," *Journal of Physics: Conference Series*, vol. 273, p. 012104, 2011.

[5] S. Saha, N. Butch, K. Kirshenbaum, and J. Paglione, "Evolution of bulk superconductivity in $SrFe_2As_2$ with Ni substitution," *Physical Review B*, vol. 79, p. 224519, 2009.

[6] S. R. Saha, N. P. Butch, K. Kirshenbaum, and J. Paglione, "Annealing effects on superconductivity in $SrFe_{2-x}Ni_xAs_2$," *Physica C*, vol. 470, p. S379, 2010.

[7] N. P. Butch, S. R. Saha, X. H. Zhang, K. Kirshenbaum, R. L. Greene, and J. Paglione, "Effective carrier type and field-dependence of the reduced-T_c superconducting state in $SrFe_{2-x}Ni_xAs_2$," *Physical Review B*, vol. 81, p. 024518, 2010.

[8] K. Kirshenbaum, S. R. Saha, T. Drye, and J. Paglione, "Superconductivity and magnetism in platinum-substituted $SrFe_2As_2$ single crystals," *Physical Review B*, vol. 82, p. 144518, 2010.

[9] K. Kirshenbaum, S. R. Saha, S. Ziemak, T. Drye, and J. Paglione, "Universal pair-breaking in transition metal-substituted iron-pnictide superconductors," *Physical Review B*, vol. 86, p. 140505(R), 2012.

[10] Q. Huang, Y. Qiu, W. Bao, M. A. Green, J. W. Lynn, Y. C. Gasparovic, T. Wu, G. Wu, and X. H. Chen, "Neutron-diffraction measurements of magnetic order and a structural transition in the parent $BaFe_2As_2$ compound of feas-based high-temperature superconductors," *Physical Review Letters*, vol. 101, p. 257003, 2008.

[11] J. Zhao, W. R. II, J. W. Lynn, G. F. Chen, J. L. Luo, N. L. Wang, J. Hu, and P. Dai, "Spin and lattice structures of single-crystalline $SrFe_2As_2$," *Physical Review B*, vol. 78, p. 140504(R), 2008.

[12] A. I. Goldman, D. N. Argyriou, B. Ouladdiaf, T. Chatterji, A. Kreyssig, S. Nandi, N. Ni, S. L. Budko, P. C. Canfield, and R. J. McQueeney, "Lattice and magnetic instabilities in $CaFe_2As_2$: A single-crystal neutron diffraction study," *Physical Review B*, vol. 78, p. 100506(R), 2008.

[13] A. I. Goldman, A. Kreyssig, K. Prokes, D. K. Pratt, D. N. Argyriou, J. W. Lynn, S. Nandi, S. A. J. Kimber, Y. Chen, Y. B. Lee, G. Samolyuk, J. B. L. ao, S. J. Poulton, S. L. Budko, N. Ni, P. C. Canfield, B. N. Harmon, and R. J. McQueeney, "Lattice collapse and quenching of magnetism in $CaFe_2As_2$ under pressure: A single-crystal neutron and x-ray diffraction investigation," *Physical Review B*, vol. 79, p. 024513, 2009.

[14] A. Kreyssig, M. A. Green, Y. Lee, G. D. Samolyuk, P. Zajdel, J. W. Lynn, S. L. Budko, M. S. Torikachvili, N. Ni, S. Nandi, J. B. L. ao, S. J. Poulton, D. N. Argyriou, B. N. Harmon, R. J. McQueeney, P. C. Canfield, and A. I. Goldman, "Pressure-induced volume-collapsed tetragonal phase of $CaFe_2As_2$ as seen via neutron scattering," *Physical Review B*, vol. 78, p. 184517, 2008.

[15] A. Leithe-Jasper, W. Schnelle, C. Geibel, and H. Rosner, "Superconducting state in $SrFe_{2-x}Co_xAs_2$ by internal doping of the iron arsenide layers," *Physical Review Letters*, vol. 101, p. 207004, 2008.

[16] F. Han, X. Zhu, P. Cheng, G. Mu, Y. Jia, L. Fang, Y. Wang, H. Luo, B. Zeng, B. Shen, L. Shan, C. Ren, and H.-H. Wen, "Superconductivity and phase diagrams of the 4d- and 5d-metal-doped iron arsenides $SrFe_{2x}M_xAs_2$ (M=Rh,Ir,Pd)," *Physical Review B*, vol. 80, p. 024506, 2009.

[17] X. Zhu, F. Han, G. Mu, J. Tang, J. Ju, K. Tanigaki, and H.-H. Wen, "Superconductivity induced by doping platinum in $BaFe_2As_2$," *Physical Review B*, vol. 81, p. 104525, 2010.

[18] K. K. N. P. B. P. Y. Z. J. P. S. R. Saha, T. Drye, "Superconductivity at 23 K in pt doped $BaFe_2As_2$ single crystals," *Journal of Physics: Condensed Matter*, vol. 22, p. 072204, 2010.

[19] N. Ni, A. Thaler, A. Kracher, J. Q. Yan, S. L. Bud'ko, and P. C. Canfield, "Phase diagrams of $Ba(Fe_{1-x}TM_x)_2As_2$ (TM = Rh, Pd) single crystals," *Physical Review B*, vol. 80, p. 024511, 2009.

[20] M. Matusiak, Z. Bukowski, and J. Karpinski, "Nernst effect in single crystals of the pnictide superconductor $CaFe_{1.92}Co_{0.08}As_2$ and parent compound $CaFe_2As_2$," *Physical Review B*, vol. 81, p. 020510, 2010.

[21] E. D. Mun, S. L. Budko, N. Ni, A. N. Thaler, and P. C. Canfield, "Thermoelectric power and hall coefficient measurements on $Ba(Fe_{1-x}T_x)_2As_2$ (T=Co and Cu)," *Physical Review B*, vol. 80, p. 054517, 2009.

[22] F. Rullier-Albenque, D. Colson, A. Forget, and H. Alloul, "Hall effect and resistivity study of the magnetic transition, carrier content, and fermi-liquid behavior in $Ba(Fe_{1-x}Co_x)_2As_2$," *Physical Review Letters*, vol. 103, p. 057001, 2009.

[23] Z. Xu, Q. Tao, L. Li, J. Shen, X. Lin, and G. Cao, "Ni doping effect and phase diagram of Ni-doped $BaFe_2As_2$," *Physica C*, vol. 470, p. S447, 2009.

[24] L. J. Li, Y. K. Luo, Q. B. Wang, H. Chen, Z. Ren, Q. Tao, Y. K. Li, X. Lin, M. He, Z. W. Zhu, G. H. Cao, and Z. A. Xu, "Superconductivity induced by Ni doping in $BaFe_2As_2$ single crystals," *New Journal of Physics*, vol. 11, p. 025008, 2009.

[25] X. Zhang, S. Saha, N. P. Butch, K. Kirshenbaum, J. Paglione, R. L. Greene, Y. Liu, L. Yan, Y. S. Oh, K. H. Kim, and I. Takeuchi, "Josephson effect between electron-doped and hole-doped iron pnictide single crystals," *Applied Physics Letters*, vol. 95, p. 062510, 2009.

[26] A. E. Karkin, J. Werner, G. Behr, , and B. N. Goshchitskii, "Neutron-irradiation effects in polycrystalline $LaFeAsO_{0.9}F_{0.1}$ superconductors," *Physical Review B*, vol. 80, p. 174512, 2009.

[27] C. Tarantini, M. Putti, A. Gurevich, Y. Shen, R. K. Singh, J. M. Rowell, N. Newman, D. C. Larbalestier, P. Cheng, Y. Jia, and H.-H. Wen, "Suppression of the critical temperature of superconducting NdFeAs(OF) single crystals by kondo-like defect sites induced by α-particle irradiation," *Physical Review Letters*, vol. 104, p. 087002, 2010.

[28] V. G. Kogan, "Pair breaking in iron pnictides," *Physical Review B*, vol. 80, p. 214532, 2009.

[29] H. K. Onnes, "The resistance of pure mercury at helium temperatures," *Comm. Phys. Lab. Univ. Leiden*, no. 120b, 1911.

[30] W. Meissner and R. Ochsenfeld *Naturwissenschaften*, vol. 21, p. 787, 1933.

[31] J. Bardeen, L. N. Cooper, and J. R. Schrieffer, "Theory of superconductivity," *Physical Review*, vol. 108, p. 1175, 1957.

[32] J. G. Bednorz and K. A. Müller, "Possible high T_c superconductivity in the Ba-La-Cu-O system.," *Zeitschrift für Physik B*, vol. 64, p. 189, 1986.

[33] M. Tinkham, *Introduction to Superconductivity*. Dover Publications, 1996.

[34] N. P. Butch, M. C. de Andrade, and M. B. Maple, "Resource letter SCY-3: Superconductivity," *American Journal of Physics*, vol. 76, no. 2, p. 106, 2008.

[35] Y. Kamihara, T. Watanabe, M. Hirano, and H. Hosono, "Iron-based layered superconductor La[$O_{1-x}F_x$]FeAs (x = 0.05-0.12) with T_c = 26 k," *Journal of the American Chemical Society*, vol. 130, p. 3296, 2008.

[36] J. Paglione and R. L. Greene, "High-temperature superconductivity in iron-based materials," *Nature Physics*, vol. 6, p. 645, 2010.

[37] P. J. Hirschfeld, M. M. Korshunov, and I. I. Mazin, "Gap symmetry and structure of Fe-based superconductors," *Reports on Progress in Physics*, vol. 74, p. 124508, 2011.

[38] P. C. Canfield and S. L. Bud'ko, "FeAs-based superconductivity: A case study of the effects of transition metal doping on $BaFe_2As_2$," *Annual Review of Condensed Matter Physics*, vol. 1, p. 27, 2010.

[39] K. Ishida, Y. Nakai, and H. Hosono, "To what extent iron-pnictide new superconductors have been clarified: A progress report," *Journal of the Physical Society of Japan*, vol. 78, p. 062001, 2009.

[40] D. J. Scalapino, "A common thread: The pairing interaction for unconventional superconductors," *Reviews of Modern Physics*, vol. 84, p. 1383, 2012.

[41] W. Yu, A. A. Aczel, T. J. Williams, S. L. Budko, N. Ni, P. C. Canfield, and G. M. Luke, "Absence of superconductivity in single-phase $CaFe_2As_2$ under hydrostatic pressure," *Physical Review B*, vol. 79, p. 020511(R), 2009.

[42] N. Ni, M. E. Tillman, J.-Q. Yan, A. Kracher, S. T. Hannahs, S. L. Budko, and P. C. Canfield, "Effects of co substitution on thermodynamic and transport properties and anisotropic H_{c2} in $Ba(Fe_{1x}Co_x)_2As_2$ single crystals," *Physical Review B*, vol. 78, p. 214515, 2008.

[43] M. R. Norman, D. Pines, and C. Kallin, "The pseudogap: friend or foe of high T_c?," *Advances in Physics*, vol. 54, p. 715, 2005.

[44] J.-H. Chu, J. G. Analytis, C. Kucharczyk, and I. R. Fisher, "Determination of the phase diagram of the electron doped superconductor $Ba(Fe_{1-x}Co_x)_2As_2$," *Physical Review B*, vol. 79, p. 014506, 2009.

[45] Z. Bukowski, S. Weyeneth, R. Puzniak, P. Moll, S. Katrych, N. D. Zhigadlo, J. Karpinski, H. Keller, and B. Batlogg, "Superconductivity at 23 K and low anisotropy in rb-substituted $BaFe_2As_2$ single crystals," *Physical Review B*, vol. 79, p. 104521, 2009.

[46] C. Gen-Fu, L. Zheng, L. Gang, H. Wan-Zheng, D. Jing, Z. Jun, Z. Xiao-Dong, Z. Ping, W. Nan-Lin, and L. Jian-Lin, "Superconductivity in hole-doped $(Sr_{1x}K_x)Fe_2As_2$," *Chinese Physics Letters*, vol. 25, p. 3403, 2008.

[47] B. Shen, H. Yang, Z.-S. Wang, F. Han, B. Zeng, L. Shan, C. Ren, and H.-H. Wen, "Transport properties and asymmetric scattering in $Ba_{1-x}K_xFe_2As_2$ single crystals compared to the electron doped counterparts $Ba(Fe_{1-x}Co_x)_2As_2$," *Physical Review B*, vol. 84, p. 184512, 2011.

[48] M. Rotter, M. Pangerl, M. Tegel, and D. Johrendt, "Superconductivity and crystal structures of $(Ba_{1-x}K_x)Fe_2As_2$ (x=01)," *Angewandte Chemie*, vol. 47, p. 7949, 2008.

[49] T. B. Drye, S. R. Saha, J. Paglione, and P. Y. Zavalij, "Rare earth substitution in lattice-tuned $Sr_{0.3}Ca_{0.7}Fe_2As_2$ solid solutions," *Superconductor Science and Technology*, vol. 25, p. 084014, 2012.

[50] S. R. Saha, N. P. Butch, T. Drye, J. Magill, S. Ziemak, K. Kirshenbaum, P. Y. Zavalij, J. W. Lynn, and J. Paglione, "Structural collapse and superconductivity in rare-earth-doped $CaFe_2As_2$," *Physical Review B*, vol. 85, p. 024525, 2012.

[51] A. Carrington, "Quantum oscillation studies of the fermi surface of iron-pnictide superconductors," *Reports on Progress in Physics*, vol. 74, p. 124507, 2011.

[52] L. S. Cooper, "Bound electron pairs in a degenerate Fermi gas," *Physical Review*, vol. 104, p. 1189, 1956.

[53] V. P. Mineev and K. V. Samokhin, *Introduction to Unconventional Superconductivity*. Gordon and Breach Science Publishers, 1998.

[54] I. I. Mazin, D. J. Singh, M. D. Johannes, and M. H. Du, "Unconventional superconductivity with a sign reversal in the order parameter of $LaFeAsO_{1-x}F_x$," *Physical Review Letters*, vol. 101, p. 057003, 2008.

[55] K. Kuroki, S. Onari, R. Arita, H. Usui, Y. Tanaka, H. Kontani, , and H. Aoki, "Unconventional pairing originating from the disconnected fermi surfaces of superconducting $LaFeAsO_{1-x}F_x$," *Physical Review Letters*, vol. 101, p. 087004, 2008.

[56] A. V. Chubukov, D. V. Efremov, and I. Eremin *Physical Review B*, vol. 78, p. 134512, 2008.

[57] V. Cvetkovic and Z. Tesanovic *Europhysics Letters*, vol. 85, p. 37002, 2009.

[58] H. Ding, P. Richard, K. Nakayama, T. Sugawara, T. Arakane, Y. Sekiba, A. Takayama, S. Souma, T. Sato, T. Takahashi, Z. Wang, X. Dai, Z. Fang, G. F. Chen, J. L. Luo, and N. L. Wang, "Observation of fermi-surface-dependent nodeless superconducting gaps in $Ba_0.6K_0.4Fe_2As_2$," *Europhysics Letters*, vol. 83, p. 47001, 2008.

[59] K. Terashima, Y. Sekiba, J. H. Bowen, K. Nakayama, T. Kawahara, T. Sato, P. Richard, Y.-M. Xu, L. J. Li, G. H. Cao, Z.-A. Xu, H. Ding, and T. Takahashi, "Fermi surface nesting induced strong pairing in iron-based superconductors," *Proceedings of the National Academy of Science*, vol. 106, p. 7330, 2009.

[60] H. Kontani and S. Onari, "Orbital-fluctuation-mediated superconductivity in iron pnictides: Analysis of the five-orbital hubbard-holstein model," *Physical Review Letters*, vol. 104, p. 157001, 2010.

[61] T. Terashima, N. Kurita, M. Tomita, K. Kihou, C.-H. Lee, Y. Tomioka, T. Ito, A. Iyo, H. Eisaki, T. Liang, M. Nakajima, S. Ishida, S. ichi Uchida, H. Harima, and S. Uji, "Complete fermi surface in $BaFe_2As_2$ observed via shubnikov-de haas oscillation measurements on detwinned single crystals," *Physical Review Letters*, vol. 107, p. 176402, 2011.

[62] F. Hardy, P. Burger, T. Wolf, R. A. Fisher, P. Schweiss, P. Adelmann, R. Heid, R. Fromknecht, R. Eder, D. Ernst, H. v. Loehneysen, and C. Meingast, "Doping evolution of superconducting gaps and electronic densities of states in $Ba(Fe_{1-x}Co_x)_2As_2$ iron pnictides," *Europhysics Letters*, vol. 91, p. 47008, 2011.

[63] F. Hardy, T. Wolf, R. A. Fisher, R. Eder, P. Schweiss, P. Adelmann, H. v. Loehneysen, and C. Meingast, "Calorimetric evidence of multiband superconductivity in $Ba(Fe_{0.925}Co_{0.075})_2As_2$," *Physical Review B*, vol. 81, p. 060501(R), 2010.

[64] I. I. Mazin, "Superconductivity gets an iron boost," *Nature*, vol. 464, p. 183, 2010.

[65] S. Onari and H. Kontani, "Violation of andersons theorem for the sign-reversing s-wave state of iron-pnictide superconductors," *Physical Review Letters*, vol. 103, p. 177001, 2009.

[66] S. Graser, T. A. Maier, P. Hirschfeld, and D. Scalapino, "Near-degeneracy of several pairing channels in multiorbital models for the Fe-pnictides," *New Journal of Physics*, vol. 11, p. 025016, 2009.

[67] J.-P. Reid, M. A. Tanatar, X. G. Luo, H. Shakeripour, N. Doiron-Leyraud, N. Ni, S. L. Bud'ko, P. C. Canfield, R. Prozorov, and L. Taillefer *Physical Review B*, vol. 82, p. 064501, 2010.

[68] M. A. Tanatar, J. P. Reid, H. Shakeripour, X. G. Luo, N. Doiron-Leyraud, N. Ni, S. L. Bud'ko, P. C. Canfield, R. Prozorov, and L. Taillefer, "Doping dependence of heat transport in the iron-arsenide superconductor $Ba(Fe_{1-x}Co_x)_2As_2$: From isotropic to a strongly k-dependent gap structure," *Physical Review Letters*, vol. 104, p. 067002, 2010.

[69] B. Pei, B. Bjrkman, B. Jansson, and B. Sundman, "Thermodynamic assessment of the fe-as system using an ionic two-sublattice model for the liquid phase," *Z. Metallkd., retrieved from ASM International*, vol. 85, pp. 171–177, 1994.

[70] R. Hu, S. Ran, W. E. Straszheim, S. L. Bud'ko, and P. C. Canfield, "Single crystal growth and superconductivity of $Ca(Fe_{1x}Co_x)_2As_2$," *Philosophical Magazine*, vol. 92, p. 3113, 2012.

[71] N. W. Ashcroft and N. D. Mermin, *Solid State Physics*. Harcourt College Publishers, 1976.

[72] V. K. Pecharsky and P. Y. Zavalij, *Fundamentals of Powder Diffraction and Structural Characterization of Materials*. Springer, 2009.

[73] J. Goldstein, *Scanning Electron Microscopy and X-Ray Microanalysis*. Springer, 2003.

[74] Quantum Design, *Physical Property Measurement System: Hardware Manual*.

[75] Quantum Design, *Physical Property Measurement System: AC Transport Option Users Manual*.

[76] Quantum Design, *Magnetic Property Measurement System: Hardware Manual*.

[77] C. Kittel, *Introduction to Solid State Physics*. John Wiley and Sons, 1953.

[78] G. R. Stewart, "Heavy-fermion systems," *Reviews of Modern Physics*, vol. 56, p. 755, 1984.

[79] S. E. Sebastian, J. Gillett, N. Harrison, P. H. C. Lau, D. J. Singh, C. H. Mielke, and G. G. Lonzarich, "Quantum oscillations in the parent magnetic phase of an iron arsenide high temperature superconductor," *Journal of Physics: Condensed Matter*, vol. 20, p. 422203, 2008.

[80] N. Harrison, R. D. McDonald, C. H. Mielke, E. D. Bauer, F. Ronning, and J. D. Thompson, "Quantum oscillations in antiferromagnetic $CaFe_2As_2$ on the brink of superconductivity.," *Journal of Physics: Condensed Matter*, vol. 21, p. 322202, 2009.

[81] Lake Shore Cryotronics, Inc, *Users Manual: Model 370 AC Resistance Bridge*.

[82] P. C. Canfield, S. L. Budko, N. Ni, J. Q. Yan, and A. Kracher, "Decoupling of the superconducting and magnetic/structural phase transitions in electron-doped $BaFe_2As_2$," *Physical Review B*, vol. 80, p. 060501(R), 2009.

[83] R. G. Scurlock, *Low Temperature Behavior of Solids: An Introduction*. Dover Publication Inc., 1966.

[84] H. M. Rosenberg, *Low Temperature Solid State Physics.* Oxford University Press, 1963.

[85] S. Kasahara, T. Shibauchi, K. Hashimoto, K. Ikada, S. Tonegawa, R. Okazaki, H. Shishido, H. Ikeda, H. Takeya, K. Hirata, T. Terashima, and Y. Matsuda, "Evolution from non-fermi- to fermi-liquid transport via isovalent doping in $BaFe_2(As_{1x}P_x)_2$ superconductors," *Phys. Rev. B*, vol. 81, p. 184519, 2010.

[86] K. Jin, N. P. Butch, K. Kirshenbaum, J. Paglione, and R. L. Greene, "Link between spin fluctuations and cooper pairing in copper oxide superconductors," *Nature*, vol. 476, p. 73, 2011.

[87] H. V. Löhneysen, A. Rosch, M. Vojta, and P. Wölfle, "Fermi-liquid instabilities at magnetic quantum phase transitions.," *Rev. Mod. Phys.*, vol. 79, p. 1015, 2007.

[88] N. Doiron-Leyraud, "Correlation between linear resistivity and tc in the bechgaard salts and the pnictide superconductor $Ba(Fe_{1x}Co_x)_2As_2$.," *Phys. Rev. B*, vol. 80, p. 214531, 2009.

[89] M. Gooch, B. Lv, B. Lorenz, A. M. Guloy, and C.-W. Chu, "Evidence of quantum criticality in the phase diagram of $K_xSr_{1-x}Fe_2As_2$ from measurements of transport and thermoelectricity," *Phys. Rev. B*, vol. 79, p. 104504, 2009.

[90] A. Olariu, F. Rullier-Albenque, D. Colson, and A. Forget, "Different effects of Ni and Co substitution on the transport properties of $BaFe_2As_2$," *Physical Review B*, vol. 83, p. 054518, 2011.

[91] A. A. Abrikosov and L. Gor'kov *Soviet Physivs JETP*, vol. 12, p. 1243, 1961.

[92] P. W. Anderson, "Theory of dirty superconductors," *Journal of Physics and Chemistry of Solids*, vol. 11, p. 26, 1959.

[93] A. A. Abrikosov and L. Gor'kov *Sov. Phys. JETP*, vol. 12, p. 1243, 1961.

[94] H. Alloul, J. Bobroff, M. Gabay, and P. J. Hirschfeld, "Defects in correlated metals and superconductors," *Reviews of Modern Physics*, vol. 81, p. 45, 2009.

[95] M. Sato, Y. Kobayashi, S. C. Lee, H. Takahashi, E. Satomi, and Y. Miura, "Studies on effects of impurity doping and NMR measurements of La 1111 and/or Nd 1111 Fe-pnictide superconductors," *Journal of the Physical Society of Japan*, vol. 79, p. 014710, 2010.

[96] T. Kawamata, E. Satomi, Y. Kobayashi, M. Itoh, and M. Sato, "Study of ni-doping effect of specific heat and transport properties for $LaFe_{1-y}Ni_yAsO_{0.89}F_{0.11}$," *Journal of the Physical Society of Japan*, vol. 80, p. 084720, 2011.

[97] Y. Bang, H.-Y. Choi, and H. Won, "Impurity effects on the ±s-wave state of the iron-based superconductors," *Physical Review B*, vol. 79, p. 054529, 2009.

[98] V. G. Kogan, "Strong pairbreaking in anisotropic superconductors," *Physical Review B*, vol. 81, p. 184528, 2010.

[99] O. V. D. A. A. G. P. J. H. D. V. Efremov, M. M. Korshunov, "Disorder induced transition between s_{+-} and s_{++} states in two-band superconductors," *Physical Review B*, vol. 84, p. 180512(R), 2012.

[100] Y. Wang, A. Kreisel, P. J. Hirschfeld, and V. Mishra, "Using controlled disorder to distinguish $s_{\pm}$ and s_{++} gap structure in Fe-based superconductors," *ArXiv*, p. 1210.7474, 2012.

[101] G. R. Stewart, "Superconductivity in iron compounds," *Reviews of Modern Physics*, vol. 83, p. 1589, 2011.

[102] M. Naito, O. Matsumoto, A. Utsuki, A. Tsukada, H. Yamamoto, and T. Manabe, "Undoped cuprate superconductors band superconductors or oxygen-doped mott-hubbard superconductors?," *Journal of Physics: Conference Series*, vol. 108, p. 012037, 2008.

[103] J. S. Kim, T. D. Blasius, E. G. Kim, and G. R. Stewart, "Superconductivity in undoped single crystals of $BaFe_2As_2$: field and current dependence," *Journal of Physics: Condensed Matter*, vol. 21, p. 342201, 2009.

[104] M. A. Tanatar, N. Ni, G. D. Samolyuk, S. L. Budko, P. C. Canfield, and R. Prozorov, "Resistivity anisotropy of AFe2As2 (A=Ca, Sr, Ba): Direct versus montgomery technique measurements," *Physical Review B*, vol. 79, p. 134528, 2009.

[105] M. s. Torikachvili, S. L. Bud'ko, N. ni, P. C. Canfield, and S. T. Hannahs, "Effect of pressure on transport and magnetotransport properties in $CaFe_2As_2$ single crystals," *Physical Review B*, vol. 80, p. 014528, 2009.

[106] H. Hiramatsu, T. Katase, T. Kamiya, M. Hirano, and H. Hosono, "Water induced superconductivity in $SrFe_2As_2$," *Physical Review B*, vol. 80, p. 052501, 2009.

[107] X. F. Wang, T. Wu, G. Wu, H. Chen, Y. L. Xie, J. J. Ying, Y. J. Yan, R. H. Liu, and X. H. Chen, "Anisotropy in the electrical resistivity and susceptibility of superconducting $BaFe_2As_2$ single crystals," *Physical Review Letters*, vol. 102, p. 117005, 2009.

[108] M. Tegel, M. Rotter, V. Weiss, F. Schnappacher, R. Poettgen, and D. Johrendt, "Structural and magnetic phase transitions in the ternary iron arsenides $SrFe_2As_2$ and $EuFe_2As_2$," *Journal of Physics: Condensed Matter*, vol. 20, p. 452201, 2008.

[109] J.-Q. Yan, A. Kreyssig, S. Nandi, N. Ni, S. L. Budko, A. Kracher, R. J. McQueeney, R. W. McCallum, T. A. Lograsso, A. I. Goldman, and P. C. Canfield, "Structural transition and anisotropic properties of single-crystalline $SrFe_2As_2$," *Physical Review B*, vol. 78, p. 024516, 2008.

[110] A. S. Sefat, R. Jin, M. A. McGuire, B. C. Sales, D. J. Singh, and D. Mandrus, "Superconductivity at 22 k in co-doped $BaFe_2As_2$ crystals," *Physical Review Letters*, vol. 101, p. 117004, 2008.

[111] M. S. Torikachvili, S. L. Budko, N. Ni, and P. C. Canfield, "Pressure induced superconductivity in $CaFe_2As_2$," *Physical Review Letters*, vol. 101, p. 057006, 2008.

[112] P. L. Alireza, Y. T. C. Ko, J. Gillett, C. M. Petrone, J. M. Cole, G. G. Lonzarich, and S. E. Sebastian, "Superconductivity up to 29 k in $SrFe_2As_2$ and $BaFe_2As_2$ at high pressures," *Journal of Physics: Condensed Matter*, vol. 21, p. 012208, 2009.

[113] T. Park, E. Park, H. Lee, T. Klimczuk, E. D. Bauer, F. Ronning, and J. D. Thompson, "Pressure-induced superconductivity in $CaFe_2As_2$," *Journal of Physics: Condensed Matter*, vol. 20, p. 322204, 2008.

[114] A. Bianchi, R. Movshovich, M. Jaime, J. D. Thompson, P. G. Pagliuso, , and J. L. Sarrao, "Origin of the zero-resistance anomaly in heavy fermion superconducting $CeIrIn_5$: A clue from magnetic-field and Rh-doping studies," *Physical Review B*, vol. 64, p. 220504(R), 2001.

[115] W. Jiang, J. L. Peng, Z. Y. Li, and R. L. Greene, "Transport properties of $nd_{1.85}ce_{0.15}cuo_{4+\delta}$ crystals before and after reduction," *Physical Review B*, vol. 47, p. 8151, 1993.

[116] H. J. Kang, P. Dai, B. J. Campbell, P. J. Chupas, S. Rosenkranz, P. L. Lee, Q. Huang, S. Li, S. Komiya, and Y. Ando, "Microscopic annealing process and its impact on superconductivity in T-structure electron- doped copper oxides," *Nature Materials*, vol. 6, p. 224, 2007.

[117] A. P. Ramirez, T. Siegrist, T. T. M. Palstra, J. D. Garrett, E. Bruck, A. A. Menovsky, and J. A. Mydosh, "Superconducting phases of URu_2Si_2," *Physical Review B*, vol. 44, p. 5392, 1991.

[118] D. C. Johnston, "The puzzle of high temperature superconductivity in layered iron pnictides and chalcogenides," *Advances in Physics*, vol. 59, p. 803, 2010.

[119] J. Zhao, D.-X. Yao, S. Li, T. Hong, Y. Chen, S. Chang, W. R. II, J. W. Lynn, H. A. Mook, G. F. Chen, J. L. Luo, N. L. Wang, E. W. Carlson, J. Hu, and P. Dai, "Low energy spin waves and magnetic interactions in $SrFe_2As_2$," *Physical Review Letters*, vol. 101, p. 167203, 2008.

[120] J. Zhao, D. T. Adroja, D.-X. Yao, R. Bewley, S. Li, X. F. Wang, G. Wu, X. H. Chen, J. Hu, and P. Dai, "Spin waves and magnetic exchange interactions in $CaFe_2As_2$," *Nature Physics*, vol. 5, p. 555, 2009.

[121] W. L. Yang, A. P. Sorini, C.-C. Chen, B. Moritz, W.-S. Lee, F. Vernay, P. Olalde-Velasco, J. D. Denlinger, B. Delley, J.-H. Chu, J. G. Analytis, I. R. Fisher, Z. A. Ren, J. Yang, W. Lu, Z. X. Zhao, J. van den Brink, Z. Hussain, Z.-X. Shen, and T. P. Devereaux, "Evidence for weak electronic correlations in iron pnictides," *Physical Review B*, vol. 80, p. 014508, 2009.

[122] S. O. Diallo, V. P. Antropov, T. G. Perring, C. Broholm, J. J. Pulikkotil, N. Ni, S. L. Budko, P. C. Canfield, A. Kreyssig, A. I. Goldman, and R. J. McQueeney, "Itinerant magnetic excitations in antiferromagnetic $CaFe_2As_2$," *Physical Review Letters*, vol. 102, p. 187206, 2009.

[123] Q. Si and E. Abrahams, "Strong correlations and magnetic frustration in the high T_c iron pnictides," *Physical Review Letters*, vol. 101, p. 076401, 2008.

[124] A. H. Nevidomskyy, "Interplay of orbital and spin ordering in the iron pnictides," *ArXiv*, p. 1104.1747, 2011.

[125] J. P. Rodriguez and E. H. Rezayi, "Low ordered magnetic moment by off-diagonal frustration in undoped parent compounds to iron-based high-T_c superconductors," *Physical Review Letters*, vol. 103, p. 097204, 2009.

[126] C.-C. Chen, J. Maciejko, A. P. Sorini, B. Moritz, R. R. P. Singh, and T. P. Devereaux, "Orbital order and spontaneous orthorhombicity in iron pnictides," *Physical Review B*, vol. 82, p. 100504(R), 2010.

[127] M. D. Johannes and I. I. Mazin, "Microscopic origin of magnetism and magnetic interactions in ferropnictides," *Physical Review B*, vol. 79, p. 220510(R), 2009.

[128] Z. Tesanovic, "Viewpoint: Are iron pnictides new cuprates?," *Physics*, vol. 2, p. 60, 2009.

[129] T. Yildirim, "Strong coupling of the Fe-spin state and the As-As hybridization in iron-pnictide superconductors from first-principle calculations," *Physical Review Letters*, vol. 102, p. 037003, 2009.

[130] T. M. McQueen, M. Regulacio, A. J. Williams, Q. Huang, J. W. Lynn, Y. S. Hor, D. V. West, M. A. Green, and R. J. Cava, "Intrinsic properties of stoichiometric LaFePO," *Physical Review B*, vol. 78, p. 024521, 2008.

[131] J. Zhao, Q. Huang, C. de la Cruz, S. Li, J. W. Lynn, Y. Chen, M. A. Green, G. F. Chen, G. Li, Z. Li, J. L. Luo, N. L. Wang, and P. Dai, "Structural and magnetic phase diagram of $CeFeAsO_{1-x}F_x$ and its relation to high-temperature superconductivity," *Nature Materials*, vol. 7, p. 953, 2008.

[132] C.-H. Lee, A. Iyo, H. Eisaki, H. Kito, M. T. Fernandez-Diaz, T. Ito, K. Kihou, H. Matsuhata, M. Braden, and K. Yamada, "Effect of structural parameters on superconductivity in fluorine-free $LnFeAsO_{1-y}$ (Ln = La, Nd)," *Journal of the Physical Society of Japan*, vol. 77, p. 083704, 2008.

[133] K. Horigane, H. Hiraka, and K. Ohoyama, "Relationship between structure and superconductivity in $FeSe_{1-x}Te_x$," *Journal of the Physical Society of Japan*, vol. 78, p. 074718, 2009.

[134] E. Colombier, S. L. Budko, N. Ni, and P. C. Canfield, "Complete pressure-dependent phase diagrams for $SrFe_2As_2$ and $BaFe_2As_2$," *Physical Review B*, vol. 79, p. 224518, 2009.

[135] Z. Wang, H. Yang, C. Ma, H. Tian, H. Shi, J. Lu, L. Zeng, and J. Li, "The structural and physical properties of $Ba_{1-x}Sr_xFe_2As_2$ ($0 \leq x \leq 1$) and $Ba_{1-x}Sr_xFe_{1.8}Co_{0.2}As_2$ ($0 \leq x \leq 1$)," *Journal of Physics: Condensed Matter*, vol. 21, p. 495701, 2008.

[136] M. Rotter, C. Hieke, and D. Johrendt, "Different response of the crystal structure to isoelectronic doping in $BaFe_2(As_{1x}P_x)_2$ and $(Ba_{1x}Sr_x)Fe_2As_2$," *Physical Review B*, vol. 82, p. 014513, 2010.

[137] J. W. Lynn and P. Dai, "Neutron studies of the iron-based family of high T_c magnetic superconductors," *Physica C: Physics*, vol. 469, p. 469, 2009.

[138] Y. Z. Zhang, H. C. Kandpal, I. Opahle, H. Jeschke, and R. Valenti, "Microscopic origin of pressure-induced phase transitions in the iron pnictide superconductors AFe_2As_2: An ab initio molecular dynamics study," *Physical Review B*, vol. 80, p. 094530, 2009.

[139] M. Rotter, M. Tegel, and D. Johrendt, "Spin-density-wave anomaly at 140 K in the ternary iron arsenide $BaFe_2As_2$," *Physical Review B*, vol. 78, p. 020503(R), 2008.

[140] F. Ronning, T. Klimczuk, E. D. Bauer, H. Volz, and J. D. Thompson, "Synthesis and properties of $CaFe_2As_2$ single crystals," *Journal of Physics: Condensed Matter*, vol. 20, p. 322201, 2008.

[141] S. D. Wilson, C. R. Rotundu, Z. Yamani, P. N. Valdivia, B. Freelon, E. Bourret-Courchesne, and R. J. Birgeneau, "Universal magnetic and structural behaviors in the iron arsenides," *Physical Review B*, vol. 81, p. 014501, 2010.

[142] R. M. Fernandes, D. K. Pratt, W. Tian, J. Zarestky, A. Kreyssig, S. Nandi, M. G. Kim, A. Thaler, N. Ni, P. C. Canfield, R. J. McQueeney, J. Schmalian, and A. I. Goldman, "Unconventional pairing in the iron arsenide superconductors," *Physical Review B*, vol. 81, p. 140501(R), 2010.

[143] M. G. Kim, D. K. Pratt, G. E. Rustan, W. Tian, J. L. Zarestky, A. Thaler, S. L. Budko, P. C. Canfield, R. J. McQueeney, A. Kreyssig, and A. I. Goldman, "Magnetic ordering and structural distortion in Ru-doped $BaFe_2As_2$ single crystals studied by neutron and x-ray diffraction," *Physical Review B*, vol. 83, p. 054514, 2011.

[144] C. de la Cruz, W. Z. Hu, S. Li, Q. Huang, J. W. Lynn, M. A. Green, G. F. Chen, N. L. Wang, H. A. Mook, Q. Si, and P. Dai, "Different response of the crystal structure to isoelectronic doping in $BaFe_2(As_{1x}P_x)_2$ and $(Ba_{1x}Sr_x)Fe_2As_2$," *Physical Review Letters*, vol. 104, p. 017204, 2010.

[145] S. D. Wilson, Z. Yamani, C. R. Rotundu, B. Freelon, P. N. Valdivia, E. Bourret-Courchesne, J. W. Lynn, S. Chi, T. Hong, and R. J. Birgeneau, "Antiferromagnetic critical fluctuations in $BaFe_2As_2$," *Physical Review B*, vol. 82, p. 144502, 2010.

[146] H. Usui and K. Kuroki, "Maximizing the fermi-surface multiplicity optimizes the superconducting state of iron pnictide compounds," *Physical Review B*, vol. 84, p. 024505, 2011.

[147] J. R. Jeffries, N. P. Butch, K. Kirshenbaum, S. R. Saha, G. Samudrala, S. T. Weir, Y. K. Vohra, and J. Paglione, "Suppression of magnetism and development of superconductivity within the collapsed tetragonal phase of $Ca_{0.67}Sr_{0.33}Fe_2As_2$ under pressure," *Physical Review B*, vol. 85, p. 184501, 2012.

[148] J. Gillett, S. D. Das, P. Syers, A. K. T. Ming, J. I. Espeso, C. M. Petrone, and S. E. Sebastian, "Dimensional tuning of the magnetic-structural transition in $A(Fe_{1-x}Co_x)_2As_2$ (A=Sr,Ba)," *ArXiv*, p. 1005.1330, 2010.

[149] P. Richard, T. Sato, K. Nakayama, T. Takahashi, and H. Ding, "Fe-based superconductors: an angle-resolved photoemission spectroscopy perspective," *Reports on Progress in Physics*, vol. 74, p. 124512, 2011.

[150] M. Neupane, P. Richard, Y.-M. Xu, K. Nakayama, T. Sato, T. Takahashi, A. V. Federov, G. Xu, X. Dai, Z. Fang, Z. Wang, G.-F. Chen, N.-L. Wang, H.-H. Wen, and H. Ding, "Electron-hole asymmetry in the superconductivity of doped $BaFe_2As_2$ seen via the rigid chemical-potential shift in photoemission," *Physical Review B*, vol. 83, p. 094522, 2011.

[151] T. M. G. P. F. S. R. L. M.-F. F. G. G. d. M. A. P. G. P. E. M. Bittar, C. Adriano and E. Granado, "Co-substitution effects on the Fe valence in the $BaFe_2As_2$ superconducting compound: A study of hard x-ray absorption spectroscopy," *Physical Review Letters*, vol. 107, p. 267402, 2011.

[152] M. Merz, F. Eilers, T. Wolf, P. Nagel, H. v. Löhneysen, and S. Schuppler, "Electronic structure of single-crystalline $Sr(Fe_{1x}Co_x)_2As_2$ probed by x-ray

absorption spectroscopy: Evidence for effectively isovalent substitution of Fe^{2+} by Co^{2+}," *Physical Review B*, vol. 86, p. 104503, 2012.

[153] A. Khasanov, S. C. Bhargava, J. G. Stevens, J. Jiang, J. D. Weiss, E. E. Hellstrom, and A. Nath, "Mössbauer studies of the superconducting cobalt/nickel-doped $BaFe_2As_2$. whither go the injected electron(s)?," *Journal of Physics: Condensed Matter*, vol. 23, p. 202201, 2011.

[154] H. Wadati, I. Elfimov, and G. A. Sawatzky, "Where are the extra d electrons in transition-metal substituted Fe pnictides?," *Physical Review Letters*, vol. 105, p. 157004, 2010.

[155] S. L. Liu and T. Zhou, "Effect of transition-metal substitution in iron-based superconductors," *Journal of Physics: Condensed Matter*, vol. 24, p. 225701, 2012.

[156] T. Berlijn, C.-H. Lin, W. Garber, and W. Ku, "Do transition-metal substitutions dope carriers in iron-based superconductors?," *Physical Review Letters*, vol. 108, p. 207003, 2012.

[157] A. S. Sefat, D. J. Singh, L. H. VanBebber, Y. Mozharivskyj, M. A. McGuire, R. Jin, B. C. Sales, V. Keppens, and D. Mandrus, "Absence of superconductivity in hole-doped $BaFe_{2x}Cr_xAs_2$ single crystals," *Physical Review B*, vol. 79, p. 224524, 2009.

[158] A. Thaler, H. Hodovanets, M. S. Torikachvili, S. Ran, A. Kracher, W. Straszheim, J. Q. Yan, E. Mun, and P. C. Canfield, "Physical and magnetic properties of $Ba(Fe_{1-x}Mn_x)_2As_2$ single crystals," *Physical Review B*, vol. 84, p. 144528, 2011.

[159] N. Ni, A. Thaler, A. Kracher, J. Q. Yan, S. L. Bud'ko, and P. C. Canfield, "Temperature-doping phase diagrams for $Ba(Fe_{1-x}TM_x)_2As_2$(TM=Ni, Cu, Cu / Co) single crystals," *Physical Review B*, vol. 82, p. 024519, 2009.

[160] R. E. Baumbach, J. J. Hamlin, L. Shu, D. A. Zocco, N. M. Crisosto, and M. B. Maple, "Superconductivity in LnFePO (Ln= La, Pr and Nd) single crystals," *New Journal of Physics*, vol. 11, p. 025018, 2009.

[161] T. Terashima, M. Kimata, H. Satsukawa, A. Harada, K.Hazama, S. Uji, H. S. Suzuki, T. Matsumoto, and K. Murata, "$EuFe_2As_2$ under high pressure: An antiferromagnetic bulk superconductor," *Journal of the Physical Society of Japan*, vol. 78, p. 083701, 2009.

[162] N. R. Werthamer, E. Helfand, and P. C. Hohenberg, "Temperature and purity dependence of the superconducting critical field, H_{c2}. iii. electron spin and spin-orbit effects," *Physical Review*, vol. 147, p. 265, 1966.

[163] N. P. Butch, P. Syers, K. Kirshenbaum, A. P. Hope, and J. Paglione, "Superconductivity in the topological semimetal YPtBi," *Physical Review B*, vol. 84, p. 220504(R), 2011.

[164] M. Putti, I. Pallecchi, E. Bellingeri, M. Tropeano, C. Ferdeghini, A. Palenzona, C. Tarantini, A. Yamamoto, J. Jiang, J. Jaroszynski, F. Kametani, D. Abraimov, A. Polyanskii, J. D. Weiss, E. E. Hellstrom, A. Gurevich, D. C. Larbalestier, R. Jin, B. C. Sales, A. S. Sefat, M. A. McGuire, D. Mandrus, P. Cheng, Y. Jia, H. H. Wen, S. Lee, and C. B. Eom, "New Fe-based superconductors: properties relevant for applications," *Superconductor Science and Technology*, vol. 23, p. 034003, 2010.

[165] S. A. Baily, Y. Kohama, H. Hiramatsu, B. Maiorov, F. F. Balakirev, M. Hirano, and H. Hosono, "Pseudoisotropic upper critical field in cobalt-doped $SrFe_2As_2$ epitaxial films," *Physical Review Letters*, vol. 102, p. 117004, 2009.

[166] Y. Yin, M. Zech, T. L. Williams, X. F. Wang, G. Wu, X. H. Chen, and J. E. Hoffman, "Scanning tunneling spectroscopy and vortex imaging in the iron pnictide superconductor $BaFe_{1.8}Co_{0.2}As_2$," *Physical Review Letters*, vol. 102, p. 097002, 2009.

[167] M. A. Tanatar, N. Ni, C. Martin, R. T. Gordon, H. Kim, V. G. Kogan, G. D. Samolyuk, S. L. Budko, P. C. Canfield, and R. Prozorov, "Anisotropy of the iron pnictide superconductor $Ba(Fe_{1-x}Co_x)_2As_2$ (x=0.074, T_c=23 K)," *Physical Review B*, vol. 79, p. 094507, 2009.

[168] U. Welp, R. Xie, A. E. Koshelev, W. K. Kwok, H. Q. Luo, Z. S. Wang, G. Mu, and H. H. Wen, "Anisotropic phase diagram and strong coupling effects in $Ba_{1x}K_xFe_2As_2$ from specific-heat measurements," *Physical Review B*, vol. 79, p. 094505, 2009.

[169] H. Q. Yuan, J. Singleton, F. F. Balakirev, S. A. Baily, G. F. Chen, J. L. Luo, and N. L. Wang, "Nearly isotropic superconductivity in $(Ba,K)Fe_2As_2$," *Nature*, vol. 457, p. 565, 2009.

[170] L. Fang, H. Luo, P. Cheng, Z. Wang, Y. Jia, G. Mu, B. Shen, I. I. Mazin, L. Shan, C. Ren, and H.-H. Wen, "Roles of multiband effects and electron-hole asymmetry in the superconductivity and normal-state properties of $Ba(Fe_{1-x}Co_x)_2As_2$," *Physical Review B*, vol. 80, p. 140508(R), 2009.

[171] V. Brouet, M. Marsi, B. Mansart, A. Nicolaou, A. Taleb-Ibrahimi, P. L. Févre, F. Bertran, F. Rullier-Albenque, A. Forget, and D. Colson *Physical Review B*, vol. 80, p. 165115, 2009.

[172] C. Liu, T. Kondo, R. M. Fernandes, A. D. Palczewski, E. D. Mun, N. Ni, A. N. Thaler, A. Bostwick, E. Rotenberg, J. Schmalian, S. L. Budko, P. C. Canfield, and A. Kaminski, "Evidence for a lifshitz transition in electron-doped iron

arsenic superconductors at the onset of superconductivity," *Nature Physics*, vol. 6, p. 419, 2010.

[173] W. Schnelle, A. Leithe-Jasper, R. Gumeniuk, U. Burkhardt, D. Kasinathan, and H. Rosner, "Substitution-induced superconductivity in $SrFe_{2x}Ru_xAs_2$ ($0 \leq x \leq 2$)," *Physical Review B*, vol. 79, p. 214516, 2009.

[174] R. Hu, S. L. Budko, W. E. Straszheim, and P. C. Canfield, "Phase diagram of superconductivity and antiferromagnetism in single crystals of $Sr(Fe_{1-x}Co_x)_2As_2$ and $Sr_{1-y}Eu_y(Fe_{0.88}Co_{0.12})_2As_2$," *Physical Review B*, vol. 83, p. 094520, 2011.

[175] H. Kim, R. T. Gordon, M. A. Tanatar, J. Hua, U. Welp, W. K. Kwok, N. Ni, S. L. Bud'ko, P. C. Canfield, A. B. Vorontsov, and R. Prozorov, "London penetration depth in $Ba(Fe_{1-x}T_x)_2As_2$ (T=Co, Ni) superconductors irradiated with heavy ions," *Physical Review B*, vol. 82, p. 060518, 2010.

[176] Y. Nakajima, T. Taen, Y. Tsuchiya, T. Tamegai, H. Kitamura, and T. Murakami, "Suppression of critical temperature in $Ba(Fe_{1-x}Co_x)_2As_2$ with point defects introduced by proton irradiation," *Physical Review B*, vol. 82, p. 220504(R), 2010.

[177] Y. F. Guo, Y. G. Shi, S. Yu, A. A. Belik, Y. Matsushita, M. Tanaka, Y. Katsuya, K. Kobayashi, I. Nowik, I. Felner, V. P. S. Awana, K. Yamaura, and E. Takayama-Muromachi, "Large decrease in the critical temperature of superconducting $LaFeAsO_{0.85}$ compounds doped with 3% atomic weight of nonmagnetic Zn impurities," *Physical Review B*, vol. 82, p. 054506, 2010.

[178] G. Xiao, M. Z. Cieplak, J. Q. Xiao, and C. L. Chien, "Magnetic pair-breaking effects: Moment formation and critical doping level in superconducting $La_{1.85}Sr_{0.15}Cu_{1-x}A_xO_4$ systems (A=Fe,Co,Ni,Zn,Ga,Al)," *Physical Review B*, vol. 42, p. 8752, 1990.

[179] D. Tan, C. Zhang, C. Xi, L. Ling, L. Zhang, W. Tong, Y. Yu, G. Feng, H. Yu, L. Pi, Z. Yang, S. Tan, and Y. Zhang, "Different response of superconductivity to the transition-metal impurities in $K_{0.8}Fe_{2yx}M_xSe_2$ (M = Cr, Mn, Co, Zn)," *Physical Review B*, vol. 84, p. 014502, 2011.

[180] S. Konbu, K. Nakamura, H. Ikeda, and R. Arita, "Fermi-suface evolution by transition-metal substitution in the iron-based superconductor lafeaso," *Journal of the Physical Society of Japan*, vol. 80, p. 123701, 2011.

[181] S. Sharma, A. Bharathi, S. Chandra, V. R. Reddy, S. Paulraj, A. T. Satya, V. S. Sastry, A. Gupta, and C. S. Sundar, "Superconductivity in ru-substituted polycrystalline $BaFe_{2x}Ru_xAs_2$," *Physical Review B*, vol. 81, p. 174512, 2010.

[182] A. F. Kemper, M. M. Korshunov, T. P. Devereaux, J. N. Fry, H.-P. Cheng, and P. J. Hirschfeld, "Anisotropic quasiparticle lifetimes in Fe-based superconductors," *Physical Review B*, vol. 83, p. 184516, 2011.

[183] N. Barišić, D. Wu, and M. Dressel, "Electrodynamics of electron-doped iron pnictide superconductors: Normal-state properties," *Physical Review B*, vol. 82, p. 054518, 2010.

[184] M. Nakajima, S. Ishida, K. Kihou, Y. Tomioka, T. Ito, Y. Yoshida, C. H. Lee, H. Kito, A. Iyo, H. Eisaki, K. M. Kojima, and S. Uchida, "Evolution of the optical spectrum with doping in $Ba(Fe_{1-x}Co_x)_2As_2$," *Physical Review B*, vol. 81, p. 104528, 2010.

[185] J. J. Tu, J. Li, W. Liu, A. Punnoose, Y. Gong, Y. H. Ren, L. J. Li, G. H. Cao, Z. A. Xu, and C. C. Homes, "Optical properties of the iron arsenic superconductor $BaFe_{1.85}Co_{0.15}As_2$," *Physical Review B*, vol. 82, p. 174509, 2010.

[186] F. Rullier-Albenque, D. Colson, A. Forget, P. Thuéry, and S. Poissonnet, "Hole and electron contributions to the transport properties of $Ba(Fe_{1-x}Ru_x)_2As_2$ single crystals," *Physical Review B*, vol. 81, p. 224503, 2010.

[187] J. Li, Y. Guo, S. Zhang, S. Yu, Y. Tsujimoto, H. Kontani, K. Yamaura, and E. Takayama-Muromachi, "Linear decrease of critical temperature with increasing Zn substitution in the iron-based superconductor $BaFe_{1.892x}Zn_{2x}Co_{0.11}As_2$," *Physical Review B*, vol. 84, p. 020513(R), 2011.

[188] S. K. Kim, M. S. Torikachvili, E. Colombier, A. Thaler, S. L. Bud'ko, and P. C. Canfield, "Combined effects of pressure and ru substitution on $BaFe_2As_2$," *ArXiv*, p. 1107.6034, 2011.

[189] K. Nakamura, R. Arita, and H. Ikeda, "First-principles calculation of transition-metal impurities in LaFeAsO," *Physical Review B*, vol. 83, p. 144512, 2011.

[190] M. G. Vavilov and A. V. Chubukov, "Phase diagram of iron pnictides if doping acts as a source of disorder," *Physical Review B*, vol. 84, p. 214521, 2011.

[191] K. Gofryk, A. S. Sefat, M. A. McGuire, B. C. Sales, D. Mandrus, T. Imai, J. D. Thompson, E. D. Bauer, and F. Ronning, "Effect of annealing on the specific heat of optimally doped $Ba(Fe_{0.92}Co_{0.08})_2As_2$," *Journal of Physics: Conference Series*, vol. 273, p. 012094, 2011.

[192] E. Granado, L. Mendona-Ferreira, F. Garcia, G. de M. Azevedo, G. Fabbris, E. M. Bittar, C. Adriano, T. M. Garitezi, P. F. S. Rosa, L. F. Bufaical, M. A. Avila, H. Terashita, , and P. G. Pagliuso, "Pressure and chemical substitution effects in the local atomic structure of $BaFe_2As_2$," *Physical Review B*, vol. 83, p. 184508, 2011.

[193] H. Luo, P. Cheng, Z. Wang, H. Yang, Y. Jia, L. Fang, C. Ren, L. Shan, and H. Wen *Physica C*, vol. 469, p. 477484, 2009.

[194] Y. Li, J. Tong, Q. Tao, G. Cao, and Z. Xu, "Suppression of tc by zn impurity in the electron-type $LaFe_{0.925y}$ $Co_{0.075}Zn_yAsO$ system," *Journal of Physics and Chemistry of Solids*, vol. 72, p. 410, 2011.

[195] P. Cheng, H. Yang, Y. Jia, L. Fang, X. Zhu, G. Mu, , and H.-H. Wen, "Hall effect and magnetoresistance in single crystals of $NdFeAsO_{1x}F_x$ (x=0 and 0.18)," *Physical Review B*, vol. 78, p. 134508, 2008.